FLUID MECHANICS OF BACTERIAL SUSPENSIONS: TRACER TRANSPORT AND CONCENTRATION INSTABILITIES DRIVEN BY BACTERIA-SWIMMING-INDUCED HYDRODYNAMIC DISTURBANCES

A Dissertation

Presented to the Faculty of the Graduate School

of Cornell University

in Partial Fulfillment of the Requirements for the Degree of

Doctor of Philosophy

by

Kasyap Thottasserymana Vasudevan

January 2014

FLUID MECHANICS OF BACTERIAL SUSPENSIONS: TRACER TRANSPORT AND CONCENTRATION INSTABILITIES DRIVEN BY BACTERIA-SWIMMING-INDUCED HYDRODYNAMIC DISTURBANCES

Kasyap Thottasserymana Vasudevan, Ph.D.
Cornell University 2014

Swimming bacteria create hydrodynamic disturbances in the form of Stokesian force-dipoles and in this thesis we study the transport of passive tracer particles and instabilities that feature unstable bacteria concentration fluctuations in suspensions of swimming bacteria driven by those disturbances. We first calculate the effective diffusion coefficient of a passive, Brownian tracer particle in a uniform suspension of randomly swimming bacteria as a function of the bacterial concentration, geometry, motility, and the tracer Brownian diffusivity using theory and simulations based on binary interactions between bacteria and tracer particles and also experiments on bacterial suspensions seeded with colloidal tracers. Particular attention has been paid to understand the effect of the Brownian motion of the tracer and the tumbling of bacteria on the effective diffusivity of the tracer. Next, we analyze the stability of a bacterial suspension confined in a channel with an imposed cross-channel gradient of a chemical to which bacteria chemotactically respond. In the stationary base state without any fluid flow, the chemotaxis of bacteria leads to a net bacterial orientation along the chemical gradient direction and the chemotactic and diffusive fluxes of bacteria balance to yield an exponentially varying base-state bacterial concentration field across the channel. At the continuum level, the swimming induced force-dipoles of bacteria lead to an exponentially varying normal stress field across

the channel and we show that such a base state is linearly unstable to fluctuations in the bacterial concentration if the mean bacteria concentration exceeds a critical value. This instability involves a coupling between the bacteria-stress-driven fluid flow and the bacterial concentration field and it leads to cellular convective patterns in the channel. Finally, we experimentally study the near-contact-line dynamics of evaporating sessile drops of bacterial suspensions in which the evaporation-induced fluid flow results in accumulation of bacteria near the contact-line through the well-known "coffee ring" effect. Our experiments reveal a collective behavior of bacteria near the contact-line appearing in the form of periodic bacterial "jets" along the circumference of the drop. A qualitative reasoning of the problem suggests the possibility of a concentration instability driven by the active stress of swimming bacteria.

BIOGRAPHICAL SKETCH

Kasyap Thottasserymana Vasudevan was born to parents T. J. Vasudevan and P. N. Valsala in the state of Kerala in India. After completing his high school education at the Model Technical Higher Secondary School, Kochi, Kerala, he pursued his undergraduate degree in mechanical engineering at College of Engineering Trivandrum affiliated to the University of Kerala. He then pursued a master of science degree in aerospace engineering at the Indian Institute of Science, Bangalore, where he experimentally studied the disintegration process of elliptical liquid jets and then joined Cornell University as a graduate student in the School of Chemical and Biomolecular Engineering in Fall 2008. At Cornell, he investigated the transport processes and concentration instabilities in suspensions of swimming bacteria under the guidance of Professor Donald L. Koch.

Dedicated to my family

ACKNOWLEDGEMENTS

I am indebted to my adviser Professor Donald L. Koch for the exemplary support, inspiration, and motivation provided by him during my stay at Cornell. I shall always cherish the interactions with him as most intellectually fulfilling experiences of my life. I would like to thank Professor Abraham Stroock and Professor Jane Wang for serving in my dissertation committee and providing insightful suggestions on my research. I would like to also thank Professor Mingming Wu without whom the experimental part of my research would not have been materialized.

I am grateful to my friends and members of Koch group John (along with Gaurie), Rajesh, Arijit, Hsiu-yu, Anubhab (along with Senjuti), Mukul, Ling, and Stuart for making my Cornell days, both inside and outside the lab, quite memorable. I would like to extend my gratitude to members of the Wu group especially Beum and Chih-kuan for helping me in the experimental lab and I deeply appreciate the help from Yih Lin and Lindsey on early days of my experimental work. I gratefully acknowledge the assistance of undergraduate students Jon, Harris, Injun, and Zae in some of the projects that I did.

Special thanks go to Jack and Swapna for providing us company in Hasbrouck apartments and also to Binit for engaging badminton matches. I take this opportunity to thank my family back at home and friends outside Cornell for their kindness, love, and support. I will forever be grateful to my wife Indu for always being my greatest strength.

TABLE OF CONTENTS

LIST OF FIGURES

CHAPTER 1

INTRODUCTION

Recent experimental, numerical and theoretical investigations indicate that the hydrodynamic disturbances created by swimming bacteria can give rise to enhanced mixing and large scale, organized motion termed as collective motion in bacterial suspensions (see Koch & Subramanian (2011) and references therein). Typical bacteria such as *E. Coli* are composed of a spheroidal cell-body propelled by means of a helical bundle of thin filaments called flagella behind the cell-body. Individual flagellar filaments are rotated by motors inside the cell-body and the helical bundle forms and propels the cell-body forward when all the motors rotate in the counter clockwise direction when viewed from behind the cell-body. When one or more motors reverse their direction of rotation, the bacterium performs a "tumble" after which it picks a new swimming direction. Thus in a chemically neutral environment many bacteria such as *E. Coli* perform an unbiased random walk comprised of intervals of persistent swimming lasting about a second punctuated by short tumbling events after which they pick a new swimming direction (Berg, 2003). Since the typical bacterial length and swimming speed are of the order of 10 μm and 20 $\mu m/s$ respectively, the Reynolds number associated with their swimming is of the order of 10^{-4} and the swimming-induced hydrodynamic disturbances are Stokesian. A swimming bacterium experiences neither a net force nor a net torque so that the far-field nature of the bacterial fluid disturbance is that of a Stokesian force-dipole which decays like $1/x^2$ where x is the distance from the bacterium (Lauga & Powers, 2009). The present thesis addresses three important consequences of the hydrodynamic disturbances produced by swimming bacteria. The first is the transport of a passive, Brownian tracer particle in a bacterial suspension

and the remaining two are the hydrodynamic instabilities of bacterial suspensions that lead to fluctuations in bacterial concentration in two different physical settings, one being the case of bacterial suspensions confined in a channel and imposed with a cross-channel gradient of a chemical that attracts bacteria and the other being the case of evaporating sessile-drops of bacterial suspensions.

The importance of the first problem comes from the fact that the survival of bacteria depends crucially on the dispersal of nutrients and other chemical species such as signaling molecules and that recent experiments on suspensions of swimming bacteria (Wu & Libchaber, 2000; Kim & Breuer, 2004; Miño *et al.*, 2011) and simulations of hydrodynamically interacting self-propelled particles (Hernandez-Ortiz *et al.*, 2005; Underhill *et al.*, 2008; Hernandez-Ortiz *et al.*, 2009) have shown an enhanced diffusion of passive tracers such as colloidal beads and macromolecules with increasing bacterial concentration. A tracer particle experiencing hydrodynamic disturbances from randomly swimming bacteria would perform a diffusive random walk at long times (Wu & Libchaber, 2000; Hernandez-Ortiz *et al.*, 2005, 2009). For a Brownian tracer particle, the effective diffusivity is then the sum of the intrinsic Brownian diffusivity, the "hydrodynamic" diffusivity contributed by bacterial fluid disturbances, and a contribution from possible excluded volume interactions with bacteria if the particle size is comparable to that of the bacterium. Determination of the effective tracer diffusion coefficient is a problem of significant practical interest and a crucial issue here is that the hydrodynamic component of the effective diffusivity of the tracer in general could be a function of its Brownian diffusivity in addition to the parameters associated with bacteria such as their concentration, geometry, and motility. This is due to the facts that the velocity disturbance of a bacterium sampled by a tracer particle is a function of the position of the tracer relative to

the bacterium and this relative position evolves through the Brownian motion of the tracer in addition to bacterial swimming and bacterial velocity disturbances. A similar phenomenon occurs in the well-known Taylor-Aris dispersion (Taylor, 1953; Aris, 1956) of a solute in a tube in which the Brownian motion of solute particles enables them to sample the spatially varying Poiseuille flow field in the tube resulting in longitudinal dispersion with a coefficient that depends upon the molecular (Brownian) diffusivity of the solute in addition to the tube geometry and flow velocity.

Thus in the tracer transport problem we calculate the aforementioned hydrodynamic component of the effective tracer diffusivity in a dilute bacterial suspension as a function of the tracer Brownian diffusivity, bacterial concentration, geometry, swimming speed, and persistence time through a theory based on binary interactions between bacteria and tracer particles. The theory yields an explicit expression for the hydrodynamic diffusivity of the tracer particle through a Fickian constitutive relationship between the average tracer flux and the average tracer concentration gradient with the average being defined over all possible bacterium-tracer pair-interactions. A slender-body model is used for describing the hydrodynamic disturbances of swimming bacteria with the magnitude of the bacterial disturbance velocity assumed to be small compared to the bacterial swimming speed. The tracer particle is considered to be a point object so that we neglect the excluded volume interactions between the tracer particle and the bacterium. In order to investigate the effects of velocity disturbances with magnitudes comparable to the bacterial swimming speed as well as the excluded volume interactions between bacteria and tracer particles, we also calculate the tracer hydrodynamic diffusivity from explicit simulations of pairwise bacterium-tracer interactions. We also perform complementary exper-

iments in order to assess the accuracy of the theoretical predictions.

The primary motivation behind the investigation of concentration instabilities in bacteria suspensions driven by the hydrodynamic disturbances of the swimming bacteria is the experimental observation of large-scale flows in dense bacteria suspensions (Mendelson *et al.*, 1999; Wu & Libchaber, 2000; Dombrowski *et al.*, 2004; Sokolov *et al.*, 2007, 2009; Ishikawa *et al.*, 2011; Dunkel *et al.*, 2013) capable of strongly mixing the suspension (see Sokolov *et al.* (2009)). Numerical studies on hydrodynamically interacting self-propelled particles (Hernandez-Ortiz *et al.*, 2005; Saintillan & Shelley, 2007; Underhill *et al.*, 2008) strongly suggests that the bulk fluid flow originates from the bacteria-swimming-induced fluid disturbances and in particular (Saintillan & Shelley, 2007; Underhill *et al.*, 2008) indicate that large scale fluid motion arises from hydrodynamic instabilities of the suspension driven by the fluid disturbances associated with the swimming-induced force-dipoles on bacteria. At the continuum level, the effect of swimming induced force-dipoles on bacteria is to provide an "active" stress field as a function of the local orientation and concentration fields of bacteria and continuum theories of suspensions swimming bacteria (Subramanian & Koch, 2009) and other self-propelled particles (Simha & Ramaswamy, 2002; Saintillan & Shelley, 2008*a*,*b*; Hohenegger & Shelley, 2010) have shown the existence of hydrodynamic instabilities driven by the active stress of swimmers. These instabilities however do not involve the convection of bacteria by the fluid flow at the linear order and instead originate from the coupling between the bacterial orientation field and the fluid flow owing to a spatially uniform bacteria concentration field in the base state. We on the other hand, focus on the possibility of instabilities driven by the coupling between the fluid flow and the bacterial concentration field instead of the orientation field by

having fluid convection of bacteria in the linearized stability equations which requires an inhomogeneous bacterial concentration field in the base state. We first show that such a non-uniform base state naturally emerges and results in a concentration instability if the bacterial suspension is confined in a channel and subjected to the gradient of a chemical that attracts bacteria (chemo-attractant) across the channel. The case of bacterial suspensions with imposed chemical gradients is fundamentally important since the purpose of bacterial motility is to allow cells to respond to chemical cues in their environment and the response is often critical to their survival.

In the presence of a chemo-attractant gradient, bacteria bias their random walk by reducing the tumbling frequency when swimming up the chemical gradient and leaving it unaltered when swimming down resulting in a net bacterial migration along the chemical gradient (Berg, 2003). We investigate the effect of the aforementioned process termed as chemotaxis on the dynamics of the bacterial suspension by analyzing the linear stability of a suspension of chemotactic bacteria confined in a channel imposed with a cross-channel gradient of a chemo-attractant through continuum equations (Simha & Ramaswamy, 2002; Saintillan & Shelley, 2008*a*,*b*; Subramanian & Koch, 2009; Hohenegger & Shelley, 2010). The biased tumbling of bacteria in the presence of the attractant gradient results in a net bacterial orientation and migration velocity parallel to the attractant gradient. At long length and time scales compared to those associated with the persistence of bacterial swimming, fluxes due to chemotaxis and the random run-tumble motion of bacteria balance to yield an exponentially varying bacteria concentration profile across the channel in the base state. The associated bacterial stress field is also exponentially varying and is composed of normal stresses due to the mean bacterial orientation parallel to the

chemical gradient. This spatially non-uniform base state is then shown to be unstable to fluctuations in the bacterial concentration field when the bacterial concentration exceeds a critical value determined by the chemotactic migration velocity, bacterial diffusivity, and the channel depth. The instability is the result of the coupling between the bacteria stress driven fluid flow and the bacterial concentration and manifests as rectangular convection patterns. Thus the imposition of the chemo-attractant gradient provides a way to organize individual bacterial disturbances into a bulk flow capable of enhancing the dispersal of nutrients and other chemical species vital for bacteria. We also address the effect of fluid-shear-induced rotation of bacteria — the mechanism behind the previously reported instabilities of homogeneous bacterial suspensions (Simha & Ramaswamy, 2002; Saintillan & Shelley, 2008*a*,*b*; Subramanian & Koch, 2009; Hohenegger & Shelley, 2010)— on the aforementioned chemotaxis driven instability by performing a linear stability analysis of continuum equations of suspensions of swimming bacteria whose orientation respond to both the chemical gradient and the fluid shear. We find that shear rotation of bacteria in general has a destabilizing effect and below a critical suspension depth, the critical concentration is determined by the shear rotation instability mechanism. Above this critical depth the present mechanism of instability starts to influence the critical concentration and for large suspension depths the effect of shear rotation is negligible.

It turns out that the non-uniform state of a bacterial suspension which can potentially give rise to concentration instability can exist even without bacterial chemotaxis but under a very different physical setting of the suspension — an evaporating sessile drop. The evaporation of the drop drives a radially outward fluid flow inside the drop owing to the pinning of the contact-line, a phe-

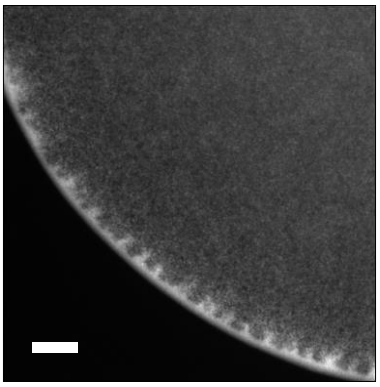

Figure 1.1: Collective motion near the contact-line of an evaporating drop containing wild-type *E. Coli* cells. The scale bar in the figure indicates a distance of 100 μm.

nomenon termed as the "coffee ring" effect (Deegan *et al.*, 1997, 2000). This flow concentrates bacteria near the contact-line due to the confinement provided by the air-water interface of the drop thus allowing one to examine the effect of passively created inhomogeneity in the suspension instead of the inhomogeniety resulting from active mechanisms such as chemotaxis as in the previous problem. The sessile drop geometry can also be important in the context of bacterial swarming and biofilm formation which often involve bacteria confined within thin liquid films (Bees *et al.*, 2000; Joanny & Ramaswamy, 2012). To understand if this setting gives rise to any instability, we study the near contact-line dynamics of sessile drops of bacterial suspensions experimentally. Our experiments reveal a collective behavior of the concentrated bacterial population near the contact-line appearing in the form of periodic "jets" of bacteria along the circumference of the drop. An image of the observed collective motion is shown in Fig. 1.1. A qualitative reasoning of the problem from the point of view of linear stability of the continuum equations for the conservation of bacteria and momentum

in the suspension suggests the possibility of a concentration instability of the suspension driven by the active stress of swimming bacteria.

Bibliography

ARIS, R. 1956 On the dispersion of a solute in a fluid flowing through a tube. *Proceedings of the Royal Society of London. Series A. Mathematical and Physical Sciences* **235** (1200), 67–77.

BEES, M. A., ANDRESN, P., MOSEKILDE, E. & GIVSKOV, M. 2000 The interaction of thin-film flow, bacterial swarming and cell differentiation in colonies of serratia liquefaciens. *Journal of Mathematical Biology* **40** (1), 27–63.

BERG, H. C. 2003 *E. coli in Motion*. Springer Verlag.

DEEGAN, ROBERT D, BAKAJIN, OLGICA, DUPONT, TODD F, HUBER, GREB, NAGEL, SIDNEY R & WITTEN, THOMAS A 1997 Capillary flow as the cause of ring stains from dried liquid drops. *Nature* **389** (6653), 827–829.

DEEGAN, ROBERT D., BAKAJIN, OLGICA, DUPONT, TODD F., HUBER, GREG, NAGEL, SIDNEY R. & WITTEN, THOMAS A. 2000 Contact line deposits in an evaporating drop. *Phys. Rev. E* **62**, 756–765.

DOMBROWSKI, C., CISNEROS, L., CHATKAEW, S., GOLDSTEIN, R. E. & KESSLER, J. O. 2004 Self-concentration and large-scale coherence in bacterial dynamics. *Phys. Rev. Lett.* **93**, 098103.

DUNKEL, JÖRN, HEIDENREICH, SEBASTIAN, DRESCHER, KNUT, WENSINK, HENRICUS H., BÄR, MARKUS & GOLDSTEIN, RAYMOND E. 2013 Fluid dynamics of bacterial turbulence. *Phys. Rev. Lett.* **110**, 228102.

HERNANDEZ-ORTIZ, J. P., STOLTZ, C. G. & GRAHAM, M. D. 2005 Transport and collective dynamics in suspensions of confined swimming particles. *Phys. Rev. Lett.* **95**, 204501.

HERNANDEZ-ORTIZ, JUAN P, UNDERHILL, PATRICK T & GRAHAM, MICHAEL D 2009 Dynamics of confined suspensions of swimming particles. *Journal of Physics: Condensed Matter* **21**, 204107 (13pp).

HOHENEGGER, C. & SHELLEY, M. J. 2010 Stability of active suspensions. *Phys. Rev. E* **81**, 046311.

ISHIKAWA, T., YOSHIDA, N., UENO, H., WIEDEMAN, M., IMAI, Y. & YAMAGUCHI, T. 2011 Energy transport in a concentrated suspension of bacteria. *Phys. Rev. Lett.* **107**, 028102.

JOANNY, JEAN-FRANÇOIS & RAMASWAMY, SRIRAM 2012 A drop of active matter. *Journal of Fluid Mechanics* **705**, 46–57.

KIM, M. J. & BREUER, K. S. 2004 Enhanced diffusion due to motile bacteria. *Phys. Fluids* **16**, L78–L81.

KOCH, D. L. & SUBRAMANIAN, G. 2011 Collective hydrodynamics of swimming microorganisms: Living fluids. *Ann. Rev. Fluid Mech.* **43**, 637–659.

LAUGA, E. & POWERS, T. R. 2009 The hydrodynamics of swimming microorganisms. *Rep. Prog. Phys.* **72**, 096601.

MENDELSON, N. H., BOURQUE, A., WILKENING, K., ANDERSON, K. R. & WATKINS, J. C. 1999 Organized Cell Swimming Motions in Bacillus subtilis Colonies: Patterns of Short-Lived Whirls and Jets. *J. Bacteriol.* **181**, 600–609.

MIÑO, GASTÓN, MALLOUK, THOMAS E., DARNIGE, THIERRY, HOYOS, MAURICIO, DAUCHET, JEREMI, DUNSTAN, JOCELYN, SOTO, RODRIGO, WANG, YANG, ROUSSELET, ANNIE & CLEMENT, ERIC 2011 Enhanced diffusion due to active swimmers at a solid surface. *Phys. Rev. Lett.* **106**, 048102.

SAINTILLAN, D. & SHELLEY, M. J. 2007 Orientational order and instabilities in suspensions of self-locomoting rods. *Phys. Rev. Lett.* **99**, 058102.

SAINTILLAN, D. & SHELLEY, M. J. 2008*a* Instabilities and pattern formation in active particle suspensions: Kinetic theory and continuum simulations. *Phys. Rev. Lett.* **100**, 178103.

SAINTILLAN, D. & SHELLEY, M. J. 2008*b* Instabilities, pattern formation, and mixing in active suspensions. *Phys. Fluids* **20**, 123304.

SIMHA, R. A. & RAMASWAMY, S. 2002 Hydrodynamic fluctuations and instabilities in ordered suspensions of self-propelled particles. *Phys. Rev. Lett.* **89**, 058101.

SOKOLOV, ANDREY, ARANSON, IGOR S., KESSLER, JOHN O. & GOLDSTEIN, RAYMOND E. 2007 Concentration dependence of the collective dynamics of swimming bacteria. *Phys. Rev. Lett.* **98**, 158102.

SOKOLOV, A., GOLDSTEIN, R. E., FELDCHTEIN, F. I. & ARANSON, I. S. 2009 Enhanced mixing and spatial instability in concentrated bacterial suspensions. *Phys. Rev. E* **80**, 031903.

SUBRAMANIAN, G. & KOCH, D. L. 2009 Critical bacterial concentration for the onset of collective swimming. *J. Fluid Mech.* **632**, 359–400.

TAYLOR, GEOFFREY 1953 Dispersion of soluble matter in solvent flowing slowly through a tube. *Proceedings of the Royal Society of London. Series A. Mathematical and Physical Sciences* **219** (1137), 186–203.

UNDERHILL, P. T., HERNANDEZ-ORTIZ, J. P. & GRAHAM, M. D. 2008 Diffusion and spatial correlations in suspensions of swimming particles. *Phys. Rev. Lett.* **100**, 248101.

WU, X. L. & LIBCHABER, A. 2000 Particle diffusion in a quasi-two-dimensional bacterial bath. *Phys. Rev. Lett.* **84**, 3017–3020.

CHAPTER 2

HYDRODYNAMIC TRACER DIFFUSION IN SUSPENSIONS OF SWIMMING BACTERIA

2.1 Abstract

We present theoretical predictions, simulations and experimental measurements for the transport of passive, Brownian tracer particles in an isotropic, quiescent suspension of swimming bacteria performing run-tumble random walks. Hydrodynamic disturbances created by randomly swimming bacteria result in enhanced tracer transport which we estimate in this paper theoretically as a function of the Brownian diffusivity of the tracer, bacterial concentration, swimming speed, geometry and persistence in bacterial swimming. We consider interactions between bacteria and tracer particles as binary and assume that the magnitude of the fluid disturbance is small compared to the bacterial swimming speed, an assumption that is valid in the slender body limit. The mass conservation equation for the tracer is then ensemble averaged over the configuration space of bacteria-tracer pair interactions. The average tracer flux can be related to the average tracer concentration gradient through a Fickian constitutive equation with an effective diffusion coefficient, $D_{eff} = D + nL^3U_sL\widetilde{D_h}$ where $\widetilde{D_h}$ is a non-dimensional "hydrodynamic" diffusivity of the tracer arising from fluid disturbances created by bacteria, D is the Brownian diffusivity of the tracer and n, L, and U_s are the concentration, overall length, and the swimming speed of bacteria respectively. Using a slender-body model for the bacterium, we derive an explicit expression for $\widetilde{D_h}$ as a function of a Peclet number, $Pe = U_sL/D$ which measures the strength of convective transport of tracer

particles relative to their diffusion and a non-dimensional bacterial persistence length, $\tau^* = U_s\tau/L$ with τ being the inverse tumbling frequency of bacteria. It is found that $\widetilde{D_h}$ increases monotonically with increasing τ^* and asymptotes to $\widetilde{D_h} \sim \alpha^2/(192\pi M^2)$ in the limits $Pe \to \infty$ and $\tau^* \to \infty$. Here, α is the ratio of the length of the cell-body of the bacterium to the overall bacterial length including the cell body and flagella bundle and M is the mobility of the cell body. The dependence of $\widetilde{D_h}$ on Pe is non-monotonic with $\widetilde{D_h} \sim \alpha^2\sqrt{Pe\tau^*}/(360\pi M^2)$ for $Pe \ll 1$ and with a peak when $Pe = O(10)$ indicating that weak Brownian motion of the tracer increases the efficacy of bacteria in transporting tracer particles. We also calculate the bacterial contribution to tracer diffusivity from explicit numerical simulations of bacteria-tracer interactions in the most physically relevant range of $Pe \geq O(1)$ and $\tau^* = O(1)$ to assess the accuracy of the assumption of weak fluid disturbance by bacteria and also to understand the effect of excluded volume interactions between bacteria and tracer particles. The simulation study shows that the theoretical treatment based on weak bacterial disturbance is accurate and that the volume exclusion between bacteria and tracer particles reduces the bacterial contribution to tracer diffusivity for smaller tracer particle sizes while increasing the same for large tracer particle sizes. Finally, we perform particle-tracking tracer diffusion experiments of colloidal particles in suspensions of wild-type *E. Coli* cells, validating the theoretical and simulation predictions for the dependence of the tracer diffusion on cell concentration.

2.2 Introduction

Mass transport in bacterial suspensions is an important problem since the survival of bacteria depends crucially on the dispersal of nutrients and other chemical species such as signaling molecules. Recent experiments on suspensions of swimming bacteria (Wu & Libchaber, 2000; Kim & Breuer, 2004; Miño *et al.*, 2011) and simulations of hydrodynamically interacting self-propelled particles (Hernandez-Ortiz *et al.*, 2005; Underhill *et al.*, 2008; Hernandez-Ortiz *et al.*, 2009) have shown an enhanced diffusion of passive tracers such as colloidal beads and macromolecules with increasing bacterial concentration. While swimming, bacteria produce Stokesian hydrodynamic disturbances and a tracer particle experiencing those disturbances from randomly swimming bacteria would perform a diffusive random walk at long times (Wu & Libchaber, 2000; Hernandez-Ortiz *et al.*, 2005, 2009). Displacements of colloidal tracers could be influenced by the finite size of the colloidal beads. For a Brownian tracer particle, the effective diffusivity is then the sum of the intrinsic Brownian diffusivity, the "hydrodynamic" diffusivity contributed by bacterial fluid disturbances, and a contribution from possible excluded volume interactions with bacteria. Determination of the effective tracer diffusion coefficient is a problem of significant practical interest and a crucial issue here is that the hydrodynamic component of the effective diffusivity of the tracer in general could be a function of its Brownian diffusivity in addition to the parameters associated with bacteria such as their concentration, geometry, and motility. This is due to the facts that the velocity disturbance of a bacterium sampled by a tracer particle is a function of the position of the tracer relative to the bacterium and this relative position evolves through the Brownian motion of the tracer in addition to bacterial swimming

and bacterial velocity disturbances. A similar phenomenon occurs in the well known Taylor-Aris dispersion (Taylor, 1953; Aris, 1956) of a solute in a tube in which the Brownian motion of solute particles enables them to sample the spatially varying Poiseuille flow field in the tube resulting in longitudinal dispersion with a coefficient that depends upon the molecular (Brownian) diffusivity of the solute in addition to the tube geometry and flow velocity. In this paper, we calculate the hydrodynamic component of the effective tracer diffusivity in a dilute bacterial suspension as a function of the tracer Brownian diffusivity, bacterial concentration, geometry, swimming speed, and persistence time through a theory based on binary interactions between bacteria and tracer particles. We validate the theoretical predictions and calculate the contribution to tracer diffusivity from bacteria-tracer excluded volume interactions through explicit simulations of pairwise bacterium-tracer interactions. We also perform complementary experiments in order to assess the accuracy of the theoretical predictions at moderate bacteria concentrations.

Typical bacteria such as *E. Coli* are comprised of a spheroidal cell-body propelled by a helical bundle of flagellar filaments. The flagellar filaments are driven by motors within the cell-body and when all the motors rotate in the counter-clockwise direction viewed from behind the cell-body, individual filaments merge to form a helical bundle and propel the cell forward. This leads to a swimming "run", which persists for around a second. The runs are punctuated by tumbles induced when one or more motors change their direction of rotation. Each tumble leads to a new direction for the next swimming run. The duration of the run or the persistence time of bacteria is not a constant but follows a Poissonian distribution and the run-tumble motion is unbiased in the absence of any chemical gradients (Berg, 1975). While modes of locomotion other than the

run-tumble motility have been discovered among bacteria (see Stocker (2011)), run-tumble motion remains to be the most extensively characterized one and hence this paper is focused on suspensions of run-tumble bacteria. Owing to the balance of the propulsive force generated by the flagellar bundle and the drag force on the cell-body, a bacterium as a whole is force-free and as a result its hydrodynamic disturbance is that of a force dipole which decays like $1/r^2$ at large distances r from the bacterium compared with its size (Hernandez-Ortiz *et al.*, 2005; Lauga & Powers, 2009).

The phenomenon of enhanced tracer diffusion due to swimming bacteria was first observed by Wu & Libchaber (2000) in their experiment with micron-sized particles suspended in a thin liquid film containing swimming *E. Coli* cells. The motion of particles was found to be correlated at short times and diffusive at long times with the measured diffusivity increasing linearly with the bacteria concentration. While the colloidal particles in the experiment of Wu & Libchaber (2000) were too large (4.5 μm and 10 μm) to have significant Brownian motion, macromolecules with relatively large Brownian diffusion also show enhanced diffusion in bacterial suspensions. For instance Kim & Breuer (2004) observed an effective tracer diffusion coefficient of a high molecular weight fluorescent dye dextran in bacterial suspensions flowing through microfluidic channels that increased linearly increasing bacterial concentration. While the aforementioned experiments are with liquid cultures, the enhanced transport of passive particles by bacteria-driven fluid flows has been observed in swarming bacterial colonies situated over agar surfaces (Wu *et al.*, 2011) and even in porous microfluidic devices containing swimming bacteria built to study bacteria-mediated contaminant transport in groundwater (Singh & Olson, 2011).

From a recent experimental study on bacterial suspensions close to a solid surface, Miño *et al.* (2011) have concluded that the enhancement in tracer diffusivity scales with the product of the concentration and the average velocity of actively swimming bacteria so that the effective tracer diffusivity should be given by $D_{eff} = D + nU_s\beta$ where D is the Brownian diffusivity of the tracer, n is the number of bacteria per unit volume of the suspension, U_s is the bacterial swimming speed, and the factor β arises from averaging tracer displacements from interactions with bacteria and should scale like the fourth power of bacterial size based on dimensional considerations (Miño *et al.*, 2011). The linear dependence signifies single bacterium effects and might be expected to hold only for dilute suspensions for which tracer interactions with more than one bacterium are negligible. However, in experiments with three dimensional suspensions (Kim & Breuer, 2004; Miño *et al.*, 2011) the linear relation has been observed to hold even at relatively large bacteria concentrations of 10^9 to 10^{10} bacteria per milliliter. For typical *E. Coli* cells with a cell-body length of $2\mu m$ (Berg & Turner, 1995) and flagella bundle length of $5\mu m$ (DePamphilis & Adler, 1971*a*,*b*), the aforementioned concentration range corresponds to the range of non-dimensional bacterial concentration $nL^3 = 0.3 - 3$ where n is the number of cells per unit volume and L is the overall length of the bacterial cell and flagellar bundle. A bacterial suspension is not truly dilute at these concentrations since dilute regime corresponds to $nL^3 \ll 1$. The linear variation of tracer diffusivity with swimmer concentration has also been observed in simulations of hydrodynamically interacting self-propelled particles mimicking bacteria (Hernandez-Ortiz *et al.*, 2005, 2009) and in particular Hernandez-Ortiz *et al.* (2009) reports linear scaling even for moderately dense suspensions. Their simulations however do not account for bacterial tumbling and Brownian motion of tracer par-

ticles. The importance of bacterial tumbling becomes readily apparent if one thinks of the hydrodynamic tracer diffusivity as the time-integral of the autocorrelation of the bacteria-induced fluid velocity disturbance sampled by the tracer particle. Since the bacterial disturbance velocity field is determined by the bacterial swimming direction, tumbling of bacteria to a new random orientation limits the time for which the disturbance velocity field remains correlated. Thus one may in general expect a reduction in tracer hydrodynamic diffusion with increasing bacterial tumbling frequency. Indeed, in the experiment of Kim & Breuer (2004), the effective tracer diffusivity in suspensions containing tumbly cells of *E. Coli* is significantly smaller than those containing wild-type cells.

Motivated by the aforementioned observations, we develop a theory for binary interactions between bacteria performing run-tumble random walks and Brownian tracer particles based on averaging the tracer transport equation over all possible pair-interactions for slowly varying tracer concentration fields where a Fickian constitutive equation relates the average tracer flux to the average tracer concentration gradient. The theory yields an explicit expression for the hydrodynamic diffusivity of the tracer particle. In the theoretical derivation the magnitude of the velocity disturbance of the bacterium is assumed to be small compared to its swimming speed, an assumption that is valid for a slender-body model of the bacterium whose cell body and flagellar tail exerts a line distribution of Stokeslets along its axis. The tracer particle is considered to be a point object so that we neglect the excluded volume interactions between the tracer particle and the bacterium. In order to investigate the effects of velocity disturbances with magnitudes comparable to the bacterial swimming speed as well as the excluded volume interactions between bacteria and tracer particles, we also calculate the tracer hydrodynamic diffusivity from explicit simu-

lations of pairwise bacterium-tracer interactions. Finally we carry out our own experiments on tracer diffusion to assess the accuracy of our theory since our theory is for an unbounded, isotropic, and three-dimensional bacterial suspension while the previous experiments are either on quasi-two-dimensional bacterial suspensions (Wu & Libchaber, 2000), bacterial suspensions lying close to a solid surface (Miño *et al.*, 2011), or strongly sheared bacterial suspensions (Kim & Breuer, 2004). One may expect the tracer hydrodynamic diffusivity in these situations to be different from that of a three-dimensional, isotropic, and unbounded suspension under consideration in this paper owing to the boundary conditions imposed by the film or the wall or due to the shear-induced rotation of bacteria. The latter makes the bacterial suspension anisotropic if the shear rate is comparable to or larger than the bacterial tumbling frequency as was the case in the experiment of Kim & Breuer (2004).

This paper is organized as follows: in §2.3 we present the theory for hydrodynamic tracer diffusion based on the averaged tracer transport equation. Next in §2.4 we derive the hydrodynamic tracer diffusivity through pairwise simulations of bacterium-tracer interactions and present the results. This is followed by §2.5 in which we describe our tracer diffusion experiments and compare the experimental data with the estimate of hydrodynamic diffusivity obtained from theory and simulations. Finally, we close the paper with a concluding discussion in §2.6.

2.3 Theory for hydrodynamic diffusion

The method of ensemble averaged equations (Hinch, 1977) was originally developed to describe the effects of hydrodynamic particle interactions on Stokes flow properties such as effective viscosity, sedimentation rate and permeability of dilute suspensions and fixed beds. It was adapted by Koch & Brady (1985) to analyze the macro - transport of chemical tracers in random porous media on a length scale much larger than the typical grain size. Specifically, one obtains a macroscopic convection-diffusion equation for the average tracer concentration field in the porous medium with the convection being driven by the bulk fluid velocity and diffusion constituted by the Brownian motion and the hydrodynamic diffusion driven by fluid disturbances created by grains in the porous medium. The average tracer concentration is defined by averaging over the ensemble of all possible realizations of the porous medium with different arrangements of the microstructural elements (Koch & Brady, 1985). In the present study, we apply this method to a bacterial suspension with the ensemble average consisting of different geometries of the bacterium-tracer interaction.

The formulation begins with the transport equation for the local tracer concentration $c(\boldsymbol{x}, t)$ (Koch & Brady, 1985)

$$\frac{\partial c}{\partial t} + \nabla \cdot \mathbf{q} = 0, \tag{2.1}$$

in which the flux at any given position and time is

$$\mathbf{q}(\mathbf{x}, t) = \mathbf{u}(\mathbf{x}, t)c(\mathbf{x}, t) - D\nabla c(\mathbf{x}, t), \tag{2.2}$$

where $\mathbf{u}c$ is the convective flux driven by the local fluid velocity $\mathbf{u}(\mathbf{x}, t)$ that the tracer experiences and $-D\nabla c$ is the diffusive flux driven by the local tracer concentration gradient (Koch & Brady, 1985). The random medium under consid-

eration in this paper is a suspension of wild-type bacteria executing run-tumble random walk with a swimming speed of U_s and a mean tumbling frequency of τ^{-1}. We assume that the suspension is unbounded, homogeneous, and isotropic with no imposed fluid flow and that the bacteria swim along straight lines between tumbles with the persistence time T (inverse tumbling frequency) following a Poisson distribution as (Berg, 1975)

$$P(T) = \frac{\exp\left(-\frac{T}{\tau}\right)}{\tau}. \tag{2.3}$$

It is also assumed that the swimming directions before and after a tumble are uncorrelated.

We now express the local velocity and tracer concentration fields in the bacterial suspension under consideration as the sum of corresponding bulk quantities (with an ensemble average indicated by $\langle\rangle$) and fluctuations due to bacteria indicated by primed variables:

$$\mathbf{u} = \langle \mathbf{u} \rangle + \mathbf{u}', \qquad c = \langle c \rangle + c'. \tag{2.4}$$

The bulk quantities in Eq. 2.4 are defined as averages over all possible realizations of the bacterial suspension with a particular realization being specified by the trajectories of all bacteria in the suspension. However, in a dilute suspension the tracer particle can be considered at any given time to be sampling the fluid disturbance created by a single bacterium so that the tracer interacts with each bacterium independently. In other words, all interactions between bacteria can be neglected and $\mathbf{u}'$ is the velocity disturbance created by an isolated bacterium. A consequence of this assumption is that any bulk property of the suspension can now be defined as an average over the ensemble of all possible realizations of the trajectory of a single bacterium.

Since the orientation $\mathbf{p}$ of a bacterium before and after a tumble are assumed to be uncorrelated, the fluid velocity produced by the bacterium in successive runs is also uncorrelated. As a result, one may define the operator $\langle\rangle$ as the average over the portion of the trajectory that lies between tumbles. The latter trajectory is

$$\mathbf{x}_b = \mathbf{x}_{b,0} + U_s \boldsymbol{p} \eta, \tag{2.5}$$

where $\mathbf{p}$ is the swimming direction, η is the time variable that parametrizes the trajectory, and $\mathbf{x}_{b,0}$ is the initial position of the center of the cell-body of the bacterium. The trajectory of the bacterium in Eq. 2.5 evolves until $\eta = T$ with T following the distribution in Eq. 2.3 and when $\eta = T$, the bacterium tumbles to a random orientation. The averaging over the trajectory in Eq. 2.5 now requires averaging over the time η, persistence time T, starting point $\mathbf{x}_{b,0}$, and swimming directions $\mathbf{p}$. For a homogeneous, isotropic suspension the probability densities of the latter two quantities are equal to the number of bacteria per unit volume of the suspension n and $1/(4\pi)$ respectively. This leads to the following expression as the definition of the average of any property $A(\mathbf{x}, t)$ of the suspension

$$\langle A \rangle(\mathbf{x}, t) = \frac{n}{4\pi\tau} \int \mathbf{dp} \int \mathbf{dx}_{b,0} \int_0^\infty dT P(T) \int_0^T d\eta A. \tag{2.6}$$

The above averaging process when applied to the tracer transport equation Eq. 2.1 yields the following evolution equation for $\langle c \rangle$

$$\frac{\partial \langle c \rangle}{\partial t} + \nabla \cdot \langle \mathbf{q} \rangle = 0, \tag{2.7}$$

where the average flux

$$\langle \mathbf{q} \rangle = \langle \mathbf{u}' c' \rangle - D \nabla \langle c \rangle. \tag{2.8}$$

This relationship makes use of the fact that there is no macroscopic fluid flow (quiescent suspension) ($\langle \mathbf{u} \rangle = 0$). When the average concentration gradient varies on length scales larger than the bacterium length and time scales larger

than the persistence time, the average flux in Eq. 2.8 can be related to the average concentration gradient through a Fickian diffusion relationship with an effective diffusivity tensor $\mathbf{D_{eff}}$

$$\langle \mathbf{q} \rangle = -\mathbf{D_{eff}} \cdot \nabla \langle c \rangle. \tag{2.9}$$

The steady solution of Eq. 2.7 at long times in then

$$\langle c \rangle = c_0 + \mathbf{G} \cdot \mathbf{x}, \tag{2.10}$$

where $\mathbf{G} = \nabla \langle c \rangle$ is the average concentration gradient and c_0 is an arbitrary constant. Equations 2.8 and 2.9 lead to the following expression for the bacterial contribution to the total flux:

$$\langle \mathbf{u}' c' \rangle = -(\mathbf{D_{eff}} - D\mathbf{I}) \cdot \nabla \langle c \rangle = -\mathbf{D_h} \cdot \nabla \langle c \rangle, \tag{2.11}$$

where $\mathbf{D_h}$ is the hydrodynamic diffusivity tensor and $\mathbf{I}$ is the identity tensor.

The governing equation for the fluctuation in the tracer concentration field due to bacteria obtained by subtracting Eq. 2.7 from Eq. 2.1 is

$$\frac{\partial c'}{\partial t} + \nabla \cdot (\mathbf{u}' c' - \langle \mathbf{u}' c' \rangle + \mathbf{u}' \langle c \rangle - D \nabla c') = 0, \tag{2.12}$$

in which the contribution from $\nabla \cdot \langle \mathbf{u}' c' \rangle$ vanishes owing to the relations in Eqs. 2.11 and 2.10. Since the velocity disturbance $\mathbf{u}'$ is from an isolated bacterium whose trajectory is described by Eq. 2.5, it is useful to rewrite Eq. 2.12 in a frame fixed on the bacterium as

$$\frac{\partial c'}{\partial \eta} + \nabla_{\mathbf{r}} \cdot [(\mathbf{u}' - U_s \mathbf{p}) c' - D \nabla_{\mathbf{r}} c'] = -\mathbf{u}' \cdot \nabla_{\mathbf{r}} \langle c \rangle, \tag{2.13}$$

in which the symbol $\nabla_{\mathbf{r}}$ stands for the vector differentiation in the relative coordinate $\mathbf{r} = \mathbf{x} - \mathbf{x}_{b,0} - U\mathbf{p}\eta$. Thus the source of the concentration fluctuation is the convection of the mean tracer concentration field by the fluid disturbance of

the bacteria and it evolves due to convection by the swimming of the bacterium (the $-U_s\mathbf{p}$ term) and the bacterial velocity disturbance (the $\mathbf{u}'c'$ term), as well as the Brownian diffusion. We now assume that the magnitude of the velocity disturbance created by the bacterium is much smaller than the swimming velocity ($|\mathbf{u}'| \ll U$) so that the $\mathbf{u}'c'$ term in Eq. 2.13 can be neglected. With this approximation and making use of Eq. 2.10, we obtain

$$\frac{\partial c'}{\partial \eta} - U_s\mathbf{p}\cdot\nabla_{\mathbf{r}}c' - D\nabla^2_{\mathbf{r}}c' = -\mathbf{u}'\cdot\mathbf{G}. \tag{2.14}$$

The assumption $|\mathbf{u}'| \ll U$ is valid for a slender-body model of a bacterium in which it is assumed that the ratio of the length L of the cell and flagella is large compared with the diameter d of the cell and the fluid velocity is smaller than the swimming speed by a factor of the logarithm of the aspect ratio. In practice we will find this to be a useful approximation even for moderate aspect ratios by comparing the theory with simulations that do not rely upon this approximation. The fluid velocity disturbance produced by a bacterium $\mathbf{u}'$ can in general have a complicated spatial dependence relative to the bacterium and hence it is easier to solve Eq. 2.14 in Fourier space rather than in real space. The Fourier transform of Eq. 2.14 with respect to the variable $\mathbf{r}$ is

$$\frac{\partial \widehat{c}}{\partial \eta} + (2\pi k)^2 D\widehat{c} - 2\pi i\mathbf{k}\cdot\mathbf{p}U_s\widehat{c} = -\widehat{\mathbf{u}}\cdot\mathbf{G}, \tag{2.15}$$

where $k = |\mathbf{k}|$ and $\widehat{c}(\mathbf{k},\eta)$ and $\widehat{\mathbf{u}}(\mathbf{k})$ are the Fourier amplitudes of the concentration and velocity disturbances defined as

$$\widehat{c}(\mathbf{k},\eta) = \int \mathbf{dr}c'(\mathbf{r},\eta)\exp(-2\pi i\mathbf{k}\cdot\mathbf{r}), \tag{2.16}$$

$$\widehat{\mathbf{u}}(\mathbf{k}) = \int \mathbf{dr}\mathbf{u}'(\mathbf{r})\exp(-2\pi i\mathbf{k}\cdot\mathbf{r}). \tag{2.17}$$

The solution of Eq. 2.15 satisfying the initial condition $\widehat{c}(\mathbf{k},0) = 0$ is

$$\widehat{c}(\mathbf{k},\eta) = \frac{\exp\{-[(2\pi k)^2 D - 2\pi i\mathbf{k}\cdot\mathbf{p}U_s]\eta\} - 1}{(2\pi k)^2 D - 2\pi i\mathbf{k}\cdot\mathbf{p}U_s}\widehat{\mathbf{u}}(\mathbf{k})\cdot\mathbf{G}. \tag{2.18}$$

We have applied an initial condition corresponding to zero concentration disturbance at the beginning of a bacterium's run because any concentration disturbance resulting from previous runs will be uncorrelated with the fluid velocity disturbance due to the present run and will result in no contribution to the mean flux of the tracer. Using the product theorem on Eq. 2.6, Eq. 2.11 takes the form

$$-\mathbf{D_h}\cdot\mathbf{G} = \frac{n}{4\pi\tau}\int \mathbf{dp}\int \mathbf{dk}\int dTP(T)\int_0^T d\eta\widehat{\mathbf{u}}(\mathbf{k})\widehat{c}(-\mathbf{k},\eta). \tag{2.19}$$

Using Eq. 2.18 in Eq. 2.19 and performing the integration over η and T explicitly yields an expression for the hydrodynamic diffusivity as

$$-\mathbf{D_h}\cdot\mathbf{G} = -\frac{n}{4\pi}\left[\int \mathbf{dp}\int \mathbf{dk}\frac{\widehat{\mathbf{u}}(\mathbf{k})\widehat{\mathbf{u}}(-\mathbf{k})}{(2\pi k)^2 D + 2\pi i\mathbf{k}\cdot\mathbf{p}U_s + \frac{1}{\tau}}\right]\cdot\mathbf{G}, \tag{2.20}$$

where the integral in brackets is a second order tensor and is independent of $\mathbf{k}$ and $\mathbf{p}$. Since the bacteria suspension is isotropic and there is no bulk fluid flow, the term in brackets must be a multiple of the second order identity tensor. This leads to the following expression for the scalar hydrodynamic diffusivity D_h defined by $\mathbf{D_h} = D_h\mathbf{I}$

$$D_h = \frac{n}{12\pi}\int \mathbf{dp}\int \mathbf{dk}\frac{\widehat{\mathbf{u}}(\mathbf{k})\cdot\widehat{\mathbf{u}}(-\mathbf{k})}{(2\pi k)^2 D + 2\pi i\mathbf{k}\cdot\mathbf{p}U_s + \frac{1}{\tau}}. \tag{2.21}$$

One may view Eq. 2.21 as the ensemble average of the integral of the disturbance velocity autocorrelation function of the tracer over the time variable η. We only need to perform the integral for the persistence time of the bacterium since the bacterial velocity disturbance autocorrelation becomes zero once the bacterium makes a tumble owing to the uncorrelated pre- and post-tumble bacterial orientations. Thus tumbling of bacteria has a strong influence on the hydrodynamic diffusivity since it limits the correlation time of tracer particles. Physically, one may expect that increasing the mean tumbling frequency of the bacterium τ^{-1} would reduce the hydrodynamic diffusivity of the tracer.

To proceed further, we need to know the Fourier amplitude of the fluid velocity disturbance produced by the bacterium $\widehat{\mathbf{u}}(\mathbf{k})$ in Eq. 2.21. While the simplest fluid-dynamical model of a bacterium is the force dipole, we shall show later that this model cannot account for the dependence of the hydrodynamic diffusivity on the bacterial tumbling frequency in the limit of $D \to 0$ owing to the inappropriateness of the dipole model at distances from the bacterium of the order of bacterial length and smaller. Since the bacterium is a rod-like object of overall aspect ratio of the order of 10, one may use a slender-body model for the bacterium instead of a force-dipole. Thus, we model the bacterium as a line distribution of Stokeslets along its axis with the net strength of the Stokeslets on the cell-body being equal to the viscous drag on the cell-body. The force per unit length on the flagella bundle is then adjusted based on the relative lengths of the cell-body and the flagella bundle to make the bacterium as a whole force-free. We have used this model previously to calculate the two-bacteria velocity correlations (Liao *et al.*, 2007) and to analyze the linear stability of bacteria suspensions (Subramanian & Koch, 2009). A similar slender body formulation was used in the simulations of Saintillan & Shelley (2007). The slender-body model leads to the forced Stokes' equations

$$-\nabla_{\mathbf{r}} p' + \mu \nabla^2_{\mathbf{r}} \mathbf{u}' = -f\mathbf{p} \left[\int_{-\alpha L/2}^{\alpha L/2} \delta(\mathbf{r} - s\mathbf{p}) ds - \frac{\alpha}{1-\alpha} \int_{-(1-\alpha/2)L}^{-\alpha L/2} \delta(\mathbf{r} - s\mathbf{p}) ds \right], \tag{2.22a}$$

$$\nabla_{\mathbf{r}} \cdot \mathbf{u}' = 0 \tag{2.22b}$$

in which L is the overall length of the bacterium including the flagella bundle and α is the ratio of the length of the cell-body to the overall length of the bacterium. In Eq. 2.22a the first integral on the right hand side is the forcing due to the cell-body with a force per unit length of

$$f = \frac{\mu U_s}{M} \tag{2.23}$$

where

$$M = (8\pi)^{-1}\{-2\gamma^2(\gamma^2-1)^{-1}+(2\gamma^3-\gamma)(\gamma^2-1)^{-3/2}\ln[(\gamma+\sqrt{\gamma^2-1})/(\gamma-\sqrt{\gamma^2-1})]\} \tag{2.24}$$

is the mobility of the cell-body considering the latter as a prolate spheroid of aspect ratio γ (Happel & Brenner, 1973). The second integral on the right hand side of Eq. 2.22a is the contribution from the force distribution of magnitude $\alpha f/(1-\alpha)$ on the flagella bundle and is in the opposite direction to the cell-body force distribution so that the net force on the bacterium is zero. For typical E. Coli cells, the length and width of the cell-body are around 2 μm and 1 μm respectively (Berg & Turner, 1995) with the flagella length being around 5 μm (DePamphilis & Adler, 1971*a*,*b*) which yield $\alpha = 2/7$ and $\gamma = 2$. The value of the cell-body mobility for the aspect ratio $\gamma = 2$ calculated from Eq. 2.24 is $M = 0.18$. The solution of Eq. 2.22 is

$$\mathbf{u}'(\mathbf{r}) = f\mathbf{p}\cdot\left[\int_{-\alpha L/2}^{\alpha L/2}\mathbf{J}(\mathbf{r}-s\mathbf{p})ds - \frac{\alpha}{1-\alpha}\int_{-(1-\alpha/2)L}^{-\alpha L/2}\mathbf{J}(\mathbf{r}-s\mathbf{p})ds\right]. \tag{2.25}$$

where $\mathbf{J}(\mathbf{r})$ is the Oseen's tensor defined as

$$\mathbf{J}(r) = \frac{1}{8\pi\mu}\left(\frac{\mathbf{I}}{r}+\frac{\mathbf{rr}}{r^3}\right) \tag{2.26}$$

and $r = |\mathbf{r}|$. For $r \gg L$ the velocity field in Eq. 2.25 reduces to $\mathbf{u}'(\mathbf{r}) = -(\alpha f L^2)/2[\mathbf{pp}:\nabla\mathbf{J}(\mathbf{r})]$ which corresponds to the disturbance caused by a force-dipole of strength $-(\alpha f L^2)/2$.

We now make a comparison between the slender-body velocity field in Eq. 2.25 and the experimental data of Drescher *et al.* (2011) in which the authors have measured the disturbance velocity field around a bacterium using particle image velocimetry. We take the swimming speed $U_s = 22\mu m/s$ in Eq. 2.23 which is the mean swimming speed measured in the experiment of Drescher

et al. (2011). Since Drescher *et al.* (2011) do not provide any measurements of the geometry of E. Coli cells used in the experiment, we use the typical values of the geometrical parameters $L = 7\mu m$, $\alpha = 2/7$, and $\gamma = 2$ in Eqs. 2.23 - 2.25. Furthermore, since the velocity field has been spatially averaged over square domains of size 0.63 μm in the experimental data of Drescher *et al.* (2011), we also average our calculated velocity field over the same length scale. The results of the comparison are shown in Fig. 2.1 in non-dimensional form in which the dimensionless bacterial disturbance velocity $\mathbf{u}'/U_s$ depends only on the geometry of the bacterium specified by the parameters α and γ besides the spatial dependence. We first observe in Fig. 2.1 that the slender-body velocity field is in excellent agreement with the experimental data on the transverse axis of the bacterium as well as ahead of the cell-body when $r/L > 1$. The agreement is moderate for these cases when r/L is close to unity or below and for the velocity profile along the flagella when $r/L > 1$. While the model significantly overestimates the magnitude of the fluid disturbance on the flagella when r/L is close to unity or below, the qualitative nature of the profile is faithfully reproduced. It has to be noted that the slender-body velocity field along the axis of the bacterium is actually singular within the flagella bundle and it is the spatial averaging that resulted in a non-singular velocity profile in Fig. 2.1. Nevertheless, the overall agreement between the slender-body model and the experimental data is reasonable considering that the geometrical parameters of the bacterium are not known in the experiments of Drescher *et al.* (2011).

Solving Eq. 2.22 in Fourier space and using Eq. 2.23 yields

$$\widehat{\mathbf{u}}(\mathbf{k}) = \frac{U_s L^3}{M k^2} \left[\mathbf{p} - \frac{(\mathbf{k}\cdot\mathbf{p})\mathbf{k}}{k^2} \right] F(\mathbf{k}\cdot\mathbf{p}) \tag{2.27}$$

in which the wavenumber is non-dimensionalized by $(2\pi L)^{-1}$ and the quantity

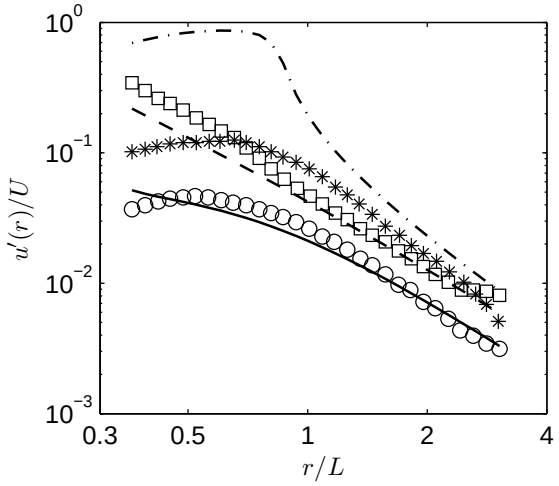

Figure 2.1: Comparison of the disturbance velocity profiles - the variation of the magnitude of the disturbance velocity with the distance from the center of the bacteria cell, obtained in the experiment of Drescher *et al.* (2011) (symbols) and the slender-body calculation given in Eq. 2.25 (lines). As in Drescher *et al.* (2011), velocity magnitudes at each point are averages over a square domain of size $0.63\mu m$. Squares and the dashed line show the velocity profiles on the axis of the bacterium and ahead of the cell-body along the direction of swimming. Asterisks and the dash-dotted line show the profiles on the axis along the flagella bundle and directed opposite to the swimming direction of bacterium. Finally, circles and the solid line represent the profiles along the transverse axis of the bacterium passing through the center of its cell-body.

$F(\mathbf{k}\cdot\mathbf{p})$ is defined as

$$F(\mathbf{k}\cdot\mathbf{p}) = -\frac{1}{i\mathbf{k}\cdot\mathbf{p}}\Bigg\{\exp(-i\alpha\mathbf{k}\cdot\mathbf{p}/2) - \frac{1}{1-\alpha}\exp(i\alpha\mathbf{k}\cdot\mathbf{p}/2) + \frac{\alpha}{1-\alpha}\exp\left(i[1-\alpha/2]\mathbf{k}\cdot\mathbf{p}\right)\Bigg\}. \tag{2.28}$$

At long length scales compared to bacterial length for which $k \ll 1$, $\widehat{\mathbf{u}}(\mathbf{k})$ becomes asymptotically close to the Fourier amplitude of the velocity disturbance of a force-dipole. Substituting Eq. 2.27 in Eq. 2.21 and non-dimensionalizing

the mean run time τ with the characteristic time scale L/U_s gives an expression for the hydrodynamic diffusivity as

$$D_h = nL^3 U_s L \widetilde{D_h}, \tag{2.29}$$

in which the non-dimensional hydrodynamic diffusivity $\widetilde{D_h}$ is given by

$$\widetilde{D_h} = \frac{1}{96\pi^4 M^2} \int d\mathbf{p} \int d\mathbf{k} \frac{[k^2 - (\mathbf{k}\cdot\mathbf{p})^2]\, F(\mathbf{k}\cdot\mathbf{p}) F(-\mathbf{k}\cdot\mathbf{p})}{k^6 \left(\frac{1}{\tau^*} + i\mathbf{k}\cdot\mathbf{p} + \frac{k^2}{Pe}\right)}. \tag{2.30}$$

In Eq. 2.30, $Pe = U_s L/D$ measures the strength of convective sampling by bacterial swimming relative to sampling by tracer diffusion and $\tau^* = U_s \tau / L$ measures the length that a bacterium swims before it tumbles relative to the length of the bacterium itself. Typical wild-type *E. Coli* has $\tau^* = O(1)$ and the typical Pe that one may encounter is primarily determined by the molecular diffusivity of the tracer. For instance, while the colloidal tracer particles used in the experiment of Wu & Libchaber (2000) are nearly non-Brownian with $Pe = O(10^3)$ corresponding to their thermal diffusivity (around 0.01 $\mu m^2/s$ for $4.5\mu m$ diameter particles and around $0.005\mu m^2/s$ for $10\mu m$ particles) typical bacterial length and speed of $L = 7\mu m$ and $U_s = 15\mu m/s$ respectively, the fluorescent dye used in the experiment of Kim & Breuer (2004) has $Pe \approx 5$ based on its molecular diffusivity of $20\mu m^2/s$ (see Fig. 4 in Kim & Breuer (2004)). We also consider the asymptotic limit of $\tau^* \gg 1$ with $Pe \gg 1$ which corresponds to a non-Brownian tracer in a suspension of smooth-swimming bacteria such as the *E. Coli* strain RP9535 (Wu *et al.*, 2006). We shall derive an analytical expression for the hydrodynamic diffusivity in this limit. It turns out that the product $F(\mathbf{k}\cdot\mathbf{p})F(-\mathbf{k}\cdot\mathbf{p})$ in Eq. 2.30 is both real and an even function of $\mathbf{k}\cdot\mathbf{p}$. As a result, the imaginary part of the integrand in Eq. 2.30 becomes an odd function of $\mathbf{k}\cdot\mathbf{p}$ and vanishes when integrated over $\mathbf{k}$ and $\mathbf{p}$ space. While the integral in Eq. 2.30 can be evaluated analytically using asymptotic techniques for the special cases of $Pe \ll 1$ with

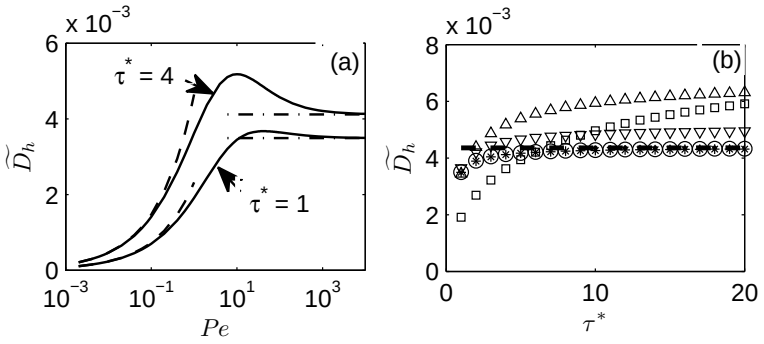

Figure 2.2: $\widetilde{D_h}$ as a function of (a) Pe for various τ^* (solid lines) and (b) τ^* for various Pe (symbols). The dashed lines in $Pe < 1$ region of figure (a) correspond to the asymptotic result $\widetilde{D_h} = \alpha^2\sqrt{Pe\tau^*}/(360\pi M^2)$ for $Pe \ll 1$ and $\tau^* \geq O(1)$. The dash-dotted line in $Pe \gg 1$ region of figure (a) corresponds to the limit $Pe \to \infty$. In figure (b) squares are for $Pe = 1$, up-triangles are for $Pe = 10$, down-triangles are for $Pe = 100$, circles are for $Pe = 10^4$, and asterisks as for $Pe = \infty$. The dashed line corresponds to the asymptotic result $\widetilde{D_h} = \alpha^2/(192\pi M^2)$ for the case $Pe \to \infty$ and $\tau^* \to \infty$.

$\tau^* \geq O(1)$ and $Pe \gg 1$ with $\tau^* \gg 1$, numerical integration is required for general cases. Equation 2.30 can be reduced to a one dimensional integral by first writing it as an integral over a cylindrical domain with axis along $\mathbf{p}$ for which $d\mathbf{k} = 2\pi k_\perp dk_\perp dk_\parallel$ where $k_\parallel = \mathbf{k}\cdot\mathbf{p}$ and $k_\perp = |\mathbf{k} - (\mathbf{k}\cdot\mathbf{p})\mathbf{p}|$ and evaluating the integral over $k_\perp$ space analytically. The remaining integration over $k_\parallel$ has been performed numerically using the adaptive Gauss - Kronrod quadrature routine.

Fig. 2.2 shows the results of our calculation of $\widetilde{D_h}$ as a function of Pe and τ^*. The values of geometrical parameters of the bacterium used in calculating $\widetilde{D_h}$ for all cases correspond to that of a typical bacterium so that $\gamma = 2$ and $\alpha = 2/7$. We have used the same values of these parameters while comparing the experimentally obtained bacterial disturbance velocity field (Drescher *et al.*, 2011) with our slender-body model earlier in this section. The primary observation from Fig. 2.2 is that while the non-dimensional hydrodynamic diffusivity increases

monotonically with increasing τ^* as expected, the variation is non-monotonic with respect to Pe. In the $Pe \ll 1$ regime, the Brownian diffusion of the tracer is much faster compared to bacterial swimming and as a result, the tracer - bacterium interactions are less effective in transporting the tracer. The asymptotic evaluation of the integral in Eq. 2.30 for $Pe \ll 1$ and $\tau^* \geq O(1)$ (see Appendix A) reveals that the $\widetilde{D_h} \sim \alpha^2\sqrt{Pe\tau^*}/(360\pi M^2)$ and this asymptotic result shown in Fig. 2.2(a) as a dashed-line agrees well with the numerical calculations shown by the solid line. The origin of the $\sqrt{Pe\tau^*}$ scaling in the limit of $Pe \ll 1$ and $\tau^* \geq O(1)$ can be understood physically by first writing down a generic scaling expression for the hydrodynamic diffusivity as

$$D_h \sim n l_s^3 u'(l_s)^2 \tau \tag{2.31}$$

where l_s is the typical length scale of separation between the bacterium and the tracer particle. This expression arises from the fact that the tracer displacement due to a bacterium's disturbance field stays correlated for a time scale of the order of the bacterium's persistence time τ and the typical velocity with which the tracer moves $u'(l_s)$ is a function of the typical tracer-bacterium separation distance l_s. Averaging over all possible tracer-bacteria interactions brings the factor nl_s^3. For the case of $Pe \ll 1$, the characteristic length scale of separation is the diffusion length of the tracer $l_s = O(\sqrt{D\tau})$ since bacteria translate only by a distance of $U_s\tau \ll \sqrt{D\tau}$. Indeed, as given in Appendix A, the dominant contribution to the integral comes from small wavenumbers with $k \leq O(\sqrt{Pe/\tau^*})$ which corresponds to bacteria-tracer separation length scales of order $\sqrt{D\tau}$ or smaller. Now if $\tau^* \geq 1$, $l_s/L = \sqrt{\tau^*/Pe} \gg 1$ and one may assume that $u'(l_s)$ is the fluid velocity disturbance of a force dipole with a characteristic dipole strength of $\mu U L^2$, $u'(l_s) = O(U_s L^2/l_s^2)$. Now using these scalings in Eq. 2.31 gives $D_h \sim nL^3 U_s L\sqrt{U_s^2\tau/D}$ which in turn yields $\widetilde{D_h} \sim \sqrt{Pe\tau^*}$.

When $Pe \gg 1$, the non-dimensional hydrodynamic diffusivity is independent of Pe as seen Fig. 2.2(a) indicating a purely convective transport of the tracer. This is further demonstrated by the coincidence of $Pe = 10^4$ data (circles) and $Pe = \infty$ data (asterisks) in Fig. 2.2(b). The figures however show that the hydrodynamic diffusivity is still dependent on τ^* thus yielding a scaling expression $D_h \sim nL^3U_sL\phi(\tau^*)$ in which the non-dimensional $\phi(\tau^*)$ has to be obtained numerically. However, Fig. 2.2(b) indicates that the hydrodynamic diffusivity becomes independent of τ^* in the limit $Pe \to \infty$ and $\tau^* \to \infty$. Though this limit corresponds to the case of a non-Brownian tracer particle in a suspension of bacteria which do not tumble at all, the $Pe = \infty$ data in Fig. 2.2(b) shows that this limit can be attained for $\tau^* \geq 5$. Experimentally, it is possible to attain the aforementioned limit by controlling the tumbling frequency of bacterium through the control of the level of CheY protein in the bacterium as demonstrated by Alon *et al.* (1998). The dependence of $\widetilde{D_h}$ on τ^* when $\tau^* = O(1)$ and the independence at large τ^* when Pe is large can be explained again through the scaling expression given in Eq. 2.31. First, the characteristic length scale of separation between a bacterium and a tracer particle is of the order of the bacterial persistence length, $l_s = O(U_s\tau)$ since the Brownian diffusion of the tracer is negligible in this high Pe regime. Now if $\tau^* \gg 1$ as in the case of smooth swimming bacteria, $l_s \gg L$ and the typical velocity disturbance experienced by the tracer follows the dipolar scaling $u'(l_s) = O(U_sL^2/l_s^2)$ again and for $l_s = O(U_s\tau)$, Eq. 2.31 yields the scaling $D_h \sim nL^3U_sL$ which means that $\widetilde{D_h}$ is independent of both Pe and τ^*. Mathematically, the dominant contribution to the integral in Eq. 2.30 comes from wavenumbers of order $1/\tau^*$ which gives the leading order non-dimensional hydrodynamic diffusivity as $\widetilde{D_h} = \alpha^2/(192\pi M^2)$ through the asymptotic evaluation of the integral in Eq. 2.30 in Appendix B. This expression

yields $\widetilde{D_h} \approx 0.0044$ for a typical bacterium with $\alpha = 2/7$ and $M = 0.18$ (corresponding to the cell-body aspect ratio $\gamma = 2$) in the non-tumbling limit so that the dimensional hydrodynamic diffusivity is given by $D_h = 0.0044nL^3U_sL$. It is clear from Fig. 2.2(b) that the latter prediction (shown by a dashed line) agrees well with the full numerical calculation for the case with $Pe = \infty$ (shown by asterisks) when $\tau^* \gg 1$. Now if $\tau^* = O(1)$, $l_s = O(L)$ for which the velocity field experienced by the tracer is not really dipolar. This results in a non-trivial relationship $\widetilde{D_h}$ with τ^* which can be obtained only through the numerical integration of Eq. 2.30 and hence the scaling $D_h \sim nL^3U_sL\phi(\tau^*)$. For a typical bacterium swimming at a speed of $15\mu m/s$ and tumbling at a rate of $1s^{-1}$, $\tau^* = 2.1$ for $L = 7\mu m$ and for this value of τ^* yields $\widetilde{D_h} = 0.0039$.

We now explicitly demonstrate that the dependence of the hydrodynamic diffusivity on the tumbling frequency of the bacterium in the limit of vanishing Brownian diffusivity cannot be captured if one models the bacterium as a point force dipole. As mentioned earlier, the dipolar velocity field of the bacterium obtained through the Taylor's expansion of the right hand side of Eq. 2.25 about $\mathbf{r}$ is

$$\mathbf{u}'_d(\mathbf{r}) = -\frac{\alpha f L^2}{2}\mathbf{pp} : \nabla \mathbf{J}(\mathbf{r}) \tag{2.32}$$

where $\mathbf{J}(\mathbf{r})$ is defined in Eq. 2.26. Fourier transforming Eq. 2.32 and using Eq. 2.23 yields

$$\widehat{\mathbf{u}}_d(\mathbf{k}) = -\frac{i\alpha U_s L^3}{2Mk^2}\mathbf{pp} : \mathbf{k}\left(\mathbf{I} - \frac{\mathbf{kk}}{k^2}\right), \tag{2.33}$$

in which the subscript "d" stands for dipole field. Equation 2.33 can also be obtained by expanding Eq. 2.27 in the limit of $k \ll 1$. Substituting $\widehat{\mathbf{u}}_d(\mathbf{k})$ in place of $\widehat{\mathbf{u}}(\mathbf{k})$ in Eq. 2.21 and non-dimensionalizing time using the characteristic time scale L/U_s, we obtain the following expression for the non-dimensional hydrodynamic diffusivity in the limit of vanishing tracer Brownian diffusivity

($Pe \to \infty$)

$$\widetilde{D_{hd}} = \frac{\alpha^2}{384\pi^4 M^2} \int \mathbf{dp} \int \mathbf{dk} \frac{(\mathbf{k}\cdot\mathbf{p})^2 \left[k^2 - (\mathbf{k}\cdot\mathbf{p})^2\right]}{k^6 \left(\frac{1}{\tau^*} - i\mathbf{k}\cdot\mathbf{p}\right)}. \tag{2.34}$$

The integral in Eq. 2.34 can be explicitly evaluated easily by splitting it over $k_\parallel$ and $k_\perp$ spaces and the resulting expression for non-dimensional hydrodynamic diffusivity

$$\widetilde{D_{hd}} = \frac{\alpha^2}{192\pi M^2} \tag{2.35}$$

is independent of τ^* no matter what τ^* is and is the same as the $Pe \gg 1$, $\tau^* \gg 1$ asymptote of $\widetilde{D_h}$ calculated earlier using the slender-body model for the bacterium. The lack of dependence of the hydrodynamic diffusivity on the bacterial persistence time is an artifact of the $1/r^2$ singularity of the force dipole. This can be elucidated easily through the generic scaling expression for the hydrodynamic diffusivity given in Eq. 2.31. In the absence of any Brownian motion $l_s = U_s\tau$ in Eq. 2.31 and since the velocity disturbance is dipolar $u'(l_s) = UL^2/l_s^2$ for all τ in Eq. 2.31. This gives the scaling $D_h \sim nL^3U_sL$ which means that $\widetilde{D_h}$ is a constant.

A surprising feature in Fig. 2.2(a) is the non-monotonic dependence of the hydrodynamic diffusivity on the Peclet number. This is also evident in the downward shift of $\widetilde{D_h}$ versus τ^* curves with increasing Pe (beyond $Pe = 1$) in Fig. 2.2(b). The hydrodynamic diffusivity is largest when $Pe = O(10)$ which signifies that weak Brownian diffusion in fact makes bacteria more efficient in transporting the tracer. This is in sharp contrast with the case of fixed beds (Koch & Brady, 1985) in which the hydrodynamic diffusivity decreases monotonically with a decrease in Pe. In general, the hydrodynamic diffusivity is expected to decrease monotonically with decreasing Pe since the increased Brownian displacement of the tracer relative to its convective displacement makes the tracer motion less correlated. A bacterial suspension differs from this picture

owing to the fact that the bacterial disturbance velocity field points in opposite directions at the front and back of the bacterium. The odd nature of the dipolar fluid disturbance produced by the bacterium limits the integral of the tracer velocity autocorrelation and hence its hydrodynamic diffusion. We elucidate thus further in Fig. 2.3 in which we show the interaction between a bacterium and a tracer particle happening over a typical bacterial run with and without Brownian motion for the tracer. Since the hydrodynamic diffusivity of the tracer is given by the integral of the autocorrelation of the bacterial disturbance velocity sampled by the tracer, the contribution to the hydrodynamic diffusivity from a given tracer trajectory can be written as an integral along the tracer trajectory $(1/3)\int \mathbf{u}'(\mathbf{x})\cdot\mathbf{u}'(\mathbf{x}+\mathbf{x}'(s))ds$ where $\mathbf{x}'(s)$ is the tracer trajectory parametrized by the variable s. In the absence of any tracer Brownian diffusion there exists only a single tracer-bacterium relative trajectory for a given pair of initial locations of the bacterium and the tracer particle and the run duration of the bacterium. For weak bacterial disturbances, the aforementioned trajectory is a straight line as shown in Fig. 2.3 by the solid line. Depending upon the the run duration of the bacterium, the tracer trajectory could span regions where the component of the bacterial disturbance velocity parallel to the tracer trajectory has opposite signs. This decreases the contribution to the integral of velocity autocorrelation from that trajectory and hence decreases the hydrodynamic diffusivity especially if the trajectory has equal lengths in those two regions with different signs for the velocity disturbance parallel to the trajectory. On the other hand, a non-zero tracer Brownian diffusivity helps the tracer sample an infinite number of possible trajectories for any given initial locations of the bacterium and the tracer and the bacterial run duration many of which can have displacements perpendicular to the trajectory as shown in Fig. 2.3 by a dash-dot line. Even a

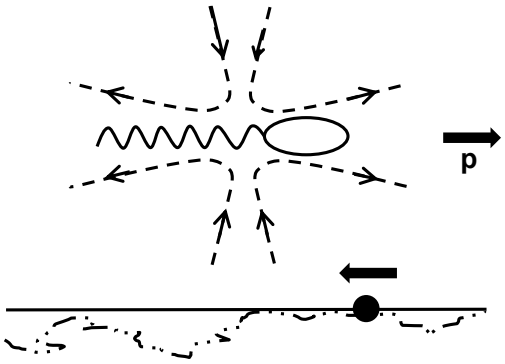

Figure 2.3: A typical tracer-bacterium interaction. The bacterium's velocity disturbance streamlines are shown by dashed lines and the solid line shows the trajectory of the tracer relative to the bacterium in the absence of any Brownian motion. The tracer's trajectory relative to the bacterium in presence of Brownian motion is shown by a dash-dot line.

relatively small Brownian displacement perpendicular to the bacterium orientation can modulate the strength of the fluid velocity disturbance parallel to the orientation leading to a net displacement for initial bacterium positions and run lengths that might have led to zero net displacement otherwise. The average contribution to the tracer velocity autocorrelation due to these weakly Brownian trajectories will in general be larger than the straight trajectory that one would have in the absence of tracer Brownian motion even when equal lengths of the trajectory lie in regions with opposite signs of velocity disturbance parallel to the swimming direction and this increases the hydrodynamic diffusivity. In other words, having a weak Brownian motion for the tracer helps the latter in sampling the velocity field around the bacterium in a manner more likely to produce a net displacement for each interaction and a larger hydrodynamic diffusivity averaged over all interactions than in the case without any Brownian motion. Nevertheless, a large tracer Brownian diffusivity would reduce

the tracer velocity autocorrelation and hence would reduce the hydrodynamic diffusivity.

2.4 Calculation of $\widetilde{D_h}$ through numerical simulations of pairwise tracer-bacterium interactions

In deriving the hydrodynamic diffusivity in the previous section, we have assumed that the disturbance fluid velocity produced by the bacterium is small compared to the swimming velocity. In a slender-body model of a high aspect ratio bacterium, the fluid velocity is indeed logarithmically small in the outer region corresponding to separations from the bacterium axis of order L which contribute most to the integrals leading to the diffusivity. However, the fluid velocity does become of $O(U_s)$ at separations from the axis of order of the bacterium diameter and even diverges logarithmically if (as we have done in the calculations) we extend the fluid velocity description to the axis of the bacterium itself. To test for possible effects of the finite ratio of fluid velocity to bacterium swimming speed, we therefore perform numerical simulations of pairwise interaction between a bacterium and a colloidal tracer particle. We find that the finite ratio has no noticeable effect on the predicted hydrodynamic diffusivity. An additional purpose served by the simulations is the investigation of the effects of excluded volume interactions between bacteria and tracer particles as most of the experiments on enhanced diffusion in bacteria suspensions are with tracer particles of size comparable to the size of the bacterium (Wu & Libchaber, 2000; Miño *et al.*, 2011). The simulations will not include the detailed hydrodynamic interactions between the bacterium and the tracer particle. Instead the

tracer particle which is assumed to be spherical, will be convected with the fluid velocity disturbance due to our slender-body model of the bacterium evaluated at the center of the particle.

We simulate the interactions of the tracer with bacteria that come within a distance R of the tracer's initial position at some point within the their run. Here, R and all lengths in this section are non-dimensionalized by the bacterium length L and velocities are non-dimensionalized with the swimming speed U_s. In a dilute suspension it is rare that two bacteria will affect a tracer's motion simultaneously and so we consider the bead to be influenced by one bacterium at a time. Furthermore, the random selection of a new direction $\mathbf{p}$ for each bacterium run implies that any displacement of the bead during one run is uncorrelated with that induced by the previous run of the same bacterium and so we treat each run as an independent stochastic event.

During each bacterium run, the positions $\mathbf{x}$ and $\mathbf{x}_b$ of the tracer and bacterium, respectively, evolve as

$$\mathbf{x}(t+\Delta t) = \mathbf{x}(t) + \mathbf{u}'(\mathbf{x}(t) - \mathbf{x}_b(t))\Delta t + \sqrt{\frac{6\Delta t}{Pe}}\boldsymbol{\xi} + \boldsymbol{\delta}_{ex}, \tag{2.36a}$$

$$\mathbf{x}_b(t+\Delta t) = \mathbf{x}_b(t) + \mathbf{p}\Delta t, \tag{2.36b}$$

in which $\boldsymbol{\xi}$ is a random vector of unit magnitude so that $\langle\boldsymbol{\xi}\rangle = 0$ and $\langle\boldsymbol{\xi}\boldsymbol{\xi}\rangle = (\mathbf{I}/3)$ where $\mathbf{I}$ is the identity tensor and $\boldsymbol{\delta}_{ex}$ is the displacement of the tracer due to excluded volume interaction with the bacterium. The disturbance velocity field of the bacterium $\mathbf{u}'(\mathbf{x}(t) - \mathbf{x}_b(t))$ is obtained by the numerical integration of Eq. 2.25 using an adaptive Simpson's quadrature routine. To obtain $\boldsymbol{\delta}_{ex}$, we first model the bacterium as a sphero-cylinder with an overall length equal to the bacterial length L and radius equal to the radius of the cell-body $d/2$. The tracer particle is then assumed to be spherical with a radius R_t so that tracer-

bacterium excluded volume is a sphero-cylinder with a non-dimensional radius $R_{ex} = (d/2 + R_t)/L$ and length $L_{ex} = 1 + 2(R_t/L)$. Whenever the center of the tracer particle comes within the excluded volume zone, the tracer is pulled back along the normal direction of the surface of the excluded volume and this displacement is added to the tracer trajectory equation Eq. 2.36b as the quantity $\boldsymbol{\delta}_{ex}$. We set $\boldsymbol{\delta}_{ex}$ to be zero if the center of the tracer particle is outside the excluded volume. The position of the tracer is chosen as $\mathbf{x} = 0$ at the beginning of the run $t = 0$. The duration T of the run is chosen from the Poisson distribution and the orientation $\mathbf{p}$ of the bacterium is chosen isotropically on the unit sphere. We then stipulate that the bacterium should pass through a random location $\mathbf{x}_b'$ with $|\mathbf{x}_b'| \leq R$ where R is the radius of the spherical control volume at some randomly chosen time $0 < t' < T$ which gives the starting point of the bacterial trajectory as $\mathbf{x}_b(0) = \mathbf{x}_b' - \mathbf{p}t'$.

To calculate the hydrodynamic and excluded volume contributions to the tracer diffusivity, we are interested in determining the influence of the bacterium on the tracer motion. Thus, in addition to the tracer position $\mathbf{x}$ which is influenced by both Brownian motion and the bacterium interaction, we define a displacement $\mathbf{x}_{tb}$ that results from the fluid velocity disturbance due to the bacterium and the excluded volume interaction at the position $\mathbf{x}$ and therefore evolves as

$$\mathbf{x}_{tb}(t + \Delta t) = \mathbf{x}_{tb}(t) + \mathbf{u}'(\mathbf{x}(t) - \mathbf{x}_b(t))\Delta t + \boldsymbol{\delta}_{ex}, \tag{2.37}$$

with the initial condition $\mathbf{x}_{tb}(0) = 0$. Here the subscript "tb" stands for tracer displacement caused by bacteria. At the end of each bacterial run occurring when $t = T$, the displacements of the tracer particle $\mathbf{x}_{tb}(T)$ is recorded and the evolution of all trajectories are stopped. The pairwise simulation is repeated to accumulate the statistics on tracer displacements and the mean-square

tracer displacement induced by bacteria corresponding to a single bacterial run, $\langle|\mathbf{x}_{tb}(T)|^2\rangle$, is calculated in which the angle brackets indicate an average over bacterial runs. We first perform simulations for $R = 1$ and with varying number of bacterial runs to determine the number of tracer-bacterium interactions required for a statistically accurate $\langle|\mathbf{x}_{tb}T)|^2\rangle$ and then scale the number of bacterial runs proportional to R^3 for $R > 1$. We found that 10^4 interactions are enough to have the standard relative error of $\langle|\mathbf{x}_{tb}T)|^2\rangle$ below 10% for $R = 1$ and $Pe \leq 250$.

Now to obtain the diffusivity of the tracer particle, we make use of the definition of tracer diffusivity in three dimensions as one-sixth of the rate of change of the mean square tracer displacement. Since there are $(4/3)\pi R^3 n L^3$ bacteria inside the control volume of non-dimensional radius R and since each bacterium tumbles at a rate of τ^{-1}, the non-dimensional tracer diffusivity due to bacterial fluid disturbances and excluded volume interactions is given by

$$\widetilde{D_{tb,R}} = \frac{1}{6}\frac{d\langle|\mathbf{x}_{tb}(T)|^2\rangle}{dt} = \frac{4\pi R^3}{3\tau^*}\frac{\langle|\mathbf{x}_{tb}(T)|^2\rangle}{6}. \tag{2.38}$$

Since we are simulating only those bacterial runs which pass through the spherical control volume, the mean square displacements as well as the diffusivities in Eq. 2.38 are dependent upon the control volume radius R as indicated by the subscript R in Eq. 2.38. We now need to extrapolate the diffusivity calculated in Eq. 2.38 to the limit $R \to \infty$ to obtain the tracer diffusivity corresponding to an unbounded bacterial suspension and for this we make use of the scaling that $\widetilde{D_{tb}} - \widetilde{D_{tb,R}} \sim \tau^*/R$ when $R \to \infty$ in which $\widetilde{D_{tb}}$ is the bacteria induced tracer diffusivity corresponding to an unbounded suspension. This scaling arises from the fact that $|\mathbf{x}_{tb}(T)| \sim \tau^*/R^2$ at large R for those bacteria trajectories that lie outside the control volume owing to the dipolar nature of the bacterial fluid disturbance at those tracer-bacterium separation length scales. Thus in order to

extrapolate the diffusivity obtained from Eq. 2.38 we perform simulations with varying R and fit the simulation data with the expression

$$\widetilde{D_{tb,R}} = \widetilde{D_{tb}} - A\frac{\tau^*}{R} \tag{2.39}$$

where A is a constant. We found that Eq. 2.39 provides a good fit to simulations with $R = 2.5$, 3, 3.5, and 4 and we use this expression to extrapolate and determine $\widetilde{D_{tb}}$ (see the inset of Fig. 2.4(a)). We would like to emphasize that the non-dimensional bacteria-induced diffusivity $\widetilde{D_{tb}}$ obtained from the above extrapolation procedure is not purely due to the fluid disturbances created by the bacterium but consists of the effect of bacteria-tracer excluded volume interactions. This is due to the $\boldsymbol{\delta}_{ex}$ term in Eq. 2.37 which is the volume-exclusion induced tracer displacements. Nevertheless, when the excluded volume radius $R_{ex} = 0$, $\boldsymbol{\delta}_{ex} = 0$ and as a result the bacteria induced diffusivity obtained from simulations becomes of purely hydrodynamic origin.

We first perform simulations without any tracer-bacterium excluded volume interactions by setting $R_{ex} = 0$ and compare the simulation results for $\widetilde{D_{tb}}$ with the theoretical prediction of $\widetilde{D_h}$ made in the previous section. The comparison of diffusivities obtained from theory and these simulations gives insights about the effect of having bacterial fluid disturbances of magnitude comparable to the swimming speed of the bacterium. We present this comparison in Figs. 2.4(a) and (b) in which the first shows the variation of the hydrodynamic diffusivity with Pe and the second shows variation with τ^*. Symbols in both figures show data from simulations and lines show the theoretical predictions from Eq. 2.30. The inset in Fig. 2.4(a) shows that the R dependent diffusivity $\widetilde{D_{tb,R}}$ indeed varies linearly with $1/R$ as anticipated in the previous paragraph with the $1/R$ data points corresponding to $R = 2.5$, 3, 3.5, and 4. All simulations are performed with $\alpha = 2/7$ and $\gamma = 2$ as representative values and Fig. 2.4(a) is for

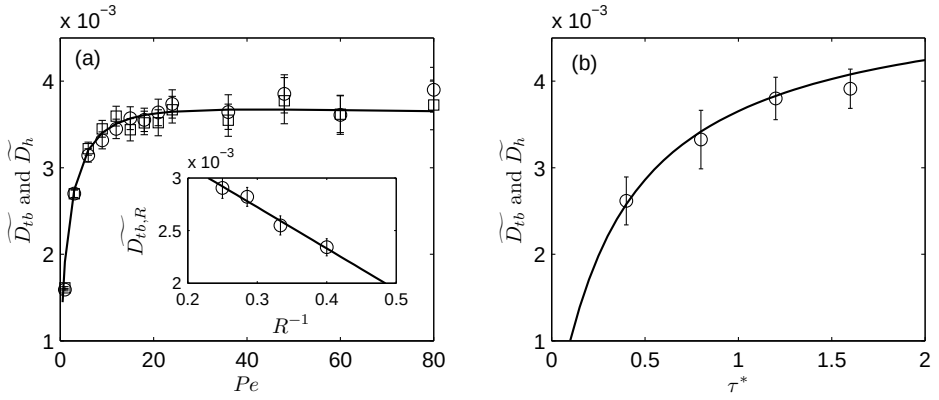

Figure 2.4: Comparison of the theoretical prediction (shown by lines) of $\widetilde{D_h}$ given in Eq. 2.30 and simulation results $\widetilde{D_{tb}}$ (shown by symbols) for varying Pe at $\tau^* = 1$ in figure (a) and for varying τ^* at $Pe = 80$ in figure (b). Circles in figure (a) are with a time step $\Delta t = 0.01$ in simulations and squares are for $\Delta t = 0.005$ and the symbols in the inset of figure (a) show the variation of the R dependent diffusivity $\widetilde{D_{tb,R}}$ with $1/R$ obtained from the simulations and the line is the linear fit of the form given in Eq. 2.39. The results are for $\alpha = 2/7$ and $\gamma = 2$. The error bars in the figure correspond to one standard error of the mean in each direction.

$\tau^* = 1$ and Fig. 2.4(b) is for $Pe = 80$. Circles and squares in Fig. 2.4(a) are for time steps $\Delta t = 0.01$ and $\Delta t = 0.005$ respectively and the agreement between these two sets of data ensures that $\Delta t = 0.01$ is adequate for converged results. The latter time step has been used for all of the simulations results discussed. It is clear from Fig. 2.4 that the simulation results agree in general well with the theoretical prediction of hydrodynamic diffusivity. Since numerical simulations have finite velocity disturbance near the bacterium compared to the swimming speed, the agreement between the latter and the theoretical results from Eq. 2.30 shows that the finiteness of the bacterial velocity disturbance compared to the swimming speed does not have a statistically significant effect on the hydrody-

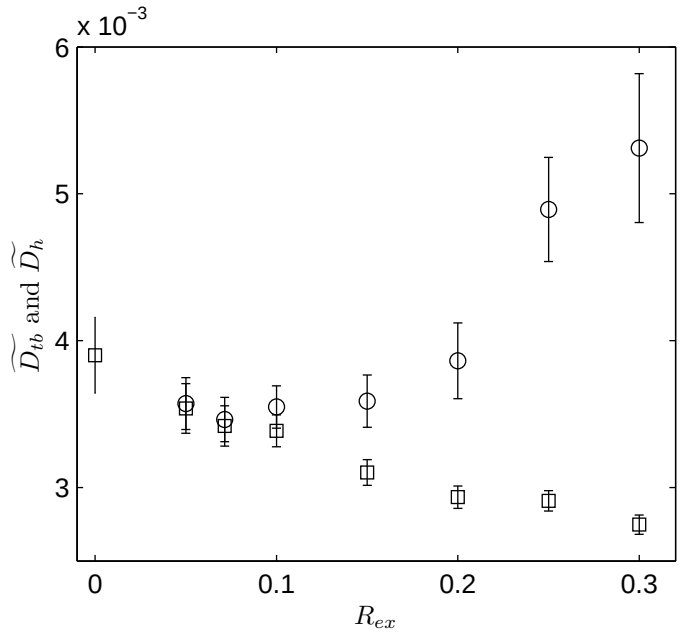

Figure 2.5: Variation of the bacteria-induced tracer diffusivity $\widetilde{D_{tb}}$ (circles) and hydrodynamic tracer diffusivity $\widetilde{D_h}$ (squares) with the non-dimensional excluded volume radius R_{ex}. Here $R_{ex} = 0.07$ (third data point from left) corresponds to a point tracer interacting with a bacterium with a finite size while the first two points correspond to tracers that can penetrate the interior of the spherocylinder representing the bacterium. The results are for $Pe = 80$, $\alpha = 2/7$, and $\gamma = 2$.

namic diffusivity.

We now proceed to investigate the effect of tracer-bacterium excluded volume interactions on the bacteria-induced diffusivity of the tracer by performing simulations with varying excluded volume radius R_{ex}. The results of these simulations are shown in Fig. 2.5 in which circles show the variation of the non-dimensional tracer diffusivity $\widetilde{D_{tb}}$ with the excluded volume radius R_{ex}. We also show the variation of the hydrodynamic contribution to the tracer diffusivity obtained from simulations with R_{ex} in Fig. 2.5 using squares. The latter is

calculated by first evolving the hydrodynamic trajectory of the tracer particle

$$\mathbf{x}_h(t+\Delta t) = \mathbf{x}_h(t) + \mathbf{u}'(\mathbf{x}(t) - \mathbf{x}_b(t))\Delta t, \tag{2.40}$$

and using the definition

$$\widetilde{D_{h,R}} = \frac{1}{6}\frac{d\langle|\mathbf{x}_h(T)|^2\rangle}{dt} = \frac{4\pi R^3}{3\tau^*}\frac{\langle|\mathbf{x}_h(T)|^2\rangle}{6}. \tag{2.41}$$

The R dependent hydrodynamic diffusivity in Eq. 2.41 is then extrapolated to the limit $R \to \infty$ by the same procedure as followed for determining $\widetilde{D_{tb}}$. In Fig. 2.5 the overall bacteria-induced tracer diffusivity $\widetilde{D_{tb}}$ is found to be first decreasing from its value at $R_{ex} = 0$ with increasing R_{ex} and thereafter increasing. Thus the bacteria-induced diffusivity of a point tracer ($R_{ex} = 0.07$) is smaller than its hydrodynamic diffusivity owing to the excluded volume of the bacterium preventing the tracer from sampling the velocity disturbances close to the bacterial axis. This is further elucidated by the observation that the hydrodynamic component of the tracer diffusivity shown in Fig. 2.5 by squares keeps decreasing with increasing in R_{ex}. However, increasing R_{ex} further causes the tracer displacements arising from excluded volume interactions with bacteria compensate for the reduced convective transport of the tracer and even enhance the tracer diffusivity beyond the case without any tracer-bacterium excluded volume. For instance, when $R_{ex} = 0.3$, the excluded volume contribution is as large as the hydrodynamic contribution to the diffusivity and the tracer diffusivity is larger than the case without any excluded volume. It is thus possible in the experiment of Wu & Libchaber (2000) that a significant portion of the enhancement in tracer diffusivity came from direct collisions between colloidal tracer particles and bacteria. In that case, the effect of excluded volume would be further enhanced since the confinement of the suspension to a quasi-to-dimensional geometry leads to an increased frequency of tracer-bacterium collisions.

2.5 Experiment

To assess the accuracy of our theoretical and simulation results for the hydrodynamic diffusivity tracers in dilute bacterial suspensions, we measure the effective diffusivity of colloidal tracer particles in a suspension of run-tumble bacteria at bacterial concentrations that range from dilute suspensions $nL^3 = 0.24$ to moderately concentrated suspensions $nL^3 = 5.6$. Here nL^3 is a non-dimensional measure of the bacteria concentration that is on the order of the volume fraction of spheres that circumscribe the bacterium cell and its flagella bundle (spheres of diameter L). The bacteria used in the experiment are from the wild-type *E. Coli* strain RP437 and the colloidal tracer particles are fluorescent (red) polystyrene beads of diameter 1.01μm (Bangs Laboratories, Fishers, IN). To prepare the bacterial suspension, the cells were first grown in Tryptone broth (10 g bacto-tryptone powder and 5 g sodium chloride per liter of 10 mM phosphate buffer) overnight in a rotary water bath kept at $30°C$ and rotated at 200 rpm. The overnight culture was then diluted into fresh tryptone broth by a factor of 25 and rotated again in the water bath until the bacteria entered the mid-exponential growth phase which corresponds to an optical density of the suspension OD_{600} around 0.5. The cells were then centrifuged, washed, and resuspended in a motility medium consisting of 10mM lactic acid, 0.1 mM EDTA, 1 μM L - methionine, and 50 mM glucose. Glucose was added to sustain the motility in the event that the oxygen might be depleted due to bacterial respiration especially at higher bacteria concentrations (Adler & Templeton, 1967). The final concentration of bacteria in the suspension was determined by measuring the OD_{600} optical density of the suspension using a spectrophotometer calibrated by means of the Helber bacteria counting chamber (Hawksley, Sus-

sex, UK). Fluorescent polystyrene tracer particles were added to the bacterial suspension to a final volume fraction of around 0.016%. Experiments were performed with bacterial concentrations ranging from $6.9*10^8$ bacteria per milliliter to $1.64 * 10^{10}$ bacterial per milliliter corresponding to non-dimensional bacterial concentration nL^3 in the range 0.24 to 5.61.

The bacteria - tracer suspension was then loaded into the three-channel microfluidic device developed by Cheng *et al.* (2007). The device mainly consists of a set of three channels each of depth 170 μm and width 400 μm patterned on a 1 mm thick agarose gel membrane. Only the middle channel was loaded with the bacteria - tracer suspension and channels on either sides were filled with the motility medium which helped keep the bacterial suspension oxygenated. Movies of tracer particles were then taken at the mid-plane of the channel using a fluorescent microscope (Olympus IX-51 microscope with 20x objective lens and EXFO X-Cite 120 fluorescent illumination system) at a rate of 30 frames per second using a CCD camera (Cascade 512B from Photometrics, Tucson, AZ). The positions of the tracer particles were tracked using an in-house MATLAB code (Liao *et al.*, 2007) and the effective diffusivity of tracer particles was obtained from the slope of their mean square displacement versus time curve. While the inlets and outlets of all three channels were sealed by using PDMS filled pipette tips to reduce any evaporation induced drift flow, the sealing was occasionally imperfect resulting in slow, bulk flow of the suspension along the length of the channel with velocities of the order of 3 μm/s. To avoid error due to the bulk flow induced particle motion in calculating the effective diffusivity of tracer particles, we compute the mean square tracer displacement only in the transverse direction of the channel and use the one dimensional diffusion relation $D_{eff} = \lim_{t\to\infty}(1/2)(d/dt)\langle y^2\rangle$ to calculate the effective diffusivity of

the tracer with y being its displacement along the transverse channel direction. The shear rate based on the drift velocity and the smallest channel dimension is of the order of $10^{-2}s^{-1}$ and since the latter is much smaller than the bacterial tumbling frequency ($\approx 1s^{-1}$), the shear re-orientation of bacteria would be negligible so that the suspension may still be considered as isotropic.

A control experiment was carried out using a suspension of tracer particles in the same suspending medium (the motility medium) in the absence of bacteria to measure the Brownian diffusivity of tracer particles in the motility medium. The measured Brownian diffusivity is $D = 0.48 \pm 0.02\mu m^2/s$ with 95% confidence level which is close to the value of diffusivity of the tracers $D \approx 0.45\mu m^2/s$ in water obtained from the Stokes-Einstein relationship at an ambient temperature of $22°C$. In Figs. 2.6(a) and (b) we show a comparison between typical tracks obtained for the control case and the case with highest bacteria concentration ($nL^3 = 5.61$) and in Fig. 2.6(c) we show the comparison between typical mean square displacement versus time curves for those to cases. The typical movies captured by the camera for the control case and the $nL^3 = 5.61$ case are available in the supplementary materials as files "SupplementaryMovie1.avi" and "SupplementaryMovie2.avi" respectively. To obtain the swimming speed U_s and the mean tumbling frequency τ^{-1}, the bacteria were induced to express green fluorescent protein using $0.5mM$ of isopropyl β-D-1-thiogalactopyranoside (see Kalinin *et al.* (2009)) and the swimming cells were imaged at low bacterial concentration of $6 * 10^8$ cells per milliliter (see the movie file "SupplementaryMovie3.avi" in supplementary materials). Again to avoid errors due to drift motion in the channel, only the component of bacterial velocity in the transverse channel direction was used to compute the swimming speed and the mean run time τ. The three dimensional bacterial swim-

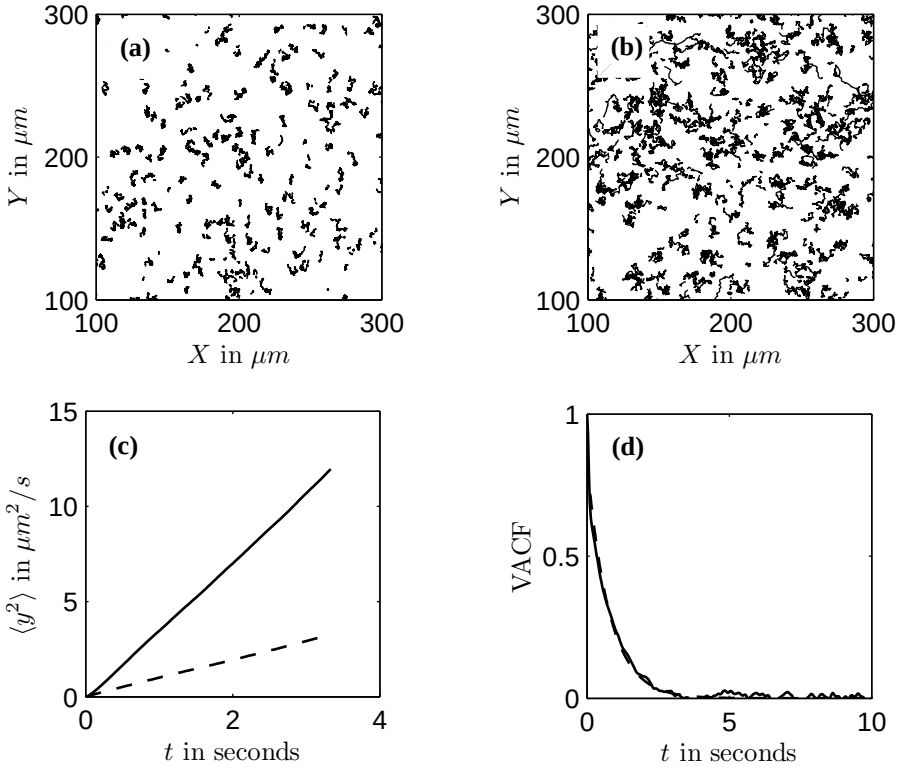

Figure 2.6: Typical tracer particle tracks obtained for (a) control experiment with no bacteria and (b) a bacterial suspension with a cell concentration of $1.64 * 10^{10}$ bacteria per milliliter corresponding to $nL^3 = 5.61$, (c) typical mean square displacement of the tracer versus time curve for the control case (dashed line) and for the case with $nL^3 = 5.6$ (solid line), and (d) normalized bacteria velocity autocorrelation versus time obtained from the experiment (solid line) and the exponential fit to the experimental data (dashed line).

ming speed is obtained from the one-dimensional measurements through the relationship that the average magnitude of the one-dimensional projection of a vector in three dimensional space is half of the magnitude of the vector if the latter is distributed isotropically. The mean run time τ has been obtained by fitting the normalized autocorrelation of the bacterial swimming velocity along the transverse direction defined as $VACF = \langle U_{sy}(0)U_{sy}(t)\rangle/\langle U_{sy}(0)^2\rangle$ with an exponentially decaying curve of the form $A\exp(-t/\tau)$ where A is a fitting parameter as seen in Fig. 2.6(d). The swimming speed and the run time of bacteria measured from the experiment are $U_s = 12.54\mu m/s$ and $\tau = 0.78s$. These values of U_s and τ with the assumed bacterial length of $L = 7\mu m$ and measured mean $D = 0.48\mu m^2/s$ yield $Pe = 182.88$ and $\tau^* = 1.40$ and we compare the experimental results on D_{eff} and estimates of the latter from the averaged equation theory and pairwise simulations at the aforementioned values of parameters along with $\gamma = 2$ and $\alpha = 2/7$. The pair-simulations are with a non-dimensional excluded volume radius of $R_{ex} = 0.14$ which corresponds to the tracer particle size used in the experiment.

Figure 2.7 shows the comparison of the effective tracer diffusivity versus bacteria concentration relationship obtained from the experiment (symbols), theory using averaged equations (solid line), and numerical simulations of pair-interactions (dash-dot line). The dash-dot line is the least square linear fit to the effective diffusivity values obtained from the experiment so that its slope is the quantity $\widetilde{D_h}U_sL$ and its numerical value is $0.18\pm0.01\mu m^2/s$ with 95% confidence level. The theoretical prediction of $\widetilde{D_h}U_sL$ at the Pe and τ^* corresponding to the experiment is $0.34\mu m^2/s$ which is larger than the experimentally obtained value by factor of 1.89. The prediction of $\widetilde{D_h}U_sL$ by the numerical simulation of pair-interactions which account for the excluded volume between bacteria and tracer

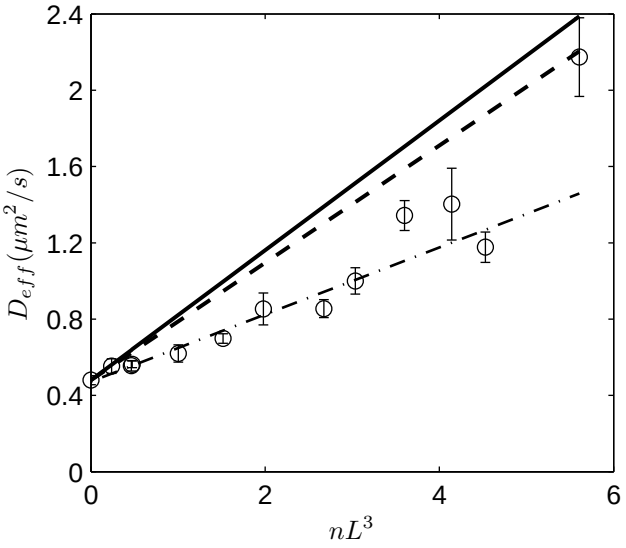

Figure 2.7: Variation of the effective diffusivity of colloidal tracer particles with non-dimensional bacteria concentration obtained from the experiment (symbols), theory (solid line), and simulations with excluded volume interactions between bacteria and tracer particles (dashed line). The dash-dot line is the linear fit to the experimental data (mean values) and error bars on the experimental data show 95% confidence interval obtained from nine sets of tracer particle tracks for each data point. Theory and simulation data are for $Pe = 182.88$ and $\tau^* = 1.40$ which are based on $U_s = 12.54\mu m/s$, $\tau = 0.78s$, $D = 0.48\mu m^2/s$, and $L = 7\mu m$. We also have $\gamma = 2$ and $\alpha = 2/7$ in both and theory and simulation and the latter is with $R_{ex} = 0.14$ based on the typical diameters $1\mu m$ and $1.01\mu m$ for the bacterial cell-body and the tracer particle respectively.

particles is $0.31\mu m^2/s$ which is 1.72 times larger than the value obtained from the experiment. Thus while the theory and simulations presented in previous sections correctly predict the order of magnitude of the bacterial contribution to the tracer diffusivity, they overestimate the diffusivity by nearly a factor of 2. The most probable cause of the discrepancy between experiment and theory is that the exact geometrical parameters of the bacterium are unknown in the experiment. The effective tracer diffusivity is extremely sensitive to the over-

all length of the bacterium since the bacterial contribution the tracer diffusivity scales like the fourth power of bacterial length (see Eq. 2.29). The uncertainty in the overall bacterial length available in the literature is large primarily due to the uncertainty in the experimentally measured length of bacterial flagella bundles. For instance, while DePamphilis & Adler (1971*a*) and DePamphilis & Adler (1971*b*) through electron microscopy measured the flagella length to be around $5\mu m$ for *E. Coli* K-12 (the parent strain of the *E. Coli* RP437 strain used in our experiments Sourjik & Berg (2000)) Turner *et al.* (2000)'s measurements on flagellar bundles of *E. Coli* AW405 (a derivative strain of *E. Coli* K-12 (Tisa & Adler, 1992)) labeled with fluorescent dyes gave a mean flagella length varying from $5.6\mu m$ to $7.3\mu m$ with the standard deviation in the range 2.4 - 2.9 μm depending on the type of fluorescent dye used to label the flagella bundle. Thus it may be the case that the overall length of the bacterium used in our experiments is smaller than $7\mu m$ so that the theory with $L = 7\mu m$ overestimates the tracer diffusivity. Nonetheless, considering the possible uncertainty in the bacterial geometry, our pairwise theory and simulations are successful in predicting the tracer diffusivity in three-dimensional, isotropic, and quiescent suspensions of run-tumble bacteria.

Even though, the simple pairwise treatment employed in our theory and simulation is expected to be accurate only for a dilute suspension $nL^3 \ll 1$, it is remarkable that the aforementioned treatment continues to be reliable even when the suspension is moderately dense with nL^3 of order unity. This is due to the fact that bacteria being slender objects create relatively weak hydrodynamic disturbances. An estimate of the effect of hydrodynamic interactions on the force per unit length exerted on the fluid which would control the magnitude of the hydrodynamic diffusion as well as the stress in the suspension can be

made by reference to literature on passive fibers. Mackaplow & Shaqfeh (1996) derived a theory for the effective viscosity of passive fibers resulting from two fiber hydrodynamic interactions. For the fiber concentration equal to the highest bacteria concentration reached in our experiment ($nL^3 \approx 6$) and for the fiber aspect ratio equal to the overall bacterial aspect ratio (defined as L/d) of 7 , the two-particle correction to the effective viscosity is just 4% of the single-particle contribution. Thus one may expect the present theory to be accurate even at the highest bacterial concentration reached in the experiment. However, beyond a critical bacterial concentration given by $(nL^3)_{crit} = (5/C)L/(U_s\tau)$ where $C = \alpha/(2M)$ is the bacterial dipole strength non-dimensionalized by $\mu U_s L^2$, a bacterial suspension undergoes an instability driven by the coupling between the bacterial orientation field and the fluid velocity field (Subramanian & Koch, 2009). The instability gives rise to macroscopic fluid motion in the suspension and in that situation, the tracer diffusivity calculation presented in this paper no longer holds. For the typical bacterial geometry considered in this paper $(nL^3)_{crit} = 4.4$ and a close examination of Fig. 2.7 reveals that the highest concentration data point ($(nL^3)_{crit} = 5.6$) has a significantly larger tracer diffusivity than the prediction from the linear fit of the experimental data. A detailed discussion on the applicability of dilute theory for bacteria suspensions even at moderately large concentrations can be found in Subramanian & Koch (2009).

2.6 Concluding discussion

In the preceding sections, we have provided a theory for the transport of a Brownian tracer particle in an isotropic, homogeneous, and unbounded suspension of swimming bacteria performing run - tumble random walks. The theory is

based on a Fickian constitutive law that relates the average convective flux arising from bacterial velocity disturbances with the average tracer concentration gradient through a hydrodynamic diffusion coefficient with the average being defined over all possible pair-interactions between a tracer particle and a bacterium whose fluid velocity disturbance is modeled as that due to a line distribution of forces along its axis. The primary result of the theory is an integral expression for the value of the hydrodynamic diffusion coefficient as a function of a Peclet number $Pe = U_s L/D$ which measures the relative importance of the convective motion due to the bacterial swimming and the diffusive motion of the tracer and the non-dimensional persistence length of the bacterium $\tau^* = U_s \tau/L$. For $Pe \ll 1$ and $\tau^* \geq O(1)$ $D_h \sim nL^3 U_s L\sqrt{U_s^2 \tau/D}$ and when $Pe \gg 1$ and $\tau^* = O(1)$, the hydrodynamic diffusivity follows a purely convective scaling of $D_h \sim nL^3 U_s L\phi(\tau^*)$ but with a dependence on τ^*. When both Pe and τ^* are much larger than one, the hydrodynamic diffusivity is independent of τ^* so that $D_h \sim nL^3 U_s L$. While the hydrodynamic tracer diffusivity increases monotonically with the bacterial persistence length, it has a non-monotonic dependence on Pe with a peak around Pe of order 10. This peak may be attributed to the fact that the velocity disturbance of the bacterium is an odd function of relative positions and the combined effects of diffusion and convection allow the tracer to sample a less symmetric range of relative position leading to a larger net displacement. The theoretical predictions for the most relevant parametric regime of $Pe \geq 1$ and $\tau^* = O(1)$ has been verified through explicit simulations of pair interactions between bacteria and tracer particles and the simulations also revealed the weakening effect of excluded volume of the bacteria and tracer particles on hydrodynamic diffusivity. Finally, the results of our experiments with suspensions of swimming bacteria and colloidal particles as tracers are in

excellent agreement with predictions from theory and simulations.

An important insight from this investigation is the dependence of hydrodynamic diffusivity of the tracer on its Brownian diffusivity. It is clear from Fig. 2.2 that the bacteria induced mixing is in general smaller for smaller tracers with relatively large Brownian diffusivity. For instance, oxygen has $Pe \approx 0.05$ based on its molecular diffusivity(Hillesdon & Pedley, 1996) $D = 2000\mu m^2/s$, the bacterial swimming speed $U_s = 15\mu m/s$, and bacterial length $L = 7\mu m$. For a typical tumbling frequency of $\tau^{-1} = 1s^{-1}$, the dimensional hydrodynamic diffusivity of oxygen would be around $0.07nL^3\mu m^2/s$ which would require physically impossible bacterial concentrations of $nL^3 = O(10^3)$ in order to be comparable to the molecular diffusivity. Thus bacteria induced mixing is irrelevant for small molecules. On the other hand, hydrodynamic diffusion can be significant in the case of chemical signaling between bacteria mediated through membrane vesicles. It is known that bacteria such as *E. Coli* or *P. aeruginosa* produce membrane vesicles with diameters of the order of 100 nm which help transport inter-bacterial signaling molecules (Mashburn & Whiteley, 2005; Schooling & Beveridge, 2006; Wu *et al.*, 2011). The typical Brownian diffusivity of these vesicles is of the order of $5\mu m^2/s$ based on the Stokes - Einstein relationship which yields Pe of the order of 10 for typical bacterial speed and length. The hydrodynamic diffusivity of these vesicles is then of the order of $0.5nL^3\mu m^2/s$ which is comparable to their Brownian diffusivity even at moderate bacteria concentrations with $nL^3 = 5$. Enhanced transport of chemical signals between bacteria could play an important role in signaling-dependent bacterial behavior such as quorum sensing (Mashburn & Whiteley, 2005).

2.7 Appendix A: Asymptotic evaluation of $\widetilde{D_h}$ for $Pe \ll 1$ and $\tau^* \geq O(1)$

We first re-write Eq. 2.30 as an integral over a spherical domain defined by $\mathbf{k} \cdot \mathbf{p} = k\cos\theta$ as

$$\widetilde{D_h} = \frac{\tau^*}{96\pi^4 M^2} \int d\mathbf{p} \int_0^{2\pi} d\phi \int_0^{\pi} d\theta \int_0^{\infty} dk \frac{\sin^3\theta F(k\cos\theta)F(-k\cos\theta)}{k^2\left(1 + ik\tau^*\cos\theta + \frac{\tau^*}{Pe}k^2\right)}. \quad (2.42)$$

The integral over $\mathbf{p}$ and ϕ together yields $8\pi^2$ and since the product $F(k\cos\theta)F(-k\cos\theta) = \alpha^2 k^2\cos^2\theta/4 + O(k^4)$ for $k \ll 1$, the dominant contribution to the integral for the case with $Pe \ll 1$ and $\tau^* \geq O(1)$ comes from $k = O(\sqrt{Pe/\tau^*})$. Thus at the the leading order we simply have

$$\widetilde{D_h} = \frac{\alpha^2\tau^*}{48\pi^2 M^2} \int_0^{\pi} d\theta \sin^3\theta\cos^2\theta \int_0^{\infty} \frac{dk}{1 + \frac{\tau^*}{Pe}k^2} = \frac{\alpha^2\sqrt{Pe\tau^*}}{360\pi M^2} \quad (2.43)$$

2.8 Appendix B: Asymptotic evaluation of $\widetilde{D_h}$ for $Pe \gg 1$ and $\tau^* \gg 1$

The leading contribution to the integral in Eq. 2.30 can be calculated by simply dropping the k^2/Pe term in Eq. 2.30 and taking the limit of the integral for $\tau^* \to \infty$. The resulting expression when written as an integral over cylindrical coordinates $(k_\parallel, k_\perp)$ with the $k_\parallel$ axis along $\mathbf{p}$ takes the form

$$\widetilde{D_h} = \lim_{\tau^*\to\infty} \frac{1}{12\pi^2 M^2} \int_{-\infty}^{\infty} dk_\parallel \int_0^{\infty} dk_\perp \frac{k_\perp^3 F(k_\parallel)F(-k_\parallel)}{\left(k_\parallel^2 + k_\perp^2\right)^3\left[\frac{1}{\tau^*} + ik_\parallel\right]} \quad (2.44)$$

The integral over $k_\perp$ space in Eq. 2.44 is equal to $1/(4k_\parallel^2)$ so that the integral in Eq. 2.44 can be written in the following form by multiplying both the numerator

and the denominator by the complex conjugate of the denominator $1/\tau^* - ik_\parallel$

$$\widetilde{D_h} = \lim_{\tau^* \to \infty} \frac{1}{48\pi^2 M^2} \int_{-\infty}^{\infty} dk_\parallel \frac{\left[\frac{1}{\tau^*} - ik_\parallel\right] F(k_\parallel)F(-k_\parallel)}{k_\parallel^2 \left[\frac{1}{\tau^{*2}} + k_\parallel^2\right]}. \tag{2.45}$$

Since the product $F(k_\parallel)F(-k_\parallel)$ is even in $k_\parallel$, the imaginary part of the integral in Eq. 2.45 vanishes and it is clear from the denominator of the integrand in Eq. 2.45 that in the limit of $\tau^* \to \infty$ the dominant contribution to the integral comes from the region of $k_\parallel = O(1/\tau^*)$. We now rescale $k_\parallel$ by $1/\tau^*$ to yield the variable $\bar{k}_\parallel = k_\parallel \tau^*$ and rewrite Eq. 2.45 in terms of $\bar{k}_\parallel$ as

$$\widetilde{D_h} = \lim_{\tau^* \to \infty} \frac{\tau^{*2}}{48\pi^2 M^2} \int_{-\infty}^{\infty} d\bar{k}_\parallel \frac{F(\bar{k}_\parallel/\tau^*)F(-\bar{k}_\parallel/\tau^*)}{\bar{k}_\parallel^2 \left[1 + \bar{k}_\parallel^2\right]}. \tag{2.46}$$

The dominant contribution to the integral in Eq. 2.46 comes from $\bar{k}_\parallel = O(1)$ and hence in the limit $\tau^* \to \infty$, one may replace the product $F(\bar{k}_\parallel/\tau^*)F(-\bar{k}_\parallel/\tau^*)$ by its Taylor series near $\bar{k}_\parallel = 0$, $F(\bar{k}_\parallel)F(-\bar{k}_\parallel) = \alpha^2 \bar{k}_\parallel^2/(4\tau^{*2})$ to yield

$$\widetilde{D_h} = \lim_{\tau^* \to \infty} \frac{\alpha^2}{192\pi^2 M^2} \int_{-\infty}^{\infty} d\bar{k}_\parallel \frac{1}{1 + \bar{k}_\parallel^2} = \frac{\alpha^2}{192\pi M^2}. \tag{2.47}$$

Acknowledgement

This work is supported by NSF Grant CBET-1066193.

Bibliography

ADLER, J. & TEMPLETON, B. 1967 The effect of environmental conditions on the motility of escherichia coli. *Journal of General Microbiology* **46** (2), 175–184.

ALON, URI, CAMARENA, LAURA, SURETTE, MICHAEL G, Y ARCAS, BLAISE AGUERA, LIU, YI, LEIBLER, STANISLAS & STOCK, JEFFRY B 1998 Response regulator output in bacterial chemotaxis. *EMBO J.* **17** (15), 4238–4248.

ARIS, R. 1956 On the dispersion of a solute in a fluid flowing through a tube. *Proceedings of the Royal Society of London. Series A. Mathematical and Physical Sciences* **235** (1200), 67–77.

BERG, H C 1975 Chemotaxis in bacteria. *Annual Review of Biophysics and Bioengineering* **4** (1), 119–136.

BERG, H C & TURNER, L 1995 Cells of escherichia coli swim either end forward. *Proceedings of the National Academy of Sciences* **92** (2), 477–479.

CHENG, S. Y., HEILMAN, S., WASSERMAN, M., ARCHER, S., SHULER, M. L. & WU, M. 2007 A hydrogel-based microfluidic device for the studies of directed cell migration. *Lab Chip* **7**, 763–769.

DEPAMPHILIS, M. L. & ADLER, JULIUS 1971*a* Fine structure and isolation of the hook-basal body complex of flagella from escherichia coli and bacillus subtilis. *Journal of Bacteriology* **105** (1), 384–395.

DEPAMPHILIS, M. L. & ADLER, JULIUS 1971*b* Purification of intact flagella from escherichia coli and bacillus subtilis. *Journal of Bacteriology* **105** (1), 376–383.

DRESCHER, KNUT, DUNKEL, JRN, CISNEROS, LUIS H., GANGULY, SUJOY & GOLDSTEIN, RAYMOND E. 2011 Fluid dynamics and noise in bacterial cell-cell and cellsurface scattering. *Proceedings of the National Academy of Sciences* **108** (27), 10940–10945.

HAPPEL, J. & BRENNER, H. 1973 *Low Reynolds number hydrodynamics*. Noordhoff International Publishing.

HERNANDEZ-ORTIZ, J. P., STOLTZ, C. G. & GRAHAM, M. D. 2005 Transport and collective dynamics in suspensions of confined swimming particles. *Phys. Rev. Lett.* **95**, 204501.

HERNANDEZ-ORTIZ, JUAN P, UNDERHILL, PATRICK T & GRAHAM, MICHAEL D 2009 Dynamics of confined suspensions of swimming particles. *Journal of Physics: Condensed Matter* **21**, 204107 (13pp).

HILLESDON, A. J. & PEDLEY, T. J. 1996 Bioconvection in suspensions of oxytactic bacteria: linear theory. *J. Fluid Mech.* **324**, 223–259.

HINCH, E. J. 1977 An averaged-equation approach to particle interactions in a fluid suspension. *Journal of Fluid Mechanics* **83**, 695–720.

KALININ, Y. V., JIANG, L., TU, Y. & WU, W. 2009 Logarithmic sensing in escherichia coli bacterial chemotaxis. *Biophys. J.* **96**, 2439 – 2448.

KIM, M. J. & BREUER, K. S. 2004 Enhanced diffusion due to motile bacteria. *Phys. Fluids* **16**, L78–L81.

KOCH, DONALD L. & BRADY, JOHN F. 1985 Dispersion in fixed beds. *Journal of Fluid Mechanics* **154**, 399–427.

LAUGA, E. & POWERS, T. R. 2009 The hydrodynamics of swimming microorganisms. *Rep. Prog. Phys.* **72**, 096601.

LIAO, QIAN, SUBRAMANIAN, GANESH, DELISA, MATTHEW P., KOCH, DONALD L. & WU, MINGMING 2007 Pair velocity correlations among swimming escherichia coli bacteria are determined by force-quadrupole hydrodynamic interactions. *Physics of Fluids* **19** (6), 061701.

MACKAPLOW, MICHAEL B. & SHAQFEH, ERIC S. G. 1996 A numerical study of the rheological properties of suspensions of rigid, non-brownian fibres. *Journal of Fluid Mechanics* **329**, 155–186.

MASHBURN, LAUREN M & WHITELEY, MARVIN 2005 Membrane vesicles traffic signals and facilitate group activities in a prokaryote. *Nature* **437** (7057), 422–425.

MIÑO, GASTÓN, MALLOUK, THOMAS E., DARNIGE, THIERRY, HOYOS, MAURICIO, DAUCHET, JEREMI, DUNSTAN, JOCELYN, SOTO, RODRIGO, WANG, YANG, ROUSSELET, ANNIE & CLEMENT, ERIC 2011 Enhanced diffusion due to active swimmers at a solid surface. *Phys. Rev. Lett.* **106**, 048102.

SAINTILLAN, D. & SHELLEY, M. J. 2007 Orientational order and instabilities in suspensions of self-locomoting rods. *Phys. Rev. Lett.* **99**, 058102.

SCHOOLING, SARAH R. & BEVERIDGE, TERRY J. 2006 Membrane vesicles: an overlooked component of the matrices of biofilms. *Journal of Bacteriology* **188** (16), 5945–5957.

SINGH, RAJVEER & OLSON, MIRA STONE 2011 Transverse mixing enhancement due to bacterial random motility in porous microfluidic devices. *Environmental Science and Technology* **45** (20), 8780–8787.

SOURJIK, VICTOR & BERG, HOWARD C. 2000 Localization of components of the chemotaxis machinery of escherichia coli using fluorescent protein fusions. *Molecular Microbiology* **37** (4), 740–751.

STOCKER, ROMAN 2011 Reverse and flick: Hybrid locomotion in bacteria. *Proceedings of the National Academy of Sciences* **108** (7), 2635–2636.

SUBRAMANIAN, G. & KOCH, D. L. 2009 Critical bacterial concentration for the onset of collective swimming. *J. Fluid Mech.* **632**, 359–400.

TAYLOR, GEOFFREY 1953 Dispersion of soluble matter in solvent flowing slowly through a tube. *Proceedings of the Royal Society of London. Series A. Mathematical and Physical Sciences* **219** (1137), 186–203.

TISA, L S & ADLER, J 1992 Calcium ions are involved in escherichia coli chemotaxis. *Proceedings of the National Academy of Sciences* **89** (24), 11804–11808.

TURNER, LINDA, RYU, WILLIAM S. & BERG, HOWARD C. 2000 Real-time imaging of fluorescent flagellar filaments. *Journal of Bacteriology* **182** (10), 2793–2801.

UNDERHILL, P. T., HERNANDEZ-ORTIZ, J. P. & GRAHAM, M. D. 2008 Diffusion and spatial correlations in suspensions of swimming particles. *Phys. Rev. Lett.* **100**, 248101.

WU, MINGMING, ROBERTS, JOHN W., KIM, SUE, KOCH, DONALD L. & DELISA, MATTHEW P. 2006 Collective Bacterial Dynamics Revealed Using a Three-Dimensional Population-Scale Defocused Particle Tracking Technique. *Appl. Environ. Microbiol.* **72** (7), 4987–4994.

WU, X. L. & LIBCHABER, A. 2000 Particle diffusion in a quasi-two-dimensional bacterial bath. *Phys. Rev. Lett.* **84**, 3017–3020.

WU, YILIN, HOSU, BASARAB G. & BERG, HOWARD C. 2011 Microbubbles reveal chiral fluid flows in bacterial swarms. *Proceedings of the National Academy of Sciences* **108** (10), 4147–4151.

CHAPTER 3

CHEMOTAXIS DRIVEN INSTABILITY OF A CONFINED BACTERIAL SUSPENSION

3.1 Abstract

A suspension of bacteria in a thin channel or film subject to a gradient in the concentration of a chemoattractant, will develop, in the absence of an imposed fluid flow, a steady bacteria concentration field that depends exponentially on cross-stream position. Above a critical bacteria concentration, this quiescent base state is unstable to a steady convective motion driven by the active stresses induced by the bacteria's swimming. Unlike previously identified long wavelength instabilities of active fluids, this instability results from coupling of the bacteria concentration field with the disturbance flow.

3.2 Theory and results

Observations that suspensions of swimming bacteria with no imposed stresses or chemical gradients exhibit collective motions on length scales large compared with an individual cell have inspired simulations of hydrodynamically interacting Stokesian swimmers and continuum theories for bacteria suspensions (Koch & Subramanian, 2011). The continuum theories feature an active stress resulting from the force dipoles the cells exert as they swim. The homogeneous, quiescent state of an unbounded suspension governed by these equations has been shown

This chapter is reprinted from T. V. Kasyap and Donald L. Koch, *Physical Review Letters* **108**, 038101 (2012).

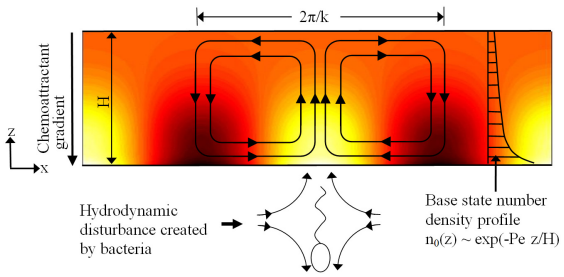

Figure 3.1: Mechanism of the chemotaxis driven instability. Individual bacteria align in the direction of the chemical gradient leading to dipolar fluid velocity disturbances. At the continuum level, the instability manifests itself through the perturbed number density field represented by color contours and the streamline pattern illustrated within the channel. Brighter regions indicate higher bacteria concentrations. The fluid motion acting on the base state number density profile sweeps bacteria toward the region of high perturbed bacteria concentration leading to growth of the perturbation.

to be unstable to perturbations in bacteria orientation distribution that couple with the fluid shearing induced by the active stresses (Koch & Subramanian, 2011; Simha & Ramaswamy, 2002; Saintillan & Shelley, 2008*a*,*b*; Subramanian & Koch, 2009). Since the purpose of bacterial motility is to allow cells to respond to chemical cues in their environment, it is of interest to explore how bacterial collective motion may be altered by chemical gradients. In this Letter, we show that bacteria suspensions exhibit a new type of instability (illustrated in Fig. 4.2) when the cells' swimming motion is biased due to a gradient of a chemical attractant in a confined channel or liquid film. The new instability involves coupling of active stress induced fluid convection with the bacteria concentration field.

Two recent experimental studies suggest that bacteria do exhibit enhanced convection in the presence of chemoattractant gradients. Kim & Breuer (2007) observed a significant increase in the hydrodynamically induced diffusivity of

a fluorescent molecule in a suspension of wild type *E. Coli* as the concentration gradient of an attractant was increased. Sokolov *et al.* (2009) studied the dynamics of thin films of aqueous suspensions of aerobic *B. Subtilis* cells. As they increased the thickness of these films, they observed a transition from spatially homogeneous, coherent motion in the plane of the film to a strongly convective, spatially inhomogeneous three dimensional motion. The onset of convective motion coincided with the development of cross-film gradients of oxygen, which acts as an attractant for the cells. While gravitational forces due to cell concentration variations can lead to "bio-convection" (Pedley & Kessler, 1992; Hillesdon & Pedley, 1996), the film thickness and associated Rayleigh number in Sokolov *et al.* (2009)'s experiment was too small to admit such an instability. We suggest instead that the motion was induced by an instability associated with the active stress of chemotactic bacteria.

While chemical attractants are often consumed or produced by bacteria, the simplest setting in which to explore chemical effects on the motion of a bacteria suspension is that illustrated in Fig. 1, where a linear gradient is imposed across a channel of thickness H in the z direction and infinite extent in the x direction with no slip walls. Cheng *et al.* (2007) have designed an apparatus where a linear gradient of an attractant, such as Me-Asp (α-methyl-DL-aspartate) that is not consumed by bacteria (Mesibov & Adler, 1972) and has a diffusivity large compared with that of the cells, can be established by the attractant diffusing across a sealed micro-channel sandwiched between source and sink channels.

In the absence of velocity and chemical gradients, bacteria such as *E. Coli* or *B. Subtilis* perform an unbiased random walk comprised of intervals of persistent swimming lasting about $\tau_0 \approx 1$s punctuated by short intervals of 'tum-

bling' (Berg, 2003). The state of a dilute bacterial suspension can be specified by the singlet probability density $\Omega(\mathbf{x}, \mathbf{p}, t)$ where $\mathbf{p}$ and $\mathbf{x}$ are the orientation and the position of a bacterium (Koch & Subramanian, 2011; Saintillan & Shelley, 2008*a*,*b*; Subramanian & Koch, 2009). $\Omega(\mathbf{x}, \mathbf{p}, t)$ satisfies a Boltzmann-like equation with the tumbling of the bacterium being modelled as a Markov process (Subramanian & Koch, 2009). On length scales much larger than the persistence length $U\tau_0$ where U is the swimming speed of the bacteria, $\Omega(\mathbf{x}, \mathbf{p}, t)$ can be decomposed into a number density field $n(\mathbf{x}, t)$ and an orientation field $f(\mathbf{p}, t)$. In the absence of fluid flow, the steady-state orientation distribution $f(\mathbf{p})$ can be obtained by equating the rate $f(\mathbf{p})/\tau$ at which cells tumble away from orientations near $\mathbf{p}$ with the rate at which cells tumble into the region near $\mathbf{p}$. Assuming for simplicity that pre- and post-tumble orientations are uncorrelated, the latter rate is $\frac{1}{4\pi}\int f(\mathbf{p})/\tau d\mathbf{p}$ (Subramanian & Koch, 2009). In presence of a chemoattractant gradient, the bacteria bias their random walk by reducing τ^{-1} when moving up the gradient and leaving it unaltered when swimming down the gradient (Berg, 2003), so that τ^{-1} has been described by (Brown & Berg, 1974; Chen *et al.*, 2003):

$$\tau^{-1} = \begin{cases} \tau_0^{-1} \exp(-\zeta \mathbf{p}\cdot\mathbf{g}) & \text{if } \mathbf{p}\cdot\mathbf{g} > 0, \\ \tau_0^{-1} & \text{if } \mathbf{p}\cdot\mathbf{g} \leq 0, \end{cases} \tag{3.1}$$

where $\mathbf{g} = -\mathbf{e}_z$ is the unit vector parallel to the chemical gradient, $\zeta = \chi U G$, G is the magnitude of the gradient, and χ is the sensitivity of bacteria to the attractant. Using the linearized form of Eq. 3.1 for weak chemotaxis, $\zeta \ll 1$, the orientation field obtained by equating the rates of direct and inverse events (Subramanian *et al.*, 2011) is

$$f(\mathbf{p}) = \begin{cases} \frac{1}{4\pi}\left[1 + (\mathbf{p}\cdot\mathbf{g} - 1/4)\zeta\right] + O(\zeta^2) & \text{if } \mathbf{p}\cdot\mathbf{g} > 0, \\ \frac{1}{4\pi}\left[1 - \zeta/4\right] + O(\zeta^2) & \text{if } \mathbf{p}\cdot\mathbf{g} \leq 0, \end{cases} \tag{3.2}$$

The resulting mean orientation $\langle \mathbf{p} \rangle = (1/6)\zeta \mathbf{g}$ leads to a mean bacterial velocity $\mathbf{U}_0 = U\langle \mathbf{p} \rangle$ parallel to the chemoattractant gradient. Typically, the magnitude of chemotactic drift velocity $U_0 = |\mathbf{U}_0|$ is about 10% of the swimming speed (Vuppula *et al.*, 2010), so that the theory with weak chemotaxis ($\zeta \ll 1$) will be reasonably accurate. On time and length scales larger than τ_0 and $U\tau_0$, the number density satisfies a conservation equation with a chemotactic convective flux and a diffusive flux with the diffusivity $D = U^2\tau_0/3$ arising from the unbiased part of the run-and-tumble motion (Keller & Segel, 1971; Bearon, 2003):

$$\frac{\partial n}{\partial t} + \nabla \cdot \left[(\mathbf{U}_0 + \mathbf{u})\, n - D\nabla n \right] = 0. \tag{3.3}$$

The fluid velocity $\mathbf{u}(\mathbf{x}, t)$ and pressure $p(\mathbf{x}, t)$ fields satisfy Stokes equations (Koch & Subramanian, 2011; Simha & Ramaswamy, 2002; Saintillan & Shelley, 2008*a*,*b*; Subramanian & Koch, 2009)

$$\nabla \cdot \mathbf{u} = 0, \tag{3.4}$$

$$-\nabla p + \mu \nabla^2 \mathbf{u} + \nabla \cdot \sigma^B = 0, \tag{3.5}$$

where the bacterial stress is given by $\sigma^B = -C\mu U L^2 \int \Omega \left[\mathbf{pp} - \frac{1}{3}\mathbf{I} \right] d\mathbf{p}$. Here μ is the viscosity of the suspending fluid, L is the combined length of the bacterial cell and propulsive flagellar bundle, and C is the force-dipole a bacterium exerts non-dimensionalized by $\mu U L^2$. C is positive for swimmers whose propulsive mechanisms push the cells and negative for pullers. The common bacterial species *E. Coli* and *B. Subtilis* are pushers with $C = 0.57$ (Subramanian & Koch, 2009). The anisotropic orientation distribution in Eq. 3.2 leads to an anisotropic bacterial stress tensor $\sigma^B(\mathbf{x}, t) = n(\mathbf{x}, t)\mathbf{S}$ where the stresslet $\mathbf{S} = -(C/16)\mu U L^2 \zeta \left[\mathbf{gg} - \frac{1}{3}\mathbf{I} \right]$. Being a pusher, the bacterium exerts a pressure in the z direction (negative normal stress) and tension (positive normal stress) in the x and y directions. Although the orientation field in Eq. 3.2 changes after the

onset of the instability due to rotation of bacteria by fluid velocity gradients, one can model the effects of this change on the bacterial stress in terms of a modified viscosity for disturbances with wavelengths larger than $(nL^2)^{-1}$ (Subramanian & Koch, 2009; Subramanian *et al.*, 2011). This viscosity is nearly isotropic when $\zeta \ll 1$ (Subramanian *et al.*, 2011). Since the effects of such a modified viscosity on the stability of the suspension have been analyzed previously, we focus instead on the active normal stress difference induced directly by the chemical gradient. In addition, we neglect the $O(\zeta^2)$ change in $\mathbf{U}_0$ due to shear induced cell rotation.

Eqs. 3.3, 3.4, and 3.5 admit a stationary base state solution with no fluid flow and an exponential number density profile $n_0(z) = \frac{\langle n_0 \rangle Pe \exp(-Pe\, z/H)}{1-\exp(-Pe)}$ determined by the balance of cross-channel chemotaxis and diffusion. Here the angle brackets indicate an average over the channel cross-section and $Pe = U_0 H/D = 3(\frac{H}{U\tau_0})(U_0/U)$ is a Peclet number measuring the strength of the chemotactic drift. In the base state, the inhomogeneous bacterial stress is balanced by the base state pressure $p_0 = S_{zz} n_0$.

We will now study the stability of this stationary base state to small perturbations of the bacteria number density and pressure fields, i.e., $n = n_0(z) + n'(x,z,t)$ and $p = p_0(z) + p'(x,z,t)$ with $n' \ll n_0$ and $p' \ll p_0$ and fluid velocity perturbations $\mathbf{u}'(x,z,t)$. We adopt a lubrication approximation in which the variations with respect to x occur over a wavelength λ which is much larger than the channel thickness H, i.e., $\epsilon = H/\lambda \ll 1$. Non-dimensionalizing z with the channel thickness H, x with wavelength λ, n with the gap averaged number density $\langle n_0 \rangle$, p with the bacterial stress $-\frac{3}{2} S_{zz} \langle n_0 \rangle$, u_x with $U_0 \epsilon$ and u_z with $U_0 \epsilon^2$ yields the following linearized lubrication equations. The x-momentum equa-

tion involves a balance between the viscous stress, the pressure gradient and the gradient of the bacterial stress:

$$-\beta\frac{\partial p'}{\partial x}+\frac{\beta}{3}\frac{\partial n'}{\partial x}+\frac{\partial^2 u'_x}{\partial z^2}=0, \tag{3.6}$$

where $\beta=-\frac{3S_{zz}\langle n_0\rangle H}{2\mu U_0}=\frac{3}{8}C\langle n_0\rangle L^2 H$ is a non-dimensional gap-averaged bacterial concentration that reflects the relative strength of the bacterial and viscous stresses.

The z momentum equation is a balance of the pressure gradient and bacterial stress gradient

$$\frac{\partial p'}{\partial z}+\frac{2}{3}\frac{\partial n'}{\partial z}=0, \tag{3.7}$$

which integrates to $p'(x,z,t)=-\frac{2}{3}n'(x,z,t)+\bar{p}(x,t)$ where $\bar{p}(x,t)$ is a z independent pressure field that assures that there is no net fluid flux in the x direction. The bacteria number density equation is:

$$\frac{\partial^2 n'}{\partial z^2}+Pe\frac{\partial n'}{\partial z}+\epsilon^2\left[\frac{\partial^2 n'}{\partial x^2}-\frac{\partial n'}{\partial t}-Peu'_z\frac{\partial n_0}{\partial z}\right]=0. \tag{3.8}$$

In the above equations, time has been non-dimensionalized by $\epsilon^{-2}H^2/D$ so that the unsteady term $\frac{\partial n'}{\partial t}$ balances the fluid convective term. It will be seen that this coupling term is the origin of the instability. The dominant balance in the bacteria conservation equation between chemotaxis and diffusion in the z direction yields a quasi-steady, local perturbed number density profile that is similar to the base state profile

$$n'(x,z,t)=\langle n'\rangle(x,t)\frac{Pe\exp(-Pez)}{1-\exp(-Pe)}, \tag{3.9}$$

The gap-averaged number density $\langle n'\rangle(x,t)$ will be determined from the $O(\epsilon^2)$ gap-averaged bacteria conservation equation. The solution of the x momentum equation with no slip boundary conditions is

$$u'_x=\beta\left\{\left[\frac{1-\exp(-Pez)}{Pe[1-\exp(-Pe)]}-\frac{z}{Pe}\right]\frac{\partial\langle n'\rangle}{\partial x}+\frac{1}{2}\frac{\partial\bar{p}}{\partial x}(z^2-z)\right\}, \tag{3.10}$$

where the pressure gradient determined by the constraint of no net fluid flux ($\langle u_x' \rangle = 0$) is

$$\frac{\partial \bar{p}}{\partial x} = 6\frac{Pe[1+\exp(-Pe)] + 2[\exp(-Pe)-1]}{Pe^2[1-\exp(-Pe)]}\frac{\partial \langle n' \rangle}{\partial x}. \tag{3.11}$$

Integrating Eq. 3.8 over $z = (0, 1)$ and using the no-flux and no-slip boundary conditions yields the gap averaged bacteria concentration equation:

$$\frac{\partial \langle n' \rangle}{\partial t} + Pe\frac{\partial \langle u_x' n_0 \rangle}{\partial x} - \frac{\partial^2 \langle n' \rangle}{\partial x^2} = 0, \tag{3.12}$$

which shows that the gap-averaged concentration perturbation evolves due to the fluid convective and run-and-tumble diffusive fluxes in the x direction. The convective flux will be proportional to $\frac{\partial \langle n' \rangle}{\partial x}$ with a sign dependent on whether the swimmers are pushers or pullers. Using the fluid velocity field in Eq. 3.10 driven by bacterial stresses to evaluate the convective flux, Eq. 3.12 takes the form:

$$\frac{\partial \langle n' \rangle}{\partial t} + (Pe\alpha\beta - 1)\frac{\partial^2 \langle n' \rangle}{\partial x^2} = 0, \tag{3.13}$$

where α is a function of Peclet number given by

$$\begin{aligned} \alpha &= \frac{1}{2Pe} + \left\{\frac{\exp(-Pe)(1+Pe)-1}{Pe^2[1-\exp(-Pe)]}\right\} \\ &\quad -3\left\{\frac{Pe[1+\exp(-Pe)] + 2[\exp(-Pe)-1]}{Pe^2[1-\exp(-Pe)]}\right\}^2 \end{aligned} \tag{3.14}$$

Sinusoidal gap-averaged number density perturbations evolve according to $\langle n' \rangle = \exp(i2\pi x + \sigma t)$ where the growth rate $\sigma = (2\pi)^2(Pe\alpha\beta - 1)$. Since both α and Pe are positive, instability occurs if β exceeds the critical value $\beta_{crit} = (\alpha Pe)^{-1}$. A suspension of pushers such as *E. Coli* or *B. Subtilis* for which β is positive, is unstable to number density variations in the x direction above a critical concentration while puller suspensions having negative β will be unconditionally stable. Fig. 3.2 shows that the critical bacteria concentration β_{crit}

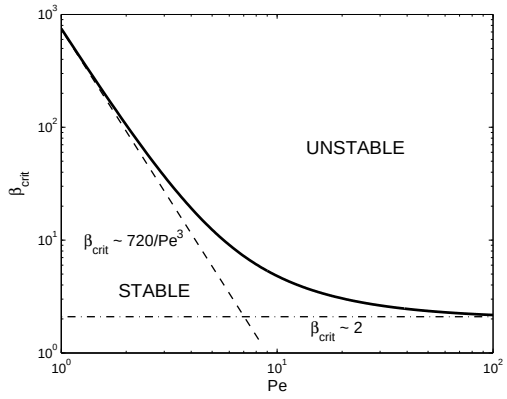

Figure 3.2: Critical bacteria concentration β_{crit} as a function of the Peclet number (solid line). The dashed lines are the asymptotic results: $\beta_{crit} \sim 720/Pe^3$ for $Pe \ll 1$ and $\beta_{crit} \sim 2$ for $Pe \gg 1$.

decreases with increasing Peclet number reaching an asymptote of 2 at high Peclet number.

The mechanism of the instability is illustrated in Fig. 3.1. The chemical gradient leads to a base state number density profile $n_0(z)$ that is an exponentially decreasing function of z and causes a net alignment of the cells in the $-z$ direction. The disturbance flow of each cell draws fluid in from the sides and pushes it out at the front and back. A sinusoidal perturbation in the gap-averaged number density, $\langle n' \rangle$, leads to a number density field, n' with alternate peaks and valleys (brighter and darker regions respectively in Fig. 3.1) at $z = 0$ owing to the competition of chemotaxis and diffusion in controlling the local z-number-density profile. Being pushers, the excess bacteria at peaks draw fluid inward at small z while the fluid returns toward valleys at larger values of z. This fluid velocity field acting on the base state number density field leads to a net gap-averaged convective flux $\langle u_x' n_0 \rangle$ toward the region of high $\langle n' \rangle$, thereby reinforcing the number density perturbation. In the sub-critical regime, x-diffusion of the bacteria attenuates the concentration perturbations and stabilizes the suspension.

Since the hydrodynamic disturbance of a puller is exactly opposite to that of a pusher, a suspension of pullers is always stable. Since σ is purely real, the instability is stationary at least in the long-wavelength limit and the streamline pattern resembles convection cells. A result of the lubrication approximation is that the dimensional growth rate increases quadratically in the wavenumber $2\pi/\lambda$. However, at sufficiently large wavenumbers one expects diffusion to stabilize the suspension implying that a mode of maximum growth rate should exist. The wavelength of the most unstable mode can come only from a finite wavelength analysis with $\lambda \sim H$ or smaller. This instability might be expected to lead to the formation of periodic clusters of bacteria within the channel or film along x axis with a length scale corresponding to the most unstable mode.

Sokolov *et al.* (2009) observed three-dimensional convective motions in films of aerobic bacteria with half-thickness greater than 100 μm. We refer to the half-film thickness here since the gradient of the attractant oxygen acts from the mid-plane to the interface when the film is thick enough so that the bacteria consume oxygen before it diffuses to the mid-plane. Although this experiment involve a thin film with gas-liquid interfaces, Marangoni stresses usually lead to a nearly inextensible nature of such interfaces making the no slip boundary condition appropriate. The bacterial concentration in Sokolov *et al.* (2009)'s experiments is $\langle n_0 \rangle \approx 2 \times 10^{10}$ per milliliter. Using $L = 12\mu m$ and $H = 100\mu$m, the scaled bacteria concentration is $\beta = 60$. It is clear from Fig. 3.2 that this value exceeds β_{crit} if $Pe \geq 2.50$. This corresponds to $U_0/U \geq 0.17$ for a typical bacterial swimming speed of 20 $\mu m/s$ and a typical tumbling frequency of 1 s^{-1} (Berg, 2003). This value of U_0/U is sufficiently small to make the small ζ analysis accurate. The chemotactic velocity is not known in Sokolov *et al.* (2009) experiments. Nevertheless, the above analysis suggests a moderate amount of chemotaxis can

drive the instability. The mode of instability predicted here is consistent with Sokolov *et al.* (2009)'s observations of convection across the film half-thickness and plumes of bacteria concentration.

The present instability mechanism differs from previous for active-stress instabilities (Koch & Subramanian, 2011; Simha & Ramaswamy, 2002; Saintillan & Shelley, 2008*a*,*b*; Subramanian & Koch, 2009; Subramanian *et al.*, 2011). Since the active bacterial stress depends on both the number density and orientation distribution of the bacteria, instability can arise from the coupling between either the number density field or the orientation field and the fluid flow. Previous stability analyses have focused on coupling of fluid shearing motion and swimmer alignment in unbounded homogeneous suspensions of isotropic (Saintillan & Shelley, 2008*a*,*b*; Subramanian & Koch, 2009) or aligned swimmers with (Subramanian *et al.*, 2011) or without chemotaxis (Simha & Ramaswamy, 2002; Saintillan & Shelley, 2008*a*,*b*). In these cases it is found that the unstable modes do not involve bacteria number density variations at leading order in the long wavelength limit. A fluid velocity perturbation to an isotropic (or nearly isotropic) suspension tends to align the bacteria to the extensional axis of the fluid velocity field. The hydrodynamic disturbance of a pusher then enhances the original velocity perturbation resulting in an orientation-shearing instability. It is possible that this instability accounts for the two-dimensional motion with no apparent bacteria concentration variation observed by Sokolov *et al.* (2009) at small film thickness. The instability mechanism described in the present Letter relies on a base state with a stratified number density profile. Fluid motion can then lead to a three-dimensional number density profile and concomitant active stress profile that enhances the number density variation in the case of pushers. In Sokolov *et al.* (2009)'s experiments, such an instability is to be expected

when the film is thick enough to allow oxygen and cell gradients to develop across the film half-thickness. A more definitive experimental test of the theory proposed in this Letter could be obtained using an experimental cell (Cheng *et al.*, 2007) that allows the cells to experience a controlled linear gradient of a chemo-attractant that is not consumed by the cells.

This work is supported by NSF grant CBET-0730579.

Bibliography

BEARON, R. N. 2003 An extension of generalized taylor dispersion in unbounded homogeneous shear flows to run-and-tumble chemotactic bacteria. *Phys. Fluids* **15**, 1552–1563.

BERG, H. C. 2003 *E. coli in Motion*. Springer Verlag.

BROWN, D. A. & BERG, H. C. 1974 Temporal Stimulation of Chemotaxis in Escherichia coli. *Proc. Natl. Acad. Sci.* **71**, 1388–1392.

CHEN, K. C., FORD, R. M. & CUMMINGS, P. T. 2003 Cell balance equation for chemotactic bacteria with a biphasic tumbling frequency. *J. Math. Biol.* **47**, 518–546.

CHENG, S. Y., HEILMAN, S., WASSERMAN, M., ARCHER, S., SHULER, M. L. & WU, M. 2007 A hydrogel-based microfluidic device for the studies of directed cell migration. *Lab Chip* **7**, 763–769.

HILLESDON, A. J. & PEDLEY, T. J. 1996 Bioconvection in suspensions of oxytactic bacteria: linear theory. *J. Fluid Mech.* **324**, 223–259.

KELLER, E. F. & SEGEL, L. A. 1971 Model for chemotaxis. *J. Theor. Biol.* **30**, 225–234.

KIM, M. J. & BREUER, K. S. 2007 Controlled mixing in microfluidic systems using bacterial chemotaxis. *Anal. Chem.* **79**, 955–959.

KOCH, D. L. & SUBRAMANIAN, G. 2011 Collective hydrodynamics of swimming microorganisms: Living fluids. *Ann. Rev. Fluid Mech.* **43**, 637–659.

MESIBOV, R. & ADLER, J. 1972 Chemotaxis toward amino acids in escherichia coli. *J. Bacteriol.* **112**, 315–326.

PEDLEY, T. J. & KESSLER, J. O. 1992 Hydrodynamic phenomena in suspensions of swimming microorganisms. *Ann. Rev. Fluid Mech.* **24**, 313–358.

SAINTILLAN, D. & SHELLEY, M. J. 2008*a* Instabilities and pattern formation in active particle suspensions: Kinetic theory and continuum simulations. *Phys. Rev. Lett.* **100**, 178103.

SAINTILLAN, D. & SHELLEY, M. J. 2008*b* Instabilities, pattern formation, and mixing in active suspensions. *Phys. Fluids* **20**, 123304.

SIMHA, R. A. & RAMASWAMY, S. 2002 Hydrodynamic fluctuations and instabilities in ordered suspensions of self-propelled particles. *Phys. Rev. Lett.* **89**, 058101.

SOKOLOV, A., GOLDSTEIN, R. E., FELDCHTEIN, F. I. & ARANSON, I. S. 2009 Enhanced mixing and spatial instability in concentrated bacterial suspensions. *Phys. Rev. E* **80**, 031903.

SUBRAMANIAN, G. & KOCH, D. L. 2009 Critical bacterial concentration for the onset of collective swimming. *J. Fluid Mech.* **632**, 359–400.

SUBRAMANIAN, G., KOCH, D. L. & FITZGIBBON, S. R. 2011 The stability of a homogeneous suspension of chemotactic bacteria. *Phys. Fluids* **23**, 041901.

VUPPULA, R. R., TIRUMKUDULU, M. S. & V., VENKATESH K. 2010 Chemotaxis of escherichia coli to l -serine. *Phys. Biol.* **7**, 026007.

CHAPTER 4

INSTABILITY OF AN INHOMOGENEOUS BACTERIAL SUSPENSION SUBJECTED TO A CHEMO-ATTRACTANT GRADIENT

4.1 Abstract

The stability of a suspension of chemotactic bacteria confined in an infinitely long channel and subjected to a stationary, linear chemo-attractant gradient is investigated. While swimming, individual bacteria exert force dipoles on the fluid which at the continuum level lead to a stress depending upon the bacterial orientation and number density fields. The presence of the attractant gradient causes bacteria to tumble less frequently when swimming along the gradient leading to a mean orientation and a non-zero chemotactic drift velocity U_0 in that direction. At long length and time scales compared to those associated with the persistence of bacterial swimming, fluxes due to chemotaxis and the random run-tumble motion of bacteria balance to yield an exponentially varying number density profile across the channel in the base state. The associated bacterial stress field is also exponentially varying and is normal. This spatially non-uniform base state is unstable to fluctuations in the bacterial concentration field when the scaled bacterial concentration $\beta = (3C/8)\langle n_0 \rangle L^2 H$ exceeds a critical value determined by a Peclet number defined as $Pe = U_0 H/\kappa$. Here, C is a non-dimensional dipole strength which depends on the geometry of the bacterium, $\langle n_0 \rangle$ is the bacterial concentration averaged across the channel of depth H, L is the total length of the bacterium, and κ is the bacterial diffusivity. β_{crit} is a monotonously decreasing function of Pe with $\beta_{crit} \sim 720/Pe^3$ for $Pe \ll 1$ and $\beta_{crit} \sim 2$ for $Pe \gg 1$. The instability is the result of the coupling between

the active stress driven fluid flow and the bacterial concentration and manifests as rectangular convection patterns. When β first exceeds β_{crit}, the unstable wavelengths are large with $\lambda \gg H$ and the mode of instability is stationary. Although oscillatory modes appear when $\lambda \leq O(H)$ and $\beta > 247$ the most dangerous mode of instability is found to be always stationary with a wavelength $\lambda_m/H \sim Pe^{-1}$. To study the coupling between the previously analyzed orientation shear instability mechanism of bacterial suspensions and the new chemotaxis driven instability, a new set of continuum equations which consistently accounts for weak chemotaxis, rotation of bacteria by weak fluid shear, and weak non-continuum effects along with their coupled effects have been derived. The stability analysis of those equations showed that the orientation shear mechanism has only a negligible influence on the critical concentration for the present chemotaxis-induced-instability when the suspension depth is large and it is the latter that has the lowest critical concentration.

4.2 Introduction

Recent experimental, numerical and theoretical investigations indicate that the stresses that swimming bacteria exert on the fluid give rise to hydrodynamic instabilities and collective motion in sufficiently dense bacterial suspensions (Koch & Subramanian, 2011). In a chemically neutral environment individual bacteria perform an unbiased random walk comprised of intervals of persistent swimming lasting about a second punctuated by short intervals of "tumbling" after which they pick a new swimming direction. In the presence of a chemical gradient, bacteria bias their random walk by reducing the tumbling frequency when swimming up the chemical gradient and leaving it unaltered

when swimming down resulting in a net bacterial migration along the chemical gradient (Berg, 2003). Since the aforementioned process "chemotaxis" is often critical to the survival of bacteria, its effects on the stability of the suspension is a pertinent question. In a previous letter (Kasyap & Koch, 2012) we have shown through a long wavelength lubrication analysis that a bacterial suspension confined in a microchannel or a thin liquid film and subjected to a transverse chemo-attractant gradient is unstable to perturbations of bacterial concentration parallel to the channel or film if the bacterial concentration exceeds a critical value due to the coupling between the bacterial number density field and the active stress driven fluid flow. In this paper, we perform a more detailed stability analysis in which we consider finite wavelengths and cover a broad range of parameter space. The primary objective of this paper is to show the existence of a most dangerous mode for which the growth rate is maximum and a cut-off wavenumber above which disturbances do not grow. Along with the scaling for the most dangerous and cut-off wavenumbers we demonstrate the existence of an oscillatory instability for certain parameter values. In addition, we examine the effect of the rotation of bacteria due to disturbance fluid shear fields which was neglected in Kasyap & Koch (2012). Shear rotation leads to orientational instabilities in suspensions of swimming bacteria and self-propelled rods (Simha & Ramaswamy, 2002; Saintillan & Shelley, 2008*a*,*b*; Subramanian & Koch, 2009) and its inclusion in the present analysis allows us to explore both the number-density chemotaxis instability and the orientational instability .

Early studies of the instability of chemotactic bacteria were either reaction-diffusion studies of bacteria that excreted or consumed the chemo-attractant in which hydrodynamic effects were neglected (Budrene & Berg, 1991, 1995; Brenner *et al.*, 1998) or studies of gravitational instabilities due to suspension mass

density variations induced by chemotaxis (Pedley & Kessler, 1992; Hillesdon & Pedley, 1996; Jánosi *et al.*, 1998). The former instability which is predominantly observed in bacterial colonies on moist agar surfaces is a result of the coupling between the attractant and bacterial concentration fields. Consumption of the attractant by bacteria generates spatial attractant gradients and when bacteria chemotactically respond to these, dense, concentric rings of bacteria form and propagate outward. When bacteria excrete the attractant the rings are destabilized and break into spots (Budrene & Berg, 1991, 1995; Brenner *et al.*, 1998).

The most extensively studied instability mechanism in a three-dimensional fluid suspension of bacteria is "bio-convection" a gravitational instability due to the chemotaxis of cells against gravity (Pedley & Kessler, 1992; Hillesdon & Pedley, 1996; Jánosi *et al.*, 1998). When a suspension of aerotactic bacteria such as *B. Subtilis* is exposed to air, the consumption of oxygen by bacteria and the diffusion of the oxygen into the suspension results in an oxygen gradient which causes the cells to migrate upwards against gravity. Since bacteria are slightly heavier than the suspending fluid, the accumulation of bacteria near the air-water interface results in an unstable density stratification with the heavier fluid lying above the lighter fluid triggering the well-known Rayleigh-Taylor instability (Pedley & Kessler, 1992; Hillesdon & Pedley, 1996; Jánosi *et al.*, 1998). The instability leads to the formation of convection patterns comprised of descending plumes rich in bacteria. Bio-convection occurs not only in bacterial suspensions but also in suspensions of algae for which the preferential motion against gravity, called gyrotaxis, arises from an asymmetric body mass distribution rather than chemotaxis. In the latter case, a second mechanism of instability arises due to the re-orientation of swimming cells by gravitational and viscous torques (Pedley & Kessler, 1992).

While the typical suspension depth required for bio-convection is of the order of millimeters or centimeters (Jánosi *et al.*, 1998), macroscopic fluid motion has been observed even in the case of chemotactic bacterial suspensions confined in liquid films or microchannels for which gravitational effects are negligible (Kim & Breuer, 2007; Sokolov *et al.*, 2009). For example, Kim & Breuer (2007) observed a significant enhancement in the effective diffusivity of a fluorescent dye in a suspension of wild type *E. Coli* in the presence of a horizontal chemo-attractant or chemo-repellent gradient. An increase in the scalar mixing indicated the existence of macroscopic stirring of the suspension. Sokolov *et al.*(2009) studied the dynamics of thin films of aqueous suspensions of aerobic *B. Subtilis* cells and observed a transition from a spatially homogeneous, quasi-two dimensional, coherent motion in the plane of the film to a strongly convective, spatially inhomogeneous three dimensional motion across the film when the film thickness was raised above a critical value. The onset of this convective motion coincided with the development of cross-film gradients of oxygen and the bacterial concentration was strongly inhomogeneous across the film thickness due to chemotaxis towards oxygen. At the critical film thickness, the Rayleigh number was much lower than the value, derived by Hillesdon & Pedley (1996), for the onset of bio-convection. This leads to the question whether the bulk convective motions observed in Sokolov *et al.* (2009)'s experiment was driven by the active stresses that bacteria exert on the fluid as they swim. The analysis presented in Kasyap & Koch (2012) shows this is indeed the case.

The long range fluid velocity disturbance due to a swimming bacterium results from a force-dipole or stresslet owing to the absence of any net force or torque on it. The fluid disturbance created by this stresslet is extensile for a bacterium like *E. Coli*, since its flagella bundle pushes the cell-body from be-

hind. Such a swimmer is termed a "pusher"to distinguish it from a "puller" for which the propulsive mechanism is located ahead of its body in the direction of swimming producing contractile fluid disturbances (Hernandez-Ortiz *et al.*, 2005; Saintillan & Shelley, 2007; Underhill *et al.*, 2008; Lauga & Powers, 2009). The dipolar hydrodynamic disturbance decays slowly as $1/|\boldsymbol{x}|^2$, where $|\boldsymbol{x}|$ is the distance from the bacterium, and hence results in long ranged hydrodynamic interactions in the suspension, the details of which are dependent on the suspension microstructure (Simha & Ramaswamy, 2002; Saintillan & Shelley, 2008*a*,*b*; Subramanian & Koch, 2009; Hohenegger & Shelley, 2010). The latter is specified by the bacterial concentration and orientation fields. At the continuum level, the effect of force-dipoles is to provide a stress field as a function of the local orientation and concentration fields of bacteria (Simha & Ramaswamy, 2002; Saintillan & Shelley, 2008*a*,*b*; Subramanian & Koch, 2009; Hohenegger & Shelley, 2010). Even for isotropic suspensions without any chemical gradients, the active stress field should in principle be able to drive instabilities that involve a feedback between suspension microstructure and fluid flow. Experiments on bacterial suspensions (Mendelson *et al.*, 1999; Wu & Libchaber, 2000; Kim & Breuer, 2004; Dombrowski *et al.*, 2004; Sokolov *et al.*, 2007) and numerical studies on hydrodynamically interacting self-propelled particles (Hernandez-Ortiz *et al.*, 2005; Saintillan & Shelley, 2007; Underhill *et al.*, 2008) strongly suggests that the aforementioned hypothesis is true. As we shall see later, the presence of an attractant gradient modifies the suspension micro-structure in a non-trivial way to result in a new kind of active stress driven instability.

Insights on the nature of these instabilities can be obtained through the recently developed continuum theory of bacterial suspensions (Saintillan & Shelley, 2008*a*,*b*; Subramanian & Koch, 2009; Hohenegger & Shelley, 2010). The start-

ing point in the continuum theory is the representation of the micro-structure of the suspension in the dilute limit by means of a singlet probability density $\Omega(\boldsymbol{x}, \boldsymbol{p}, t)$ defined in such a way that $\Omega(\boldsymbol{x}, \boldsymbol{p}, t) d\boldsymbol{x} d\boldsymbol{p}$ is the probability to find a bacterium in the interval $d\boldsymbol{x}$ around $\boldsymbol{x}$ with an orientation in the interval $d\boldsymbol{p}$ around $\boldsymbol{p}$. The time evolution of $\Omega(\boldsymbol{x}, \boldsymbol{p}, t)$ is influenced by swimming, tumbling in the case of wild-type bacteria, fluid convection, and rotation by fluid velocity gradients. One then obtains a mean-field active stress resulting from the coarse-graining of the bacterial force-dipoles which is proportional to the second moment of the bacterial orientation. The divergence of this stress appears in the momentum conservation equation for the suspension. The coupling between the orientation field and the fluid flow results in the orientational instability of homogeneous, isotropic suspensions of swimming bacteria and self-propelled rods. A bacterium, being a slender body, responds to the long ranged disturbance shear flow from other distant bacteria by rotating into the extensional quadrant of the disturbance velocity field. Thus there is an increased probability of bacterial orientations near the extensional axis of the disturbance flow and being a pusher, the intrinsic force dipoles on bacteria enhance the original disturbance resulting in instability. A puller on the other hand mitigates the effect of the disturbance flow as it creates a contractile hydrodynamic disturbance. In the mean-field sense, the anisotropic bacterial orientation field developed as a result of the fluid shear causes a stress in the fluid which opposes the Newtonian stress. Instability occurs when this destabilizing bacterial stress exceeds the stabilizing Newtonian viscous stress which happens only if bacteria are pushers (Subramanian & Koch, 2009).

In the absence of any orientation decorrelation mechanism as in the case of smooth swimmers analyzed by Saintillan & Shelley (2008*a*,*b*), the thresh-

old concentration for the instability is zero and the mode with longest wavelength grows fastest. On the contrary, the presence of tumbling or rotational diffusion limits the destabilizing active stress accumulated and the bacterial concentration needs to be above a critical value in order for the accumulated active stress to exceed the viscous stress and drive the instability (Subramanian & Koch, 2009). In the case of wild type bacteria for which the primary mechanism for orientation relaxation is tumbling, the critical concentration neglecting the passive resistance of bacterium against deformation is given by $(nL^3)_{crit} = 5L/[C\mathcal{F}(r)U_s\tau_0]$ (Subramanian & Koch, 2009; Subramanian *et al.*, 2011). Here n is the bacterial number density, L is the total length of a bacterium including the cell-body and flagella, C is the dipole moment of the bacterium non-dimensionalized by $\mu U_s L^2$ where μ is the viscosity of the suspending fluid, U_s is the swimming speed, and $\mathcal{F}(r) = (r^2 - 1)\,/\,(r^2 + 1)$ where $r = L/d$ is the aspect ratio of the bacterium with a cell-body diameter d. For a typical run-tumble bacterium like *E. Coli* or *B. Subtilis* $C = 0.57$, $L = 12\mu m$, $d = 1\mu m$, $\mathcal{F}(r) \approx 1$, $U_s = 20\mu m/s$, $\tau_0 = 1s$ (Subramanian & Koch, 2009; Subramanian *et al.*, 2011) yielding $(nL^3)_{crit} \approx 5$.

Subramanian *et al.* (2011) for the first time considered the effect of chemotaxis on the aforementioned orientation shear instability mechanism in homogeneous bacterial suspensions. Owing to the biased tumbling in the presence of a chemo-attractant gradient, the base-state bacterial orientation field becomes anisotropic with a mean orientation parallel to the gradient (Subramanian *et al.*, 2011). Their linear stability analysis shows that chemotaxis reduces the critical concentration required for the instability due to two distinct effects; first, the reduction of the tumbling frequency of cells swimming in the direction the chemical gradient allows the destabilizing active stress to accumulate for longer time

intervals, and second, the mean alignment of the cells with the gradient makes it easier for shear rotation to bring bacteria into the extensional quadrant. Previous researchers (Simha & Ramaswamy, 2002; Saintillan & Shelley, 2008*a*,*b*) had considered the stability of a state of perfect alignment of suspensions of self-propelled rods but without considering a mechanism (such as chemotaxis) for the maintenance of this orientational order. It may also be noted that chemotaxis leads to a bias in the orientation distribution of the cells rather than the perfect initial alignment considered by Simha & Ramaswamy (2002); Saintillan & Shelley (2008*a*,*b*).

The above-mentioned studies are limited to the case of unbounded and homogeneous suspensions in which the long wavelength instability is purely due to the coupling between the bacterial orientation field and the fluid flow without a perturbation to the number density field. However, since the active stress is a function of both number density and orientation fields, one can conceive a situation where number density perturbations couple with fluid flow resulting in instability without needing to have orientational fluctuations. For this to happen at the linear order, the base-state number density needs to be inhomogeneous, a state which naturally emerges in the presence of a chemo-attractant gradient. The mean bacterial orientation parallel to the attractant gradient resulting from the biased tumbling of the bacteria gives rise to a net "chemotactic" velocity in the same direction driving a convective flux. There is also a diffusive bacterial flux due to the unbiased part of bacterial tumbling (Keller & Segel, 1971). If impermeable walls or interfaces are present normal to the chemical gradient as in the case of bacterial suspensions studied by Sokolov *et al.* (2009) the convective and diffusive fluxes balance and consequently, the equilibrium bacterial concentration and active stress profiles across the channel will

be exponential (Kasyap & Koch, 2012). Furthermore, the anisotropic bacterial orientation field makes the bacterial stress normal with a compressive normal stress in the cross-channel direction and a tensile normal stress in the longitudinal direction. Above a critical value of bacteria concentration, this normal stress difference sets up cellular flow patterns when a perturbation to the number density field occurs and the resulting flow transports bacteria in such a way as to reinforce the original perturbation. The critical concentration for instability depends upon the strength of chemotaxis, bacterial diffusivity, the channel depth, and the bacterial geometry (Kasyap & Koch, 2012).

In our previous long wavelength analysis (Kasyap & Koch, 2012), the growth rate of the instability was found to increase quadratically with the wavenumber. However, for large enough wavenumbers one expects diffusion to stabilize the suspension and a mode of maximum growth rate should exist. If one neglects nonlinear effects, the preferred length scale of the instability is likely to be set by the most dangerous mode and hence its wavelength is a quantity of practical relevance (Chandrasekhar, 1961). In addition, the information on the cut-off wavenumber above which disturbances do not grow is useful in numerical simulations. In the present paper we address these through numerical solutions based on spectral methods since the governing equations with exponentially varying base-state number density defy any simple analytical solution for finite wavenumbers. For the special case of deep channels, the governing equations will be solved by using matched asymptotic expansions. Motivated by the extensive literature on shear-orientation instabilities, we perform a detailed analysis of the effect of shear rotation of bacteria on the present instability mechanism. We find that shear rotation in general has a destabilizing effect and below a critical suspension depth, the critical concentration is determined by

the shear rotation instability mechanism. Above this critical depth the present mechanism of instability starts to influence the critical concentration and for large suspension depths the effect of shear rotation is negligible.

This paper is organized as follows. In §4.3 we pose the problem and derive the governing equations. In §4.4 we revisit the case of long wavelength perturbations in order to introduce the physical mechanism of instability. Next in §4.5, we present an asymptotic analysis of a thin layer of bacteria confined in a deep channel and then proceed to a semi-analytical calculation for the case of infinitely deep channels. A detailed numerical calculation using spectral methods for the case of finite wavenumbers is presented in §4.6 followed by the analysis of shear rotation in §4.7. We begin §4.7 by presenting a consistent derivation of governing equations that includes chemotaxis and shear rotation along with higher order corrections for visco-elasticity and non-continuum effects. We then perform a linear stability analysis of the leading order equations in the long wavelength limit to investigate the effect of shear rotation. Finally in §4.8 we discuss our results from the perspective of the present literature on the subject.

4.3 Formulation

We consider a quiescent bacterial suspension between two infinitely long, impermeable parallel walls at $z = 0$ and $z = H$ subjected to a steady, linear chemo-attractant gradient in the $-z$ direction. Let x be the coordinate along the channel. In order to provide a *minimal* physical mechanism for the instability, we neglect the consumption and production of the attractant by bacteria. In fact, it is not necessary for an attractant to be consumed in order to elicit a

chemotactic response. For instance, Me-Asp (α-methyl-DL-aspartate) is a well-known attractant that is non-metabolizable (Mesibov & Adler, 1972; Budrene & Berg, 1991). Production of the attractant on the other hand, is not a generic phenomenon as it often requires special situations such as the presence of environmental stresses (Budrene & Berg, 1991, 1995; Brenner *et al.*, 1998). We also assume that the gradient remains steady even after the onset of instability since typical attractant diffusivities are much larger than the bacterial diffusivity. A quantitative justification for this assumption is provided in Appendix 4.9. We further consider bacterial suspensions that are sufficiently dilute enough to be described by the singlet probability density $\Omega(\boldsymbol{x}, \boldsymbol{p}, t)$ satisfying the kinetic equation (Subramanian & Koch, 2009)

$$\frac{\partial \Omega}{\partial t} + \nabla \cdot [(U_s \boldsymbol{p} + \boldsymbol{u})\Omega] + \nabla_{\boldsymbol{p}} \cdot (\dot{\boldsymbol{p}}\Omega) + \left(\frac{\Omega}{\tau} - \frac{1}{4\pi} \int \frac{\Omega}{\tau} d\boldsymbol{p} \right) = 0. \tag{4.1}$$

$\Omega(\boldsymbol{x}, \boldsymbol{p}, t)$ can be written as the product

$$\Omega(\boldsymbol{x}, \boldsymbol{p}, t) = n(\boldsymbol{x}, t) f(\boldsymbol{x}, \boldsymbol{p}, t), \tag{4.2}$$

where $n(\boldsymbol{x}, t)$ is the number density of bacteria defined as

$$n(\boldsymbol{x}, t) = \int \Omega(\boldsymbol{x}, \boldsymbol{p}, t) d\boldsymbol{p}, \tag{4.3}$$

and $f(\boldsymbol{x}, \boldsymbol{p}, t)$ is the bacterial orientation field satisfying the normalization constraint

$$\int f(\boldsymbol{x}, \boldsymbol{p}, t) d\boldsymbol{p} = 1. \tag{4.4}$$

Here $\boldsymbol{u}(\boldsymbol{x}, t)$ is the fluid velocity field so that the second term in Eq. 4.1 represents the advection of the probability distribution due to bacteria's swimming and the fluid flow. The third term is the divergence of the orientational flux associated with the rotation of the bacteria at a rate $\dot{\boldsymbol{p}}$ due to fluid velocity gradients. $\dot{\boldsymbol{p}}$ is given by (Kim & Karrila, 1991)

$$\dot{\boldsymbol{p}} = \boldsymbol{\omega} \cdot \boldsymbol{p} + \mathcal{F}(r)(\boldsymbol{I} - \boldsymbol{pp}) \cdot (\boldsymbol{e} \cdot \boldsymbol{p}), \tag{4.5}$$

where $\boldsymbol{\omega} = (1/2)(\nabla \boldsymbol{u}^{\dagger} - \nabla \boldsymbol{u})$ and $\boldsymbol{e} = (1/2)(\nabla \boldsymbol{u}^{\dagger} + \nabla \boldsymbol{u})$. The final term on the right hand side of Eq. 4.1 represents the rate of change in $\Omega(\boldsymbol{x}, \boldsymbol{p}, t)$ due to the tumbling of bacteria with a frequency τ. This is equal to the difference between the rate at which bacteria tumble away from orientations near $\boldsymbol{p}$ and the rate at which bacteria tumble into orientations near $\boldsymbol{p}$. Since the statistics of the tumbling process is Poissonian, the former rate is simply equal to Ω/τ (Subramanian & Koch, 2009). Assuming that the time evolution of $\Omega(\boldsymbol{x}, \boldsymbol{p}, t)$ is Markovian, the latter rate is given by $\int K(\boldsymbol{p}|\boldsymbol{p}')\Omega(\boldsymbol{x}, \boldsymbol{p}', t)/\tau d\boldsymbol{p}'$ where $K(\boldsymbol{p}|\boldsymbol{p}')$ is the transition probability between the pre- and post-tumble orientations which is equal to $1/(4\pi)$ if the pre- and post-tumble orientations are uncorrelated (Subramanian & Koch, 2009).

In the absence of any fluid flow and at time and length scales larger than the persistence time and length scales, τ_0 and $U_s\tau_0$, of a bacterium's swimming, the dominant balance in Eq. 4.1 is between the rates of bacteria coming into the phase space and leaving the phase space (Subramanian *et al.*, 2011; Kasyap & Koch, 2012)

$$\frac{\Omega}{\tau} - \frac{1}{4\pi}\int \frac{\Omega}{\tau} d\boldsymbol{p} = 0, \tag{4.6}$$

which allows one to separate $\Omega(\boldsymbol{x}, \boldsymbol{p}, t)$ into a time-dependent number density field $n(\boldsymbol{x}, t)$ and a quasi-steady orientation field $f(\boldsymbol{p})$ as (Kasyap & Koch, 2012)

$$\Omega(\boldsymbol{x}, \boldsymbol{p}, t) = n(\boldsymbol{x}, t) f(\boldsymbol{p}), \tag{4.7}$$

where $f(\boldsymbol{p})$ is governed by the integral equation

$$\frac{f(\boldsymbol{p})}{\tau} = \frac{1}{4\pi}\int \frac{f(\boldsymbol{p})}{\tau} d\boldsymbol{p}. \tag{4.8}$$

The requirement for a long length and time scale treatment arises from the fact that chemotaxis manifests only after a bacterium has experienced many tumbles. In this limit the separation between the orientation and number density

fields is possible since the swimming term $U_s\boldsymbol{p}\cdot\nabla\Omega$ does not appear in the dominant balance in Eq. 4.1 and the only way in which the number density can be correlated with the orientation field in the absence of fluid flow is through bacteria's swimming.

In the presence of a stationary chemo-attractant gradient, the biphasically biased bacterial tumbling frequency τ^{-1} is given by (Rivero *et al.*, 1989; Chen *et al.*, 2003; Kasyap & Koch, 2012)

$$\tau^{-1} = \begin{cases} \tau_0^{-1}(1-\zeta\boldsymbol{p}\cdot\boldsymbol{g}), & \boldsymbol{p}\cdot\boldsymbol{g} > 0 \\ \tau_0^{-1}, & \boldsymbol{p}\cdot\boldsymbol{g} \leq 0 \end{cases} \tag{4.9}$$

where $\zeta = \chi U_s G$ and $\boldsymbol{g} = -\boldsymbol{e_z}$ is the unit vector parallel to the chemical gradient. Here χ characterizes the sensitivity of the bacterium to the attractant gradient and G is the strength of the chemical gradient. χ is a function of the number of receptors on the bacterial cell body to which the attractant molecules bind, the binding kinetics, and the gain of the bacterium's signaling system (Rivero *et al.*, 1989; Subramanian *et al.*, 2011). The above equation is the linearized version of the exponential chemotactic response (see Subramanian *et al.*, 2011) originally proposed by Rivero *et al.* (1989). Inserting Eq. 4.9 into Eq. 4.8 and solving for $f(\boldsymbol{p})$ yields (Kasyap & Koch, 2012)

$$f(\boldsymbol{p}) = \begin{cases} \frac{1}{4\pi}\left[1+(\boldsymbol{p}\cdot\boldsymbol{g}-1/4)\zeta\right]+O(\zeta^2), & \boldsymbol{p}\cdot\boldsymbol{g} > 0, \\ \frac{1}{4\pi}\left[1-\zeta/4\right]+O(\zeta^2), & \boldsymbol{p}\cdot\boldsymbol{g} \leq 0. \end{cases} \tag{4.10}$$

Since $0 < \zeta \ll 1$ the orientation field described in Eq. 4.10 is weakly anisotropic peaking at $\boldsymbol{g}$ and resulting in a non-trivial mean orientation $\langle\boldsymbol{p}\rangle_f$ parallel to the chemical gradient and a chemotactic drift velocity $\boldsymbol{U_0}$ in the same direction (Kasyap & Koch, 2012)

$$\langle\boldsymbol{p}\rangle_f = \frac{\zeta}{6}\boldsymbol{g}, \qquad \boldsymbol{U_0} = U_s\langle\boldsymbol{p}\rangle_f = -U_0\boldsymbol{e_z}, \tag{4.11}$$

where $U_0 = U_s\zeta/6$. Here the symbol $\langle\rangle_f$ denotes an average over orientation space weighted by the bacteria's orientation distribution. Experimental observations indicate that the chemotactic velocity is typically about 10% of the swimming speed (Vuppula *et al.*, 2010; Kalinin *et al.*, 2009) making the small ζ approximation reasonably accurate. The chemotactic velocity leads to a convective bacterial flux $\boldsymbol{U_0}n$ parallel to the chemical gradient. In addition to this, the unbiased part of the bacterial random walk contributes a diffusive flux $-\boldsymbol{\kappa}\cdot\nabla n$ so that the conservation equation for the bacterial number density takes the form of a convection-diffusion equation (Keller & Segel, 1971; Chen *et al.*, 2003; Bearon & Pedley, 2000; Kasyap & Koch, 2012)

$$\frac{\partial n}{\partial t} + \nabla\cdot[(\boldsymbol{U_0}+\boldsymbol{u})n - \boldsymbol{\kappa}\cdot\nabla n] = 0. \tag{4.12}$$

Here the diffusivity tensor $\boldsymbol{\kappa} = \kappa_\parallel \boldsymbol{gg} + \kappa_\perp[\boldsymbol{I}-\boldsymbol{gg}]$ where $\kappa_\parallel$ and $\kappa_\perp$ are in general functions of ζ. However, for $\zeta \ll 1$, it can be shown that the leading order diffusion coefficient reduces to a scalar given by $\kappa = U_s^2\tau_0/3$ (Chen *et al.*, 2003; Bearon & Pedley, 2000; Bearon, 2003).

In the continuum theory of bacterial suspensions (Simha & Ramaswamy, 2002; Saintillan & Shelley, 2008*a*,*b*; Subramanian & Koch, 2009), the fluid velocity $\boldsymbol{u}(\boldsymbol{x},t)$ and pressure $p(\boldsymbol{x},t)$ satisfy Stokes' equations with an additional bacterial stress field $\boldsymbol{\sigma}^B$:

$$\nabla\cdot\boldsymbol{u} = 0, \tag{4.13a}$$

$$-\nabla p + \mu\nabla^2\boldsymbol{u} + \nabla\cdot\boldsymbol{\sigma}^B = 0. \tag{4.13b}$$

Note that one can define a macroscopic Reynolds number based on the channel depth and chemotactic velocity $Re = U_0H/\nu$ in addition to the microscopic Reynolds number based on the bacterial length and swimming speed. Since the former describes the unstable fluid flows generated by the chemotaxis of

bacteria U_0 is the appropriate velocity scale. For typical values $U_0 = 2\mu m/s$, $\nu = 0.01cm^2/s$, $Re \ll 1$ justifying the use of Stokes' equations when H is smaller than 1 cm. For the case of semi-infinite suspensions considered in §4.5, the characteristic length scale is the transport length κ/U_0 instead of H. For a bacterium swimming at a typical speed of 20 μm/s and tumbling at a rate of 1 /s, the diffusivity $\kappa = 133\mu m/s^2$ and the transport length scale based on the typical $U_0 = 2\mu m/s$ is of the order of 60 μm yielding a Reynolds number which is again much smaller than unity.

The deviatoric bacterial stress $\boldsymbol{\sigma}^B$ in Eq. 4.13 is given by (Subramanian & Koch, 2009):

$$\boldsymbol{\sigma}^B(\boldsymbol{x}, \boldsymbol{p}, t) = -C\mu U_s L^2 \int \Omega \left(\boldsymbol{pp} - \frac{\boldsymbol{I}}{3} \right) d\boldsymbol{p}, \tag{4.14}$$

Using Eqs. 4.7 and 4.10, one gets

$$\boldsymbol{\sigma}^B(\boldsymbol{x}, t) = n(\boldsymbol{x}, t)\boldsymbol{S}, \tag{4.15}$$

where the dipole moment $\boldsymbol{S}$ is given by (Kasyap & Koch, 2012)

$$\boldsymbol{S} = -\frac{C}{16}\mu U_s L^2 \zeta \left(\boldsymbol{gg} - \frac{\boldsymbol{I}}{3} \right). \tag{4.16}$$

Being a pusher, a bacterium exerts a pressure in the z direction (negative normal stress) and tension (positive normal stress) in the x and y directions corresponding to $S_{xx} = S_{yy} = -\frac{1}{2}S_{zz}$ (Kasyap & Koch, 2012).

The boundary condition for the number density equation Eq. 4.12 is the no-flux condition

$$\boldsymbol{U_0} n - \kappa \nabla n = 0 \quad \text{at } z = 0, H, \tag{4.17}$$

While it has been observed recently that the hydrodynamic and steric interactions between swimming bacteria and solid walls give rise to interesting phenomena such as swimming in circular trajectories (Lauga *et al.*, 2006), preferen-

tial swimming towards the right hand side (DiLuzio *et al.*, 2005), accumulation near walls (Berke *et al.*, 2008; Li & Tang, 2009), and motility reversal (Cisneros *et al.*, 2006), we expect these effects to be confined within a length scale of $U_s\tau_0$ from the wall so that the no-flux boundary condition Eq. 4.17 is appropriate for the long length scale treatment presented here.

For the fluid velocity field, we use the no-slip boundary condition

$$\boldsymbol{u} = 0 \quad \text{at } z = 0, H, \tag{4.18}$$

for most of our calculations. Bacteria often produce surfactants (see Angelini *et al.*, 2009) and in those situations the no-slip boundary condition Eq. 4.18 is applicable even for suspensions confined in liquid films since the Marangoni stress due to surfactants prevent dilatation of the interfaces making them effectively slip-free for two-dimensional fluid flows such as those arising in our stability analysis . We nevertheless briefly illustrate the effect of having a slip boundary on this instability in §4.5.

The governing equations Eqs. 4.12 and 4.13 together with the boundary conditions Eqs. 4.17 and 4.18 admit the stationary base-state solution (Kasyap & Koch, 2012)

$$n_0(z) = \frac{\langle n_0 \rangle \frac{U_0 H}{\kappa} \exp\left(\frac{-U_0 z}{\kappa}\right)}{1 - \exp\left(\frac{-U_0 H}{\kappa}\right)}, \tag{4.19}$$

and

$$p_0(z) = S_{zz} n_0(z). \tag{4.20}$$

where the subscript "0" indicates the base state and the angle brackets now indicate the average over the channel cross-section. $\langle n_0 \rangle$ serves as a normalization constant. Thus in the base state, the diffusive flux due to bacterial random walk and the chemotactic flux balance yielding an exponentially varying bacterial

number density profile across the channel and the resulting bacterial stress is balanced by the pressure.

We now study the stability of this base state against small perturbations by deriving the linearized equations

$$\frac{\partial n'}{\partial t} + \nabla \cdot (\boldsymbol{U_0} n' + \boldsymbol{u}' n_0 - \kappa \nabla n') = 0, \tag{4.21a}$$

$$-\nabla p' + \mu \nabla^2 \boldsymbol{u}' + \nabla \cdot (\boldsymbol{S} n') = 0, \tag{4.21b}$$

$$\nabla \cdot \boldsymbol{u}' = 0, \tag{4.21c}$$

in which the primed variables denote the perturbed quantities. Since the coefficients of primed quantities in Eq. 4.21 are independent of x, we seek normal mode solutions of the form

$$\big(n', u', w', p'\big) = \big[N(z), U(z), W(z), P(z)\big] exp(ikx + \sigma t), \tag{4.22}$$

where u' and w' are the perturbations in the fluid velocity in the x and z directions respectively. In Eq. 4.22 the wave number $k = 2\pi/\lambda$, where λ is the wavelength, is assumed to be real and the growth rate σ is allowed to be complex. The base state is unstable if the real part of σ is positive.

In order to non-dimensionalize Eq. 4.21, we use the characteristic scales H for length, U_0 for velocity, $\langle n_0 \rangle$ for the bacterial number density, H^2/κ for time, and $-\frac{3}{2} S_{zz} \langle n_0 \rangle$ for the pressure to define the non-dimensional variables: $\tilde{z} = z/H$, $\tilde{k} = kH$, $\tilde{U} = U/U_0$, $\tilde{W} = W/U_0$, $\tilde{n_0} = n_0/\langle n_0 \rangle$, $\tilde{N} = N/\langle n_0 \rangle$, $\tilde{t} = t\kappa/H^2$, $\tilde{\sigma} = \sigma H^2/\kappa$, and $\tilde{P} = P/(-\frac{3}{2} S_{zz} \langle n_0 \rangle)$. Substituting Eq. 4.22 into Eq. 4.21, using the above scalings and dropping the tildes, we obtain the following equations for the z dependent perturbation amplitudes

$$\left[D^2 + PeD - (\sigma + k^2)\right] N = PeWDn_0 \tag{4.23a}$$

$$ikU + DW = 0 \tag{4.23b}$$

$$\left(D^2 - k^2\right) U = ik\beta \left(P - \frac{1}{3}N\right) \tag{4.23c}$$

$$\left(D^2 - k^2\right) W = \beta \left(DP + \frac{2}{3}DN\right) \tag{4.23d}$$

$$(Pe + D)N = U = W = 0 \quad \text{at } z = 0, 1, \tag{4.23e}$$

where D indicates differentiation with respect to z and $n_0(z) = Pe\exp(-Pez)/[1-\exp(-Pe)]$. The physics of the instability is governed by two non-dimensional parameters, the Peclet number defined as

$$Pe = \frac{U_0 H}{\kappa} = 3\frac{H}{U_s \tau_0}\frac{U_0}{U_s}, \tag{4.24}$$

and

$$\beta = -\frac{3S_{zz}\langle n_0\rangle H}{2\mu U_0} = \frac{3}{8}C\langle n_0\rangle L^2 H. \tag{4.25}$$

Pe measures the strength of the chemotactic migration relative to the random bacterial motion and β is the ratio of the bacterial stress to the viscous stress. Equation 4.25 indicates that the parameter β can also be viewed as a scaled bacterial concentration in the channel, a relation obtained by using Eqns. 4.16 and 4.11. β and Pe are related by

$$\beta = \frac{C}{8}Pe\langle n_0\rangle L^3 \left(\frac{U_s\tau_0}{L}\right)\left(\frac{U_s}{U_0}\right). \tag{4.26}$$

For a typical wild type bacteria like *E. Coli* $U_s\tau_0/L = O(1)$ and using $C = 0.57$ and the nominal value of U_0/U_s as 0.1, one obtains $\beta = O(Pe\langle n_0\rangle L^3)$. Eliminating $U(z)$ and $P(z)$ in favor of $W(z)$ from Eq. 4.23 yields the following equations governing the amplitudes

$$\left[D^2 + PeD - (\sigma + k^2)\right] N = PeWDn_0, \tag{4.27a}$$

$$\left(D^2 - k^2\right)^2 W = -\beta k^2 DN, \tag{4.27b}$$

$$(Pe + D)N = W = DW = 0 \quad \text{at } z = 0, z = 1. \tag{4.27c}$$

Equation 4.27 has a close resemblance to the governing equations for bio-convection in Childress *et al.* (1975) and Hill *et al.* (1989) without gyrotaxis terms except that the momentum equation Eq. 4.27b here does not contain the inertial term and it is the bacterial number density gradient on the right hand side of the equation that drives the fluid flow rather than the number density itself as in bio-convection. The latter is a consequence of the fact that fluid flow here is driven by active stresses rather than buoyancy. A caveat in deriving the amplitude equations Eqs. 4.27 is the neglect of the effects of the bacterial rotation imparted by fluid velocity gradients. Shear rotation of bacteria changes the orientation field in Eq. 4.10 and hence changes the bacterial stress tensor $\boldsymbol{\sigma}^B$ and the chemotactic drift velocity $\boldsymbol{U_0}$. We address these later in §4.7 by doing a rigorous long wavelength analysis including the shear rotation of bacteria. It is found that the effect of shear rotation is negligible in determining the critical bacterial concentration required for the instability if the suspension is deep enough.

4.4 Long wavelength analysis

In this section we review the long wavelength analysis with $\lambda \gg H$ presented in Kasyap & Koch (2012) to introduce the physical mechanism of the instability. In Kasyap & Koch (2012) we performed a classical lubrication theory by scaling the x-distance with the wavelength λ and the z-distance with the channel depth H which immediately led to the small parameter for lubrication analysis $\epsilon = H/\lambda$. Here we show that solving the full governing equations perturbatively in powers of the non-dimensional wavenumber k yields identical results since k

and ϵ are related by

$$k = 2\pi\epsilon \tag{4.28}$$

This derivation provides a connection between the work of Kasyap & Koch (2012) and the current finite wavelength analysis by exhibiting the long wavelength analysis in a notation consistent with the present study. Instead of using U_0 as the characteristic scale for all velocities, we scaled the x-velocity in Kasyap & Koch (2012) by $U_0\epsilon$ and the z-velocity by $U_0\epsilon^2$ so that bacterial stress terms were retained in the leading order lubrication equations. In order to understand the dominant balances in the problem, we begin with Eq. 4.23 rather than the final governing equations Eq. 4.27. Without loss of generality, one can assume that $N(z) \sim 1$ and $P(z) \sim 1$ in the leading order and since the second order derivative on the left hand side of Eq. 4.23c should balance the right hand side (Hill *et al.*, 1989), $U \sim k$ in the leading order. The continuity equation Eq. 4.23b now implies that $W \sim k^2$. The relationship between k and ϵ in Eq. 4.28 shows that $U \sim \epsilon$ and $W \sim \epsilon^2$ which are identical to the scalings used in Kasyap & Koch (2012). Since the instability is due to the coupling between number density and fluid velocity fields, we assume $\sigma \sim k^2$ in the leading order so that the fluid convection term $PeWDn_0$ in Eq. 4.23a balances the growth term σN. Thus, we expand the dependent variables as

$$N(z) = N_0(z) + O(k), \tag{4.29a}$$

$$P(z) = P_0(z) + O(k), \tag{4.29b}$$

$$U(z) = kU_1(z) + O(k^2), \tag{4.29c}$$

$$W(z) = k^2W_2(z) + O(k^3), \tag{4.29d}$$

$$\sigma = k^2\sigma_2 + O(k^3). \tag{4.29e}$$

We restrict our analysis to the leading order since it is sufficient to capture the qualitative features of the instability. At $O(1)$ in Eq. 4.23a, chemotaxis and diffusion in the z-direction determines the leading order number density perturbation (Kasyap & Koch, 2012)

$$(D^2 + PeD)N_0 = 0, \tag{4.30a}$$

$$(Pe + D)N_0 = 0 \quad \text{at } z = 0, 1, \tag{4.30b}$$

leading to

$$N_0(z) = \frac{Pe\exp(-Pez)}{1 - \exp(-Pe)}. \tag{4.31}$$

Here $N(z)$ satisfies the arbitrary normalization condition $\langle N(z)\rangle = 1$. In the x-momentum equation Eq. 4.23c, the gradient of the pressure and the divergences of the bacterial and viscous stresses are in balance (Kasyap & Koch, 2012)

$$D^2U_1 = i\beta\left(P_0 - \frac{1}{3}N_0\right), \tag{4.32a}$$

$$U_1(0) = U_1(1) = 0, \tag{4.32b}$$

while in the z-momentum equation Eq. 4.23d the balance is between the pressure gradient and the divergence of the bacterial stress

$$DP_0 + \frac{2}{3}DN_0 = 0. \tag{4.33}$$

From Eq. 4.33

$$P_0(z) = -\frac{2}{3}N_0(z) + C_1, \tag{4.34}$$

where C_1 is an integration constant. Using Eq. 4.34 in Eq. 4.32 and solving for $U_1(z)$ gives

$$U_1(z) = i\beta\left[-\frac{\exp(-Pez)}{Pe[1 - \exp(-Pe)]} + C_1\frac{z^2}{2} + C_2z + C_3\right], \tag{4.35}$$

where the constants C_1, C_2, and C_3 are to be determined from the boundary conditions Eq. 4.32b and the incompressibility constraint Eq. 4.23b. Equations

4.32b and 4.23b imply that there is no net fluid flux in the x-direction or $\langle U(z)\rangle = 0$. Determining the constants in Eq. 4.35 yields the x-velocity field

$$\begin{aligned} U_1(z) &= i\beta\Bigg\{\frac{1-\exp(-Pez)}{Pe[1-\exp(-Pe)]} - \frac{z}{Pe} \\ &+ 3\left[\frac{Pe[1+\exp(-Pe)]+2[\exp(-Pe)-1]}{Pe^2[1-\exp(-Pe)]}\right]\left(z^2-z\right)\Bigg\}. \end{aligned} \tag{4.36}$$

The growth rate can now be obtained from the following solvability condition (Childress *et al.*, 1975; Hill *et al.*, 1989; Kasyap & Koch, 2012) resulting from the averaging of the number density equation Eq. 4.23a across the gap and using the no-flux boundary conditions

$$(\sigma_2+1)\langle N_0\rangle = -iPe\langle U_1 n_0\rangle, \tag{4.37}$$

which gives $\sigma_2 = Pe\alpha\beta - 1$ and hence

$$\sigma = k^2(Pe\alpha\beta - 1) + O(k^3), \tag{4.38}$$

where

$$\begin{aligned} \alpha &= \frac{1}{2Pe} + \left\{\frac{\exp(-Pe)(1+Pe)-1}{Pe^2[1-\exp(-Pe)]}\right\} \\ &- 3\left\{\frac{Pe[1+\exp(-Pe)]+2[\exp(-Pe)-1]}{Pe^2[1-\exp(-Pe)]}\right\}^2. \end{aligned} \tag{4.39}$$

It may be noted that $\alpha > 0$ for all $Pe > 0$ and hence $\sigma > 0$ if β is positive and exceeds the critical value given by (Kasyap & Koch, 2012)

$$\beta_{crit} = \frac{1}{Pe\alpha}. \tag{4.40}$$

Fig. 4.1 shows the neutral curve which indicates that the critical bacteria concentration β_{crit} for instability decreases with Pe and asymptotes to $\beta_{crit} = 2$ for large values of Pe. $\beta_{crit} \sim 720/Pe^3$ is the asymptotic behavior when $Pe \ll 1$. It is clear from Eq. 4.37 that the source of the instability is the coupling term $\langle U_1 n_0\rangle$

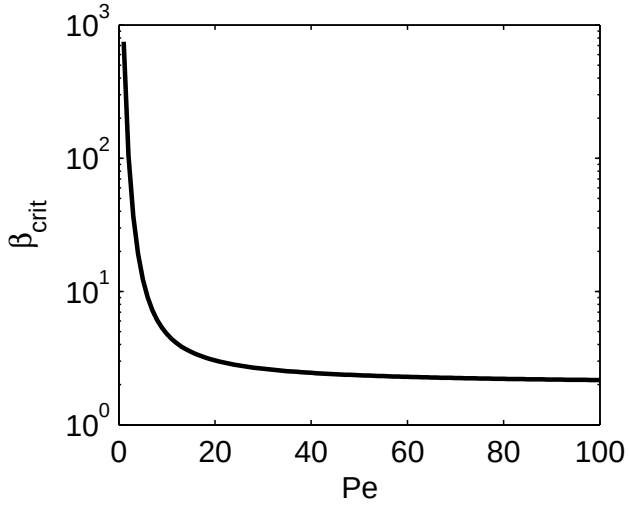

Figure 4.1: Neutral curve obtained from the long wavelength analysis. The suspension is unstable in the region that lies above the solid line. The asymptotes of β_{crit} are $\beta_{crit} \sim 720/Pe^3$ for $Pe \ll 1$ and $\beta_{crit} \sim 2$ for $Pe \gg 1$ (Kasyap & Koch, 2012).

which represents a net convective bacterial flux along the x-direction due to the action of the perturbed fluid velocity field on the base-state number density field. When this flux reinforces the original concentration perturbation, instability sets in. To understand how this net flux arises, consider Fig. 4.2 in which the color contours represent the perturbed number density field with brighter regions indicating a positive perturbation and darker regions indicating a negative perturbation from the mean number density. The associated spatially varying bacterial stress field drives a flow as shown by the streamlines. Since the hydrodynamic disturbance created by a bacterium draws fluid inward toward its sides and pushes fluid out at the front and the back, the disturbance fluid flow near the bottom wall is into the regions of higher number density. Fluid returns back to regions of lower number density near the top wall. Since the base-

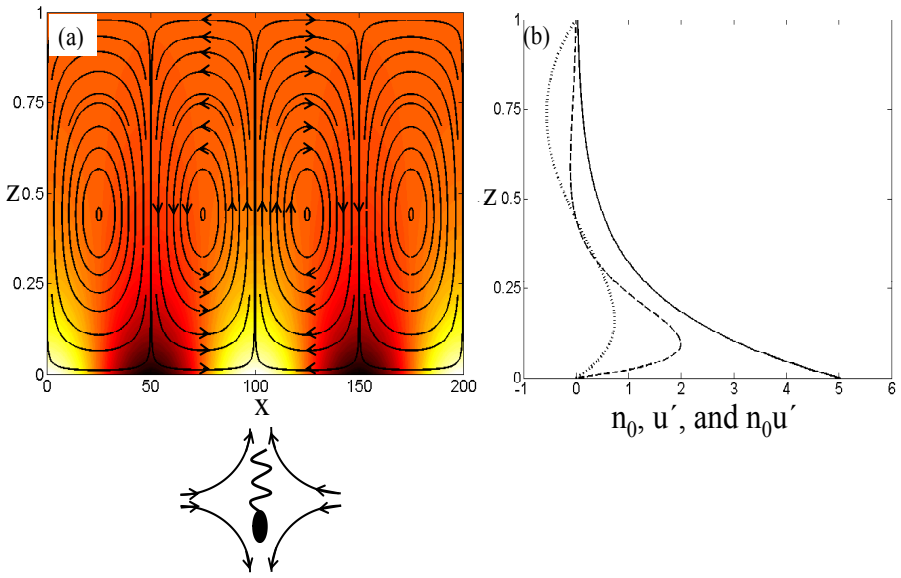

Figure 4.2: (a) Physical mechanism of the chemotaxis driven instability with the fluid disturbance created by a single bacterium aligned with the chemical gradient direction ($-z$ direction) shown at the bottom. This extensile fluid disturbance sets up convective motions in response to sinusoidal fluctuations in the bacteria concentration field. The latter is shown by the color contour with brighter regions indicating higher bacteria concentrations. The fluid motion acting on the base-state bacteria profile brings more bacteria toward the region of high perturbed bacteria concentration leading to growth of the perturbation (Kasyap & Koch, 2012). (b) Profiles of the base-state number density field n_0 (solid line), fluid velocity in the x direction u'/k (dots), and the flux $u'n_0$ at $x = 75$ (broken line)in (a) for $k = 0.02\pi$, $Pe = 5$, and $\beta = 25$. The exponentially decaying $n_0(z)$ results in a net flux $\langle u'n_0 \rangle$ towards the brighter region.

state number density is strongly peaked at the bottom wall, more bacteria are convected into brighter regions at small z than are convected back into darker regions at large z and there is a net bacterial flux towards brighter regions. This is made clear in Fig. 4.2(b) in which we show the profiles of the base-state number density field, the fluid velocity in the x direction and the convective bacterial flux along the x direction. When this convective flux exceeds the diffusive flux of bacteria from brighter regions to darker regions, the original concentration perturbation is enhanced resulting in instability. It is obvious that a suspension of pullers will be unconditionally stable against this mechanism of instability since the hydrodynamic disturbance field of a puller is exactly opposite to that of a pusher.

A result of the long wavelength analysis is that the growth rate increases quadratically with the wavenumber as seen in Eq. 4.38. In the original analysis of Kasyap & Koch (2012), this dependence of the growth rate on wavenumber has been scaled out by non-dimensionalizing time by $\epsilon^{-2}H^2/\kappa$. The long wavelength analysis fails to capture the most dangerous mode since the x diffusion of bacteria does not come into the leading order number density equation Eq. 4.30. In the following two sections we will relax the restriction to large wavelength perturbations. In doing so, analytical results can still be obtained in the limits $Pe \ll 1$ and $Pe \gg 1$, while a full numerical solution is required for $Pe = O(1)$. The asymptotic behavior of β_{crit} for $Pe \ll 1$ indicates the impossibility of instability with realistic bacterial concentrations in that regime and so we do not pursue the analysis for a shallow channel. Instead, we proceed to the analysis for deep channels for which $Pe \gg 1$.

4.5 Theory for deep channels

When the depth of the channel is large $Pe \gg 1$, the exponential form of the base-state number density $n_0(z)$ implies that bacteria occupy only an $O(1/Pe)$ layer near the bottom boundary $z = 0$ of the channel. Equations 4.27 are however valid since the boundary layer thickness $\delta = \kappa/U_0 = U_s^2\tau_0/(3U_0) \gg U_s\tau_0$ for $\zeta \ll 1$. We solve this problem by means of matched asymptotic expansions in which the dependent variables are expanded as a power series in $1/Pe$ for both the boundary layer (inner) and outer regions. Subsequent matching of solutions in these two regions determines the growth rate and eigen modes (Childress *et al.*, 1975; Hill *et al.*, 1989). We first perform the analysis for the case with the no-slip condition on both boundaries and then proceed to the case with the $z = 0$ boundary being a shear-free interface and $z = 1$ is a no-slip boundary. We choose to analyze the latter case since the $z = 0$ boundary condition has the strongest effect in this $Pe \gg 1$ regime due to the fluid flow being driven by the bacterial crowd in the boundary layer. We also provide a discussion of the results at the end of this section. In the present section "case I" refers to the problem with no-slip boundaries and "case II" to the problem with a slip boundary at $z = 0$ and a no-slip boundary at $z = 1$.

4.5.1 Analysis of case I

We start with the outer region for which the amplitude equations are

$$\left[Pe^{-1}\left(D^2 - \sigma - k^2\right) + D\right]\widehat{N} = 0, \tag{4.41a}$$

$$\left(D^2 - k^2\right)^2 \widehat{W} = -\beta k^2 D\widehat{N}, \tag{4.41b}$$

$$(1 + Pe^{-1}D)\widehat{N} = \widehat{W} = D\widehat{W} = 0 \quad \text{at } z = 1. \tag{4.41c}$$

We expand the dependent variables as

$$\widehat{N}(z) = \sum_{j=0}^{\infty} Pe^{-j}\widehat{N}_j(z), \tag{4.42a}$$

$$\widehat{W}(z) = \sum_{j=0}^{\infty} Pe^{-j}\widehat{W}_j(z). \tag{4.42b}$$

Substituting Eq. 4.42 in Eq. 4.41 one finds that

$$\widehat{N}(z) = 0, \tag{4.43}$$

for all powers of $1/Pe$ and the governing equation for $\widehat{W}(z)$ becomes

$$\left(D^2 - k^2\right)^2 \widehat{W}_j = 0, \tag{4.44a}$$

$$\widehat{W}_j = D\widehat{W}_j = 0 \quad \text{at } z = 1, \quad j = 0, 1, 2..... \tag{4.44b}$$

Solving Eq. 4.44 for each j and adding them up gives $\widehat{W}(z)$ as (Hill *et al.*, 1989)

$$\widehat{W}(z) = [A + B(z-1)]\sinh[k(z-1)] - kA(z-1)\cosh[k(z-1)], \tag{4.45}$$

with

$$A = \sum_{j=0}^{\infty} Pe^{-j}A_j \quad \text{and } B = \sum_{j=0}^{\infty} Pe^{-j}B_j.$$

The coefficients A_j's and B_j's are to be obtained by matching the outer solution with the inner solution. Since the characteristic vertical length scale in the inner region is the boundary layer thickness $\delta = O(1/Pe)$, the inner co-ordinate variable $\bar{z}$ is obtained by stretching the outer co-ordinate variable z by a factor of Pe.

$$\bar{z} = Pez. \tag{4.46}$$

Then the amplitude equations in the inner region take the form

$$\left[\overline{D}^2 + \overline{D} - Pe^{-2}(\sigma + k^2)\right]\overline{N} = -Pe\overline{W}\exp(-\bar{z}), \tag{4.47a}$$

$$\left[\overline{D}^2 - k^2 Pe^{-2}\right]^2 \overline{W} = -Pe^{-3}\beta k^2 \overline{DN}, \tag{4.47b}$$

$$(1+\overline{D})\overline{N} = \overline{W} = \overline{DW} = 0 \quad \text{at } \bar{z} = 0, \tag{4.47c}$$

where $\overline{D}$ is the differentiation with respect to $\bar{z}$. In order to solve these equations one needs to know the orders of magnitude of different variables. It is clear that $\overline{N} = O(1)$ suggesting the expansion

$$\overline{N}(\bar{z}) = \sum_{j=0}^{\infty} Pe^{-j}\overline{N}_j(\bar{z}), \tag{4.48}$$

which should satisfy the boundary and matching conditions

$$(1+\overline{D})\overline{N}(\bar{z}) = 0 \quad \text{at } \bar{z} = 0 \tag{4.49a}$$

$$\lim_{\bar{z}\to\infty} \overline{N}(\bar{z}) = 0, \tag{4.49b}$$

along with the arbitrary normalization condition

$$\int_0^{\infty} \overline{N}(\bar{z}) d\bar{z} = 1. \tag{4.50}$$

Finding a non-trivial analytical solution of Eq. 4.47 is possible only when the governing equation for the leading order number density $\overline{N}_0(\bar{z})$ is uncoupled from the momentum equation and the fluid flow $\overline{W}(\bar{z})$ driven by $\overline{N}_0(\bar{z})$ acts on the base-state number density $\overline{n}_0(\bar{z})$ to cause instability at a smaller order. In addition to this, the highest derivative on the left hand side of Eq. 4.47b should balance the right hand side in order for the velocity field to satisfy the boundary and matching conditions (Hill *et al.*, 1989)

$$\overline{W}(0) = 0, \tag{4.51a}$$

$$\lim_{\bar{z}\to\infty} \overline{W}(\bar{z}) = \lim_{z\to 0} \widehat{W}(z). \tag{4.51b}$$

From Eqs. 4.47a and 4.47b it is clear that the above requirements will be satisfied only when $k \ll O(Pe)$ and here we focus on the typical case of $k = O(1)$. We

also assume that $\beta = O(1)$ here since $\beta_{crit} \sim 2$ in the long wavelength limit with $Pe \gg 1$ as seen in Fig. 4.1. Equation 4.47b then suggests the expansion for $\overline{W}(\bar{z})$ as

$$\overline{W}(\bar{z}) = \sum_{j=0}^{\infty} Pe^{-(j+3)} \overline{W}_{j+3}(\bar{z}). \tag{4.52}$$

Finally, in order for the growth term $-Pe^{-2}\sigma\overline{N}$ in Eq. 4.47a to balance the coupling term $-Pe\overline{W}\exp(-\bar{z})$, the expansion for σ must take the form

$$\sigma = \sum_{j=0}^{\infty} Pe^{-j}\sigma_j. \tag{4.53}$$

Using the above expansions we find that the leading order number density $\overline{N}_0(\bar{z})$ is determined independently of the fluid velocity field due to the balance of chemotaxis and diffusion in the z direction:

$$(\overline{D}^2 + \overline{D})\overline{N}_0 = 0, \tag{4.54a}$$

$$(1 + \overline{D})\overline{N}_0 = 0 \quad \text{at } \bar{z} = 0, \tag{4.54b}$$

$$\lim_{\bar{z}\to\infty} \overline{N}_0(\bar{z}) = 0, \tag{4.54c}$$

whose solution satisfying the normalization $\int_0^\infty \overline{N}_0(\bar{z})d\bar{z} = 1$ is

$$\overline{N}_0(\bar{z}) = \exp(-\bar{z}). \tag{4.55}$$

At $O(Pe^{-1})$ in Eq. 4.47a we have,

$$(\overline{D}^2 + \overline{D})\overline{N}_1 = 0, \tag{4.56a}$$

$$(1 + \overline{D})\overline{N}_1 = 0 \quad \text{at } \bar{z} = 0, \tag{4.56b}$$

$$\lim_{\bar{z}\to\infty} \overline{N}_1(\bar{z}) = 0. \tag{4.56c}$$

The normalization condition at this order is $\int_0^\infty \overline{N}_1(\bar{z})d\bar{z} = 0$ so that the solution of Eq. 4.56 is the trivial solution $\overline{N}_1 = 0$. At $O(Pe^{-3})$, the leading order number density drives the fluid flow as

$$\overline{D}^4\overline{W}_3 = -\beta k^2 \overline{DN}_0, \tag{4.57a}$$

$$\overline{W}_3 = \overline{DW}_3 = 0 \quad \text{at } \bar{z} = 0. \tag{4.57b}$$

Solving Eq. 4.57 and matching with the outer solution Eq. 4.45 (see Appendix 4.10.1) gives

$$\overline{W}_3(\bar{z}) = \beta k^2 \left[\bar{z} + \exp(-\bar{z}) - 1\right] \tag{4.58}$$

One can now obtain the leading growth rate σ_0 using the solvability condition

$$(\sigma_0 + k^2) \int_0^\infty \overline{N}_0(\bar{z}) d\bar{z} = \int_0^\infty \overline{W}_3(\bar{z}) \exp(-\bar{z}) d\bar{z}, \tag{4.59}$$

which yields

$$\sigma_0 = k^2 \left(\frac{\beta}{2} - 1\right). \tag{4.60}$$

In order to obtain the first correction to σ_0 we consider the solvability condition obtained by integrating the $O(Pe^{-3})$ number density equation from Eq. 4.47a and applying the boundary and matching conditions

$$\sigma_1 \int_0^\infty \overline{N}_0(\bar{z}) d\bar{z} = \int_0^\infty \overline{W}_4(\bar{z}) \exp(-\bar{z}) d\bar{z}, \tag{4.61}$$

where $\overline{W}_4(\bar{z})$ is governed by

$$\overline{D}^4 \overline{W}_4 = 0, \tag{4.62a}$$

$$\overline{W}_4 = \overline{DW}_4 = 0 \quad \text{at } \bar{z} = 0, \tag{4.62b}$$

whose solution that matches with the outer solution is

$$\overline{W}_4(\bar{z}) = -\beta k^3 \left(\frac{k - \sinh k \cosh k}{k^2 - \sinh^2 k}\right) \bar{z}^2. \tag{4.63}$$

Equation 4.63 when used in Eq. 4.61 gives

$$\sigma_1 = -2\beta k^3 \left(\frac{k - \sinh k \cosh k}{k^2 - \sinh^2 k}\right) \bar{z} \tag{4.64}$$

and combining Eqs. 4.60 and 4.64 yields

$$\sigma = k^2 \left(\frac{\beta}{2} - 1\right) - \frac{2\beta k^3}{Pe} \left(\frac{k - \sinh k \cosh k}{k^2 - \sinh^2 k}\right) + O(Pe^{-2}). \tag{4.65}$$

Since σ is purely real, the instability is stationary in the $Pe \gg 1$ limit. Solving Eq. 4.65 for $\sigma = 0$ gives a critical β

$$\beta_c = 2 + \frac{8k}{Pe}\left(\frac{k - \sinh k \cosh k}{k^2 - \sinh^2 k}\right) + O(Pe^{-2}). \tag{4.66}$$

which is different from the β_{crit} defined earlier in §4.4 since the neutral curve here is a function of the wavenumber also. One may now define β_{crit} as $\beta_{crit} = min(\beta_c)$ and from Eq. 4.66 $\beta_{crit} = 2$ since β_c has the minimum value at $k = 0$. Thus we have recovered the previous asymptotic result for $Pe \gg 1$ from the long wavelength analysis in §4.4. We shall also see in §4.6 that for any Pe, the minimum of β_c occurs at $k = 0$.

4.5.2 Analysis of case II

Since the outer boundary condition is the same here as in case I, the outer solutions for the number density and fluid velocity fields remain those given by Eqs. 4.43 and 4.45. The inner number density and velocity fields are still governed by Eq. 4.47 but the no-slip boundary condition $\overline{U} = 0$ changes to the no-shear stress condition $\overline{DU} = 0$ at $\bar{z} = 0$. Using the incompressibility condition in Eq. 4.23b on the latter, we get the boundary conditions on $\overline{W}$as

$$\overline{W} = \overline{D}^2\overline{W} = 0 \quad \text{at } \bar{z} = 0. \tag{4.67}$$

The expansion for the number density field is the same as in Eq. 4.48 and we assume that k and β are of order 1 here too. To proceed further we need to know the scaling for the velocity field in this case. Since the governing equations in the inner region are the same as in case I except for the boundary condition at $z = 0$, one might think that the same scaling $\overline{W} \sim Pe^{-3}$ would hold here too

(see Eq. 4.52). This scaling gives an $O(Pe^{-2})$ fluid velocity in the x direction which satisfies the no-slip boundary condition at $z = 0$ and *varies* across the boundary layer. The latter variation is due to the scaled incompressibility constraint $ik\overline{U} + Pe\overline{DW} = 0$ within the boundary layer. However, unlike case I, the shear-free boundary condition here permits a fluid velocity in the x direction that is *constant* across the boundary layer which cannot be accounted by the above scaling. One can have the latter if the velocity field is not forced by the number density field in Eq. 4.47b which requires $\overline{W} = O(Pe^{-2})$ and hence suggests the expansion

$$\overline{W}(\bar{z}) = \sum_{j=0}^{\infty} Pe^{-(j+2)}\overline{W}_{j+2}(\bar{z}). \tag{4.68}$$

Equation 4.47a then suggests the expansion for growth rate as

$$\sigma = \sum_{j=0}^{\infty} Pe^{-j+1}\sigma_{j-1}. \tag{4.69}$$

These expansions indicate that the leading number density field still remains the same as in Eq. 4.55 and that the leading fluid velocity field is not driven directly by the bacterial stress

$$\overline{D}^4\overline{W}_2 = 0, \tag{4.70a}$$

$$\overline{W}_2 = \overline{D}^2\overline{W}_2 = 0 \quad \text{at } \bar{z} = 0. \tag{4.70b}$$

As in case I bacterial stress drives the fluid flow at $O(Pe^{-3})$ so that $\overline{W}_3$ is determined by

$$\overline{D}^4\overline{W}_3 = -\beta k^2\overline{DN}_0, \tag{4.71a}$$

$$\overline{W}_3 = \overline{D}^2\overline{W}_3 = 0 \quad \text{at } \bar{z} = 0. \tag{4.71b}$$

The solutions to Eqs. 4.70 and 4.71 that satisfy the boundary and matching conditions are (see Appendix 4.10.2)

$$\overline{W}_2(\bar{z}) = \frac{\beta k}{2}\left(\frac{k^2 - \sinh^2 k}{k - \sinh k \cosh k}\right)\bar{z}, \tag{4.72a}$$

$$\overline{W}_3(\bar{z}) = \beta k^2\left[\exp(-\bar{z}) - \frac{\bar{z}^2}{2} - 1\right]. \tag{4.72b}$$

The leading growth rate obtained from the solvability condition

$$\sigma_{-1}\int_0^\infty \overline{N}_0 d\bar{z} = \int_0^\infty \overline{W}_2 d\bar{z} \tag{4.73}$$

is $\sigma_{-1} = (\beta/2)k(k^2 - \sinh^2 k)/(k - \sinh k \cosh k)$ and the next correction σ_0 still determined by Eq. 4.59 is $\sigma_0 = -k^2(1 + 3\beta/2)$ so that the expression for growth rate takes the form

$$\sigma = Pe\frac{\beta k(k^2 - \sinh^2 k)}{2(k - \sinh k \cosh k)} - k^2\left(1 + \frac{3\beta}{2}\right) + O(Pe^{-1}). \tag{4.74}$$

The critical β at finite wavenumber then obtained from Eq. 4.74 is

$$\beta_c = \frac{1}{Pe}\frac{2k(k - \sinh k \cosh k)}{\left(k^2 - \sinh^2 k\right)} + O(Pe^{-2}), \tag{4.75}$$

and β_c has the minimum value of $\beta_{crit} = 4/Pe$ at $k = 0$.

4.5.3 Discussion

While the quantitative analysis of the modes of instability is given most readily in terms of solutions for the bacteria number density and the z-fluid-velocity field, more physical insight into the differences between cases I and II is obtained by examining the x-fluid-velocity field. This may be obtained by applying the continuity equation, which is Eq. 4.23b in the outer region and its rescaled form $\overline{U} = -Pe/(ik)\overline{DW}$ in the boundary layer to on the solutions for

the z-fluid-velocity fields. Specifically, for case I we have the outer, inner, and uniformly valid solutions respectively written in terms of the outer coordinate as

$$\widehat{U}(z) = -\frac{1}{ikPe^2}\big\{A_2k^2(1-z)\sinh[k(z-1)] + B_2\big[\sinh[k(z-1)] + k(z-1)\cosh[k(z-1)]\big]\big\} + O(Pe^{-3}), \tag{4.76a}$$

$$\overline{U}(z) = -\frac{1}{ikPe^2}\left\{\beta k^2[1-\exp(-Pez)] - 2\beta k^3\left(\frac{k-\sinh k\cosh k}{k^2-\sinh^2 k}\right)z\right\} + O(Pe^{-3}), \tag{4.76b}$$

$$U(z) = -\frac{1}{ikPe^2}\big\{A_2k^2(1-z)\sinh[k(z-1)] + B_2\big[\sinh[k(z-1)] + k(z-1)\cosh[k(z-1)]\big] - \beta k^2\exp(-Pez)\big\} + O(Pe^{-3}), \tag{4.76c}$$

and for case II we have

$$\widehat{U}(z) = -\frac{1}{ikPe}\big\{A_1k^2(1-z)\sinh[k(z-1)] + B_1\big[\sinh[k(z-1)] + k(z-1)\cosh[k(z-1)]\big]\big\} + O(Pe^{-3}), \tag{4.77a}$$

$$\overline{U}(z) = -\frac{1}{ikPe}\left[\frac{\beta k}{2}\left(\frac{k^2-\sinh^2 k}{k-\sinh k\cosh k}\right) - \beta k^2 z - \beta k^2 Pe^{-1}\exp(-Pez)\right] + O(Pe^{-3}), \tag{4.77b}$$

$$U(z) = -\frac{1}{ikPe}\big\{A_1k^2(1-z)\sinh[k(z-1)] + B_1\big[\sinh[k(z-1)] + k(z-1)\cosh[k(z-1)]\big] - Pe^{-1}\beta k^2\exp(-Pez)\big\} + O(Pe^{-3}). \tag{4.77c}$$

The uniformly valid solutions are constructed by subtracting the solution in the overlap region from the sum of the boundary layer and outer solutions and are shown in Fig. 4.3. The primary observation here is that the velocity field satisfying no-slip boundary conditions in Eq. 4.76 is $O(Pe^{-2})$ while the velocity field satisfying no tangential stress in Eq. 4.77 is $O(Pe^{-1})$. The latter however needs an order Pe^{-2} correction that comes from the inner solution to satisfy the shear-free boundary condition at $z = 0$. There is no $O(Pe^{-2})$ correction in the

outer solution since $A_2 = B_2 = 0$ as demonstrated in Appendix 4.10.2.

The scaling for case I fluid velocity can be obtained from a dominant balance analysis of the momentum equation and the incompressibility constraint within the boundary layer. The latter results in a large x velocity compared to the z velocity when $k \sim O(1)$ owing to the wide separation between the characteristic length scales H and δ in the x and the z direction, respectively. As a result, the fluid velocity will be primarily determined by the balance between bacteria and viscous stress terms in the x momentum equation. Since the derivatives in the x direction are asymptotically smaller than the derivatives in z direction, the dominant balance in the x momentum equation is $\mu\overline{u}'/\delta^2 \sim S_{xx}\overline{n'}/H$. This yields the amplitude of the non-dimensional fluid velocity in the x direction as $\overline{U} \sim \beta Pe^{-2}$. The incompressibility constraint then gives the fluid velocity amplitude in the z direction as $\overline{W} \sim (\delta/H)\overline{U} \sim \beta Pe^{-3}$. While most of the bacterial stress in the boundary layer is utilized for overcoming the wall shear stress induced by the no-slip boundary condition in case I, the lack of any wall shear stress in case II leaves the entire bacterial stress available for driving the outer flow. As a result the magnitude of the fluid velocity field in case II, which is larger than case I by a factor of Pe, can be obtained by balancing the shear stress $\mu\overline{u'}/\delta$ in the x momentum equation with the bacteria stress $S_{xx}\overline{n'}$ which gives the scaling $\overline{U} \sim \beta Pe^{-1}$ and consequently $\overline{W} = \beta Pe^{-2}$ for case II. The associated β_{crit} from Eqs. 4.66 and 4.75 also differ by a factor of Pe with $\beta_{crit} = O(1)$ for case I and $\beta_{crit} = O(Pe^{-1})$ for case II.

The difference between magnitudes of the fluid velocity in case I and II can also be reasoned in terms of the images that the individual force dipoles of bacteria create when they are near a no-slip or shear-free boundary. It is well-known

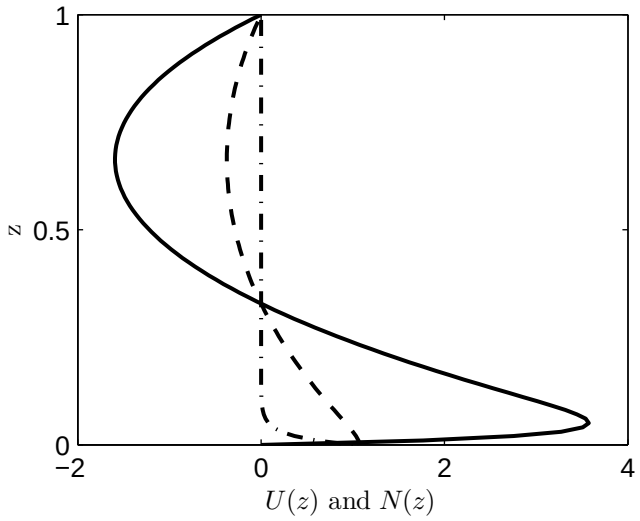

Figure 4.3: Profiles of the leading order fluid velocity in the x direction for case I (solid line) and case II (dashed line) along with the leading order number density perturbation (dash-dotted line) at $Pe = 50$, $\beta = 5$, and $k = 1$. In order to plot both case I and II on the same graph, we rescale velocities as $Pe^2U(z)$ for case I and $PeU(z)$ for case II.

that a Stokeslet with the point force normal to a no-slip boundary creates a velocity field with no net force dipole in the far-field but rather acts as a force-quadrupole (Blake, 1971). On the other hand, the image of a Stokeslet normal to a shear-free boundary is just another Stokeslet with an opposite force and hence the velocity field is that of a net force-dipole in the far-field (Aderogba & Blake, 1978). Since a force-dipole is composed of two forces equal in magnitude but opposite in direction, the far field velocity produced by a dipole near a no slip boundary has no net dipolar or quadrupolar component, while the far-field velocity due to a dipole near a shear-free boundary is a force-dipole velocity field with twice the magnitude of the original dipolar field. Thus the fluid disturbance created by a force-dipole near a shear-free boundary is much stronger than near a no-slip boundary. Furthermore, since case II permits a constant x ve-

locity throughout the boundary layer, the leading order outer solution near the boundary layer given by $\widehat{U}(0)$ is the same as the leading order boundary layer solution $\overline{U}(z) = -(ikPe)^{-1}\left[\frac{\beta k}{2}\left(\frac{k^2-\sinh^2 k}{k-\sinh k\cosh k}\right)\right]$ obtained by having $z = O(1/Pe)$ in Eq. 4.77b. In other words, the outer solution simply *continues* into the boundary layer and the next correction to the boundary layer velocity field given by the term $-Pe^{-2}\beta k^2\exp(-Pez)$ helps satisfy the condition of zero shear stress at $z = 0$. The latter is not true for case I as is evident from Eq. 4.76.

Now the magnitude of the x fluid velocity in the outer region for both cases I and II is set by the respective inner x velocities since there is no driving force for fluid flow in the outer region. Thus $\widehat{U} \sim \beta Pe^{-2}$ for case I and $\widehat{U} \sim \beta Pe^{-1}$ for case II respectively. One important observation in Fig. 4.3 is that the flow covers the entire channel for both cases even though it is driven by a thin layer of bacteria near $z = 0$. Thus the vertical length scale of fluid motion is of the same order as the horizontal length scale which in this case with $k = O(1)$ is the suspension depth. This is a simple consequence of the low Reynolds number nature of the fluid motion and the fact that the fluid velocity profile in the outer region is determined primarily by the constraint of incompressibility.

4.5.4 Analysis for a semi-infinite channel

Equation 4.65 exhibits a most dangerous mode when the $O(1/Pe)$ term in the asymptotic series is comparable to the leading term, a situation in which the series is no longer truly asymptotic. The reason behind the failure of the asymptotic analysis to capture the most dangerous mode is that the leading order number density equation Eq. 4.54 does not involve x diffusion, a situation similar to

the one in the long wavelength analysis presented in the last section. In order to have the growth and x diffusion in the leading order for the most dangerous mode, one needs $k = O(Pe)$ and $\sigma = O(Pe^2)$ in Eq. 4.47. This amounts to rescaling the dimensional wavenumber by the inverse boundary layer thickness U_0/κ and the growth rate by the inverse time scale U_0^2/κ. The former means that the most dangerous wavelength is comparable to the boundary layer thickness. Since it is difficult to obtain the exact analytical solution of the inner equations Eq. 4.47 in this limit that matches with the outer solution Eq. 4.45, we solve the problem approximately for the case of an infinitely deep channel in the positive half space. Apart from showing that a most dangerous mode exists, the solution obtained here is relevant to real cases that have finite channel depth since for $Pe \gg 1$ and for $k = O(Pe)$ the spatial extent of the flow in both horizontal and vertical directions will be of the order of the boundary layer thickness κ/U_0 rather than the channel depth so that the $z = 1$ boundary would not matter. Furthermore, the result from this analysis would serve as tool for the validation of the numerical solution presented in the next section.

Thus we solve the modified inner problem

$$\left[D^2 + D - (\sigma + k^2)\right] N = -W \exp(-z), \tag{4.78a}$$

$$\left[D^2 - k^2\right]^2 W = -\beta k^2 DN, \tag{4.78b}$$

$$(1 + D)N = W = DW = 0 \quad \text{at } z = 0, \tag{4.78c}$$

$$N = DN = W = DW \to 0 \quad \text{as } z \to \infty, \tag{4.78d}$$

obtained after dropping overbars in Eq. 4.47 and rescaling σ and k appropriately as mentioned before. Since the gap-averaged number density $\langle n_0 \rangle$ vanishes in the limit of infinite depth, one needs to rescale the number density by $n_a U_0/\kappa$

where n_a is the number of bacteria per unit area. The quantity β can then be redefined as $\beta = (3/8)Cn_aL^2$.

To solve Eq. 4.78 we use a series method similar to the one used by Childress *et al.* (1975) and expand the dependent variables as truncated series

$$N(z) = \sum_{j=0}^{M} \left\{ N_{1,j} \exp\left[-(m+j)z\right] + \Big(N_{2,j} + N_{3,j} z\Big) \exp\left[-(k+j)z\right] \right\}, \quad \text{(4.79a)}$$

$$W(z) = \sum_{j=0}^{M} \left\{ W_{1,j} \exp\left[-(m+j)z\right] + \Big(W_{2,j} + W_{3,j} z\Big) \exp\left[-(k+j)z\right] \right\}, \quad \text{(4.79b)}$$

with $m = \frac{1}{2}\left[1 + \sqrt{1 + 4(\sigma + k^2)}\right]$ so that the solutions in Eq. 4.79 and their derivatives decay as $z \to \infty$ as indicated in the boundary conditions Eq. 4.78c for $\sigma \geq 0$. It is also assumed that σ is purely real here. Here $N_{2,0} = N_{3,0} = 0$ and $N_{1,0} \exp(-mz)$ is the decaying homogeneous solution of the number density equation Eq. 4.78a with the arbitrary amplitude $N_{1,0}$ which, without loss of any generality, is taken as unity. The homogeneous solution of Eq. 4.78a then drives the $j = 0$ inhomogeneous solution for the fluid velocity in Eq. 4.78b which in turn drives the $j = 1$ inhomogeneous solution for the number density Eq. 4.78a and so on. Recursive expressions for the coefficients $N_{1,j}$'s and $W_{1,j}$'s obtained by substituting Eq. 4.79 in Eq. 4.78 and equating the coefficients of $\exp[-(m+j)z]$ are

$$W_{1,j} = \frac{\beta k^2 (m+j) N_{1,j}}{\left([m+j]^2 - k^2\right)^2}, \quad \text{(4.80a)}$$

$$N_{1,j+1} = -\frac{W_{1,j}}{(m+j+1)^2 - (m+j+1) - (\sigma + k^2)}. \quad \text{(4.80b)}$$

Similarly, the decaying homogeneous solution of Eq. 4.78b $(W_{2,0} + W_{3,0}z)\exp(-kz)$ where $W_{2,0}$ and $W_{3,0}$ are the unknowns to be determined from the boundary condition Eq. 4.78c drives series' with suffixes '2' and '3' with the

coefficients given by

$$N_{3,j+1} = -\frac{W_{3,j}}{(k+j+1)^2 - (k+j+1) - (\sigma + k^2)}, \tag{4.81a}$$

$$N_{2,j+1} = \frac{N_{3,j}[2(k+j+1)-1] - W_{2,j}}{(k+j+1)^2 - (k+j+1) - (\sigma + k^2)}, \tag{4.81b}$$

$$W_{3,j+1} = \frac{\beta k^2 (k+j+1) N_{3,j+1}}{\left[(k+j+1)^2 - k^2\right]^2}, \tag{4.81c}$$

$$W_{2,j+1} = \frac{\beta k^2 [(k+j+1)N_{2,j+1} - N_{3,j+1}] + 4W_{3,j+1}(k+j+1)\left[(k+j+1)^2 - k^2\right]}{\left[(k+j+1)^2 - k^2\right]^2}. \tag{4.81d}$$

The boundary condition at $z = 0$ in Eq. 4.78c gives three algebraic equations for the three unknowns σ, $W_{2,0}$, and $W_{3,0}$ and these equations are solved by Newton-Raphson iteration. It is clear that the series Eq. 4.79 converge as $M \to \infty$ since the coefficients in Eqs. 4.80 and 4.81 decay at least as fast as $1/j^4$. The comparison between the growth rates obtained from the series solution and the long wavelength theory with $Pe \gg 1$ shown in Fig. 4.4(a) indicates that the solutions agree for sufficiently small k establishing the validity of the series solution. Growth rates for finite values of wavenumber for the unbounded suspension obtained from the series solution are given in Fig. 4.4(b). We ensure the convergence of the series solution noting the good agreement between solutions with $M = 10$ and $M = 20$ in figure 4. As expected, for large enough k, diffusion starts stabilizing the suspension with the associated decrease in the growth rate and eventually the suspension becomes stable after the cut-off wavenumber k_{cut} defined as the non-zero horizontal intercepts of curves in Fig. 4.4(b). For $0 < k < k_{cut}$ most dangerous modes exist for all cases with a wavenumber k_m defined as the point at which the growth rate is the maximum. Fig. 4.4(b) shows that $k_m = O(1)$ (though less than unity) which means that the wavelength of the most dangerous mode is of the order of the boundary layer thickness κ/U_0

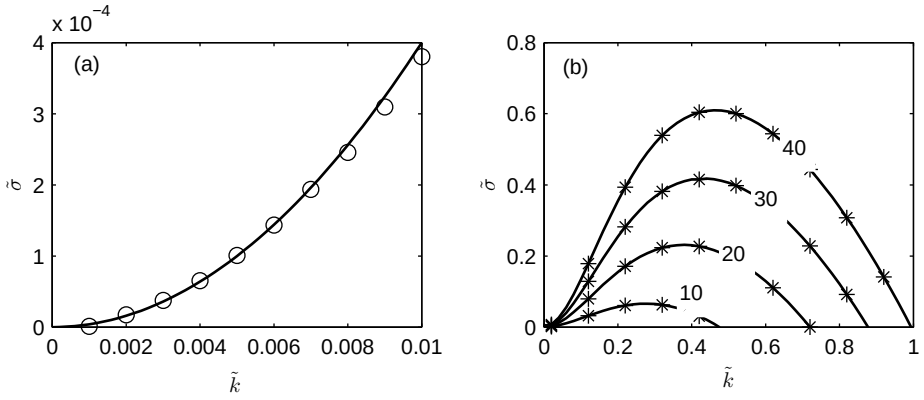

Figure 4.4: Growth rates for semi-infinite suspensions obtained from the series solution. (a) Comparison with the long wavelength theory with $Pe \gg 1$ (shown by solid line) in §3 Eq. 4.38 (with σ and k being rescaled appropriately) for $M = 10$ and $\beta = 10$. (b) Growth rates at finite k for various β as indicated. Solid lines are with $M = 10$ and asterisks are for $M = 20$.

4.6 Numerical solution for finite Pe and k

Determining the nature of solutions for $Pe = O(1)$ and finite k requires full numerical solution of the governing equations Eqs. 4.27. As noted in section 3, such a solution is required to find the fastest growing mode for $Pe = O(1)$. We adopt a spectral collocation method in which the dependent variable $N(z)$ is expanded as a truncated series of basis functions $\phi_j(z)$'s which satisfy the no-flux boundary conditions

$$N(z) = \sum_{j=0}^{M} a_j \phi_j(z), \tag{4.82}$$

where

$$\phi_0(z) = \exp(-Pez), \tag{4.83a}$$

$$\phi_j(z) = \exp\left(-\frac{Pe}{2}z\right)\left(\sin j\pi z - \frac{2j\pi}{Pe}\cos j\pi z\right), \quad j = 1, 2, 3... \tag{4.83b}$$

in which ϕ_0 corresponds to the eigen function in the long wavelength case (see Eq. 4.31). These basis functions are the solutions of the Sturm-Liouville problem closely related to the left hand side of bacteria conservation equation, Eq. 4.27a

$$\left(D^2 + PeD + \lambda_j^2\right)\phi_j = 0, \tag{4.84a}$$

$$\left(Pe + D\right)\phi_j = 0 \quad \text{at } z = 0, 1. \tag{4.84b}$$

The series expansion for $W(z)$

$$W(z) = \sum_{j=0}^{M} a_j \psi_j(z). \tag{4.85}$$

is obtained by substituting Eq. 4.82 into Eq. 4.27b and solving the resultant inhomogeneous fourth order ordinary differential equation analytically with no-slip boundary conditions. The form of $\psi_j(z)$ is given in the Appendix 4.11. Substituting Eq. 4.85 in Eq. 4.27a and re-writing it yields

$$\sum_{j=0}^{M} a_j H_j(z) = \sigma \sum_{j=0}^{M} a_j \phi_j(z), \tag{4.86}$$

where

$$H_j(z) = \left(D^2 + PeD - k^2\right)\phi_j(z) - Pe\psi_j(z)Dn_0(z).$$

The differential eigen value problem Eq. 4.86 is then converted to a generalized linear algebraic eigen value problem by collocating at M discrete points in $z\epsilon(0, 1)$.

$$\sum_{j=0}^{M} H_{ij} a_j = \sigma \sum_{j=0}^{M} \phi_{ij} a_j, \tag{4.87}$$

where $H_{ij} = H_j(z_i)$ and $\phi_{ij} = \phi_j(z_i)$. We choose equi-distant collocation points such that $z_i = \frac{1+i}{M+1}$ with $i = 0, 1, 2...M-1$ and solve the generalized linear eigen value problem Eq. 4.87 using the QZ algorithm. The neutral curves ($\sigma = 0$) are then obtained by using the bisection method.

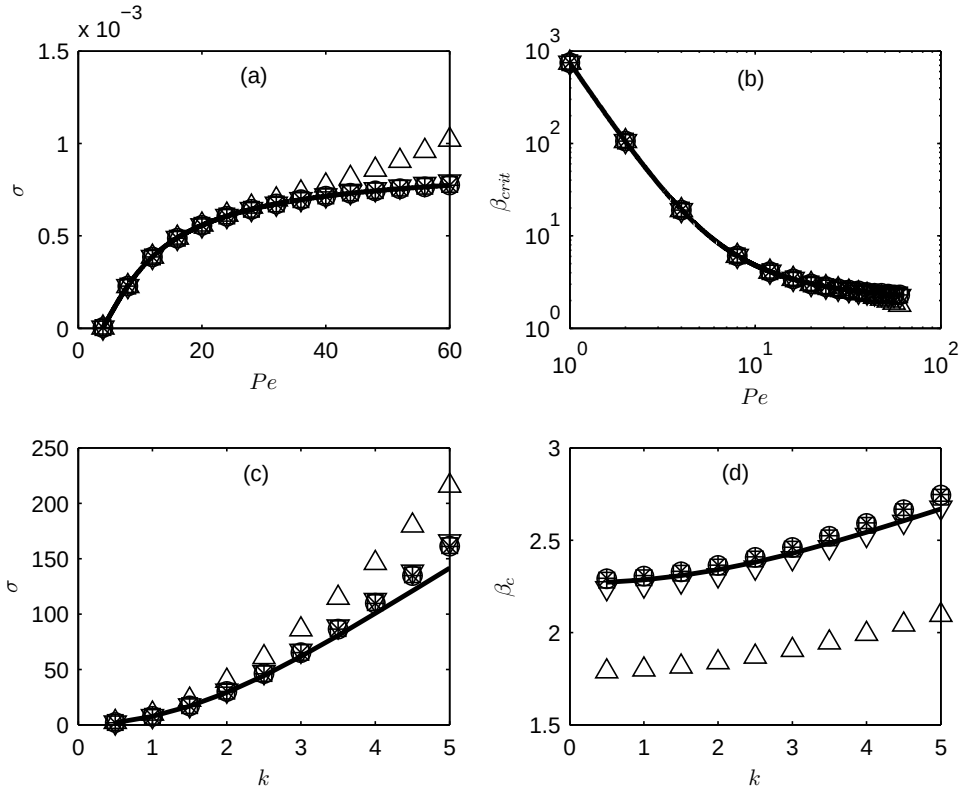

Figure 4.5: Validation of the spectral solution. (a) Comparison of growth rates and (b) neutral curves obtained from the spectral solution with different number of grid points (shown by symbols) and the long-wavelength theory at $k = 0.01$. (c) Comparison of the growth rates from the spectral and the asymptotic solution for deep channels at $Pe = 60$. (d) Neutral curves from the spectral and the deep channel asymptotic solution at $Pe = 60$. Growth rates in (a) and (c) are at $\beta = 20$. Number of grid points in the spectral solution corresponding to various symbols are $\triangle$ $M = 40$, $\bigtriangledown$ $M = 80$, $\square$ $M = 120$, $\bigcirc$ $M = 160$, and $*$ $M = 200$.

4.6.1 Validation of the numerical solution

The numerical solution has been validated by comparing it with the growth rates and neutral curves obtained from the long wavelength theory and the deep channel theory. The comparison presented in Fig. 4.5 shows that the spectral so-

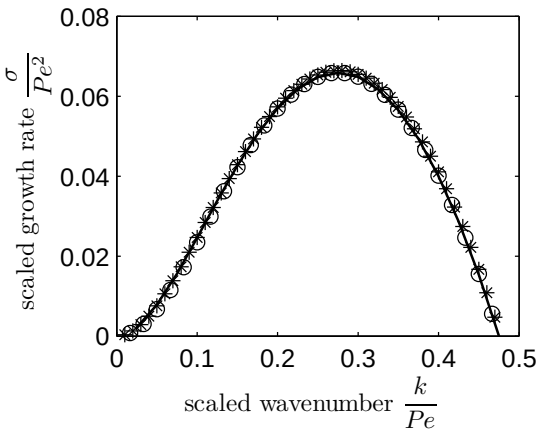

Figure 4.6: Comparison of the spectral solution at different Pe (shown by symbols) and the series solution for semi-infinite channels in §4.5 (shown by the solid line) for different values of Pe. $\bigcirc$ $Pe = 30$ and $*$ $Pe = 50$. $\beta = 10$ for all cases.

lution converges to analytical solutions after about 80 collocation points. As anticipated earlier, it is clear from Figs. 4.5(c) and (d) that the asymptotic solution for $Pe \gg 1$ is accurate when $k = O(1)$. We also found that the spectral solution is accurate only when $Pe < 80$ or so and the accuracy could not be improved by increasing the number of collocation points. Nonetheless, a comparison with the series solution for semi-infinite suspensions shows that the spectral solution correctly reproduces the scaling $\sigma \sim Pe^2$ as seen Fig. 4.6. In Fig. 4.6, when the growth rate and wavenumber are appropriately scaled, all data points collapse onto a single curve which is in excellent agreement with the series solution even for a moderate $Pe = 30$. Thus the $Pe < 80$ range is good enough to explore all the dynamics of the problem.

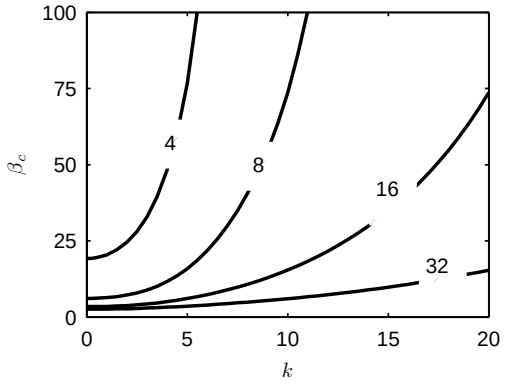

Figure 4.7: Neutral curves β_c versus k for different Pe. The critical wavenumber for instability k_{crit} at which the neutral curve has a minimum is zero for all cases implying that β_{crit} obtained from the long wavelength analysis in §4.4 is the true critical concentration for instability.

4.6.2 Results

We begin by presenting the neutral curves, β_c versus k for various values of Pe in Fig. 4.7. Since the critical wavenumber at which the neutral curve has a minimum is zero for all cases, the marginal stability limit obtained from the long wavelength analysis in §4.4 is indeed the true marginal stability limit. Nonetheless $\beta_c(k)$ would be the critical wavenumber in a numerical simulation conducted with periodic boundary conditions in the x direction with a box length of $2\pi/k$. When $\beta > \beta_c$, all modes with wavenumber lying between $k_{crit} = 0$ and the cut-off wavenumber k_{cut} will be unstable with the wavenumber of the most dangerous mode k_m which will lie somewhere between the two limits. Here k_{cut} for a given value of $\beta > \beta_c$ and Pe is given by the intersection of the horizontal line corresponding to the chosen value of β and the neutral curve corresponding

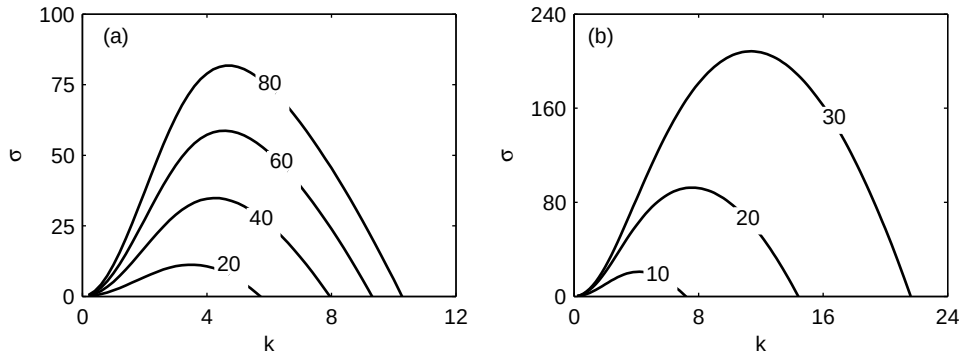

Figure 4.8: Variation of the growth rate σ with wavenumber k for (a) different values of β at $Pe = 8$ and (b) different values of Pe at $\beta = 20$.

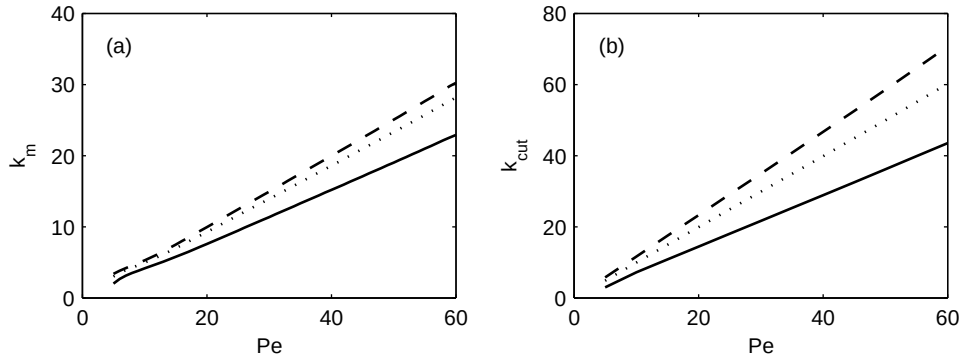

Figure 4.9: Variation of the wavelength of the most dangerous mode k_m (in (a)) and the cut-off wavelength k_{cut} (in (b)) with Pe for $\beta = 20$ (shown by solid line), 40 (dots), and 60 (broken line).

to the Pe specified. Figures 4.8(a) and (b) show the variation of the growth rate with wavenumber for different values of β and Pe respectively. It is clear that the suspension is destabilized when either the bacterial chemotaxis, suspension depth, or the bacterial concentration is increased. For all cases, a mode of maximum growth rate exists with a wavenumber k_m along with a cut-off mode with wavenumber k_{cut}. The variation of k_m and k_{cut} with Pe is given in Figs. 4.9(a) and (b) respectively. It is seen in Figs. 4.9(a) and (b) that both k_m and k_{cut} scale with Pe. Thus unless β is arbitrarily close to β_{crit}, the wavelength of the most dangerous mode and the cut-off wavelength are comparable to the channel gap width for $Pe = O(1)$ or the boundary layer thickness κ/U_0 for $Pe \gg 1$. We also provide the profiles of the fluid velocity in the x direction for most dangerous modes at $Pe = 50$ and $\beta = 5$ ($k_m = 8.03$) and $\beta = 50$ ($k_m = 24.37$) in Fig. 4.10 to show the vertical extent of the fluid flow. It is interesting to note that while the flow covers the entire channel for the $\beta = 5$ case, there is practically no flow after a quarter of the channel depth in the $\beta = 50$ case. The difference in the vertical length scale emerges from the fact that the most dangerous mode wavelength is of the order of the channel depth for the first case since $k_m = O(1)$ and of the order of the boundary layer thickness κ/U_0 for the second case since $k_m = O(Pe)$. As pointed out in §4.5.3 outside the boundary layer the vertical length scale and horizontal length scales of the fluid flow are of the same order since they are determined primarily by the incompressibility constraint.

For all cases discussed so far, the growth rate σ is purely real and the instability is stationary. However, for larger values of β and Pe oscillatory solutions do appear with the imaginary part of σ being non-zero. Fig. 4.11 depicts such a case for $Pe = 15$ and $\beta = 300$. In Fig. 4.11, for sufficiently large values of k, a second mode becomes unstable and both the first and second modes are station-

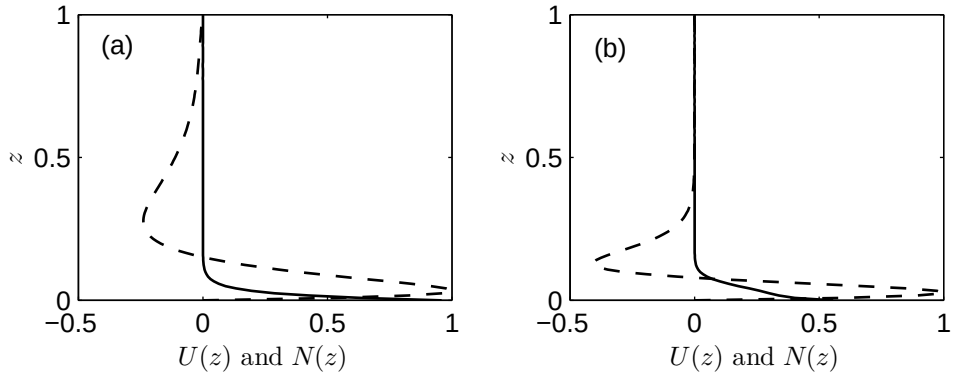

Figure 4.10: Eigen functions corresponding to the most dangerous mode for $Pe = 50$ and (a) $\beta = 5$ with $k_m = 8.03$ and (b) $\beta = 50$ for $k_m = 24.37$. Solid lines show the profiles of the number density mode $N(z)$ and broken lines show the profiles of the x fluid velocity $U(z)$. In order to be represented in the same plot as number density, velocities are rescaled by their maximum magnitudes which are 0.007 for the first case and 0.068 for the second case.

ary until k reaches some k^* after which both modes share the same real part of σ but with equal and opposite imaginary part. These complex conjugate growth rates signify travelling waves propagating along both x and $-x$ directions. For $k > k_{cut}$ the waves are damped. Fig. 4.12 shows the number density modes and streamline patterns for the stationary and oscillatory branches of the solution respectively. The mode corresponding to the upper stationary branch of Fig. 4.11 shown in Fig. 4.12(a) contains only two cells per wavelength while the mode corresponding to the lower stationary branch of Fig. 4.11 contains four cells per wavelength as seen in Fig. 4.12(b). The additional cells that appear near the bottom wall in the latter case convect bacteria back from regions with excess number density to regions of lesser number density offsetting part of the destabilizing flux and reducing the growth rate. Thus the fastest growing mode

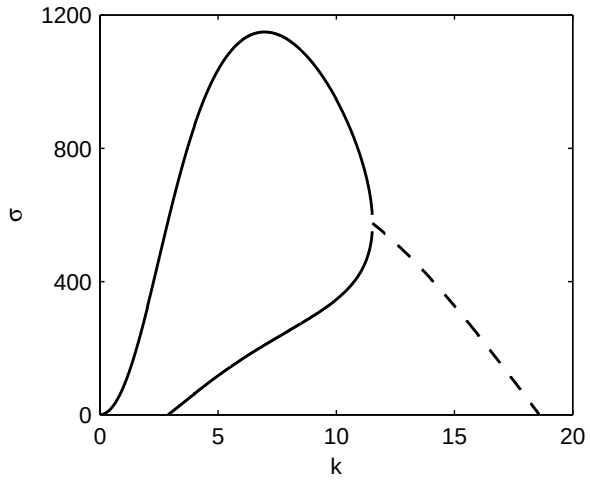

Figure 4.11: Growth rate (real part of σ) versus wavenumber k for $Pe = 15$ and $\beta = 300$. The solid lines indicate stationary solutions with imaginary part of σ being zero and the broken line indicates complex conjugate oscillatory solutions.

.

in the stationary regime will always be the two cell mode shown in Fig. 4.12(a). The oscillatory modes shown in Figs. 4.12(c) and (d) have mirror symmetry as expected and are remarkably different from the stationary modes in the sense that the cells bend left or right at the bottom wall depending their direction of propagation.

From an experimental point of view, it is important to anticipate the mode of instability that is going to be realized. To aid this, we provide the boundary separating the stationary and oscillatory instabilities in β - Pe space in Fig. 4.13(a) and the transition wavenumber k^* above which the modes become oscillatory versus Pe in Fig. 4.13(b). For $Pe < 10$ or so, the required β for oscillatory solutions increases sharply with decreasing Pe and since $\beta = O(\langle n_0 \rangle L^3 Pe)$, it is clear from the figure that one needs $Pe > 25$ or so in order to access the regime

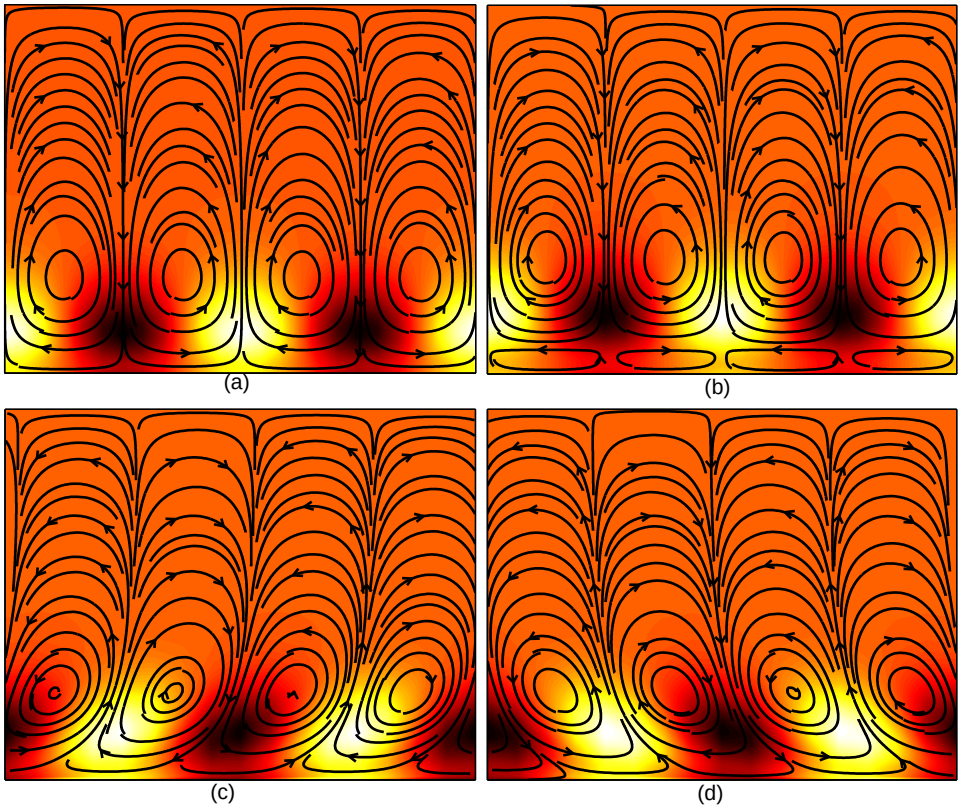

Figure 4.12: Number density modes (shown by the color contours) and streamline patterns for stationary (at $k = 10$) and oscillatory (at $k = 15$) instabilities at $Pe = 15$ and $\beta = 300$. Brighter and darker regions indicate a higher and lower bacteria number density than the base state. (a) Leading stationary mode (b) lagging stationary mode (c) left-propagating oscillatory mode (d) right-propagating oscillatory mode.

of oscillatory instability in a moderately dense suspension with $\langle n_0 \rangle L^3 < 10$. For typical bacterial parameters this translates into a channel depth requirement of the order of a millimeter. Furthermore, the likelihood for oscillatory modes to be realized in an experiment depends upon whether the most dangerous mode is oscillatory or not. Since $k_m < k^*$ always in Fig. 4.13(b) we conclude that the most dangerous mode is always stationary at least in the parameter space that we tested here. Nevertheless, one could isolate the oscillatory modes in a simu-

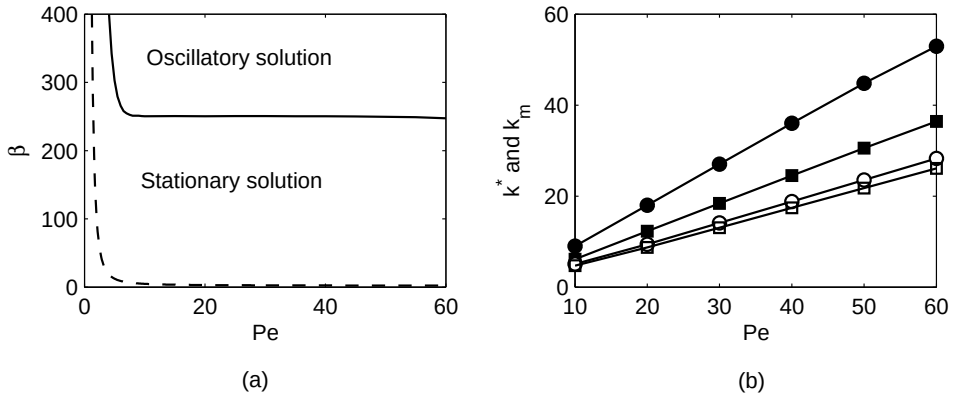

Figure 4.13: (a) Boundary separating the stationary and oscillatory solutions in β - Pe space. For comparison, the marginal stability curve is shown by the broken line. (b) Variation of the wavenumber of the most dangerous mode k_m (unfilled symbols) and the critical wavenumber k^* above which oscillatory modes exist (filled symbols) with Pe for $\beta = 260$ (circles) and 500 (squares).

lation by performing the simulations with periodic boundary conditions in the x direction that admit only the wavenumbers corresponding to the oscillatory modes.

4.7 Effect of shear rotation

In general, the orientations of bacteria are influenced by both the chemical attractant gradient which alters the tumbling frequency of the bacteria and the fluid velocity gradient which rotates the cells. Previous studies (Simha & Ramaswamy, 2002; Saintillan & Shelley, 2008*a*,*b*; Subramanian & Koch, 2009; Subramanian *et al.*, 2011) have focused on instabilities induced by rotation due to the fluid shear. In the preceding sections of the present paper we discussed an

instability resulting from coupling of the bacterial stress due to varying bacteria number density and the convective transport of the bacteria. For simplicity, we neglected the rotation of the cells by the fluid velocity gradient and assumed their orientation distribution was governed solely by their biased tumbling in the chemical gradient field. In the present section we will first derive the governing equations for the large length scale behavior of a bacterial suspension whose orientation distribution responds to both chemical and fluid velocity gradients and then perform a stability analysis of these equations to determine the effect of shear-induced rotation on the number density instability.

4.7.1 Derivation of conservation equations of a chemotactic bacterial suspension

Previous investigations of shear-rotation-induced instabilities of microswimmer suspensions (Simha & Ramaswamy, 2002; Saintillan & Shelley, 2008*a*,*b*; Subramanian & Koch, 2009; Subramanian *et al.*, 2011) have performed stability analyses directly on the kinetic equation, the equation for the one-swimmer orientation and spatial probability $\Omega(\boldsymbol{p}, \boldsymbol{x}, t)$. However, over large length and time scales we may expect the suspension behavior to be described by continuum conservation equations for the bacteria number density $n(\boldsymbol{x}, t)$ and the fluid velocity $\boldsymbol{u}(\boldsymbol{x}, t)$. Our analysis of the chemotaxis-active-stress-convective instability in the preceding sections like the previous analyses of gravity-driven bioconvection (Hill *et al.*, 1989) was based on such continuum equations. In order to perform a continuum analysis of a suspension including both fluid shear induced rotation and chemogradient induced biased tumbling, we require a systematic

derivation of the continuum equations for a weak chemical gradient and weak fluid shear rate. The first, partial effort in this direction was made by Bearon & Pedley (2000) and Bearon (2003) who derived macro-transport equations for suspensions of chemotactic bacteria in a specified fluid flow. We will point out the differences between their continuum equations and the equations derived here later in this section.

We begin the formulation by writing the non-dimensional form of the kinetic equation Eq. 4.1 as

$$\widehat{H}^{-1}\left\{\frac{\partial\Omega}{\partial t}+\nabla\cdot(\boldsymbol{p}\Omega)\right\}+De[\nabla\cdot(\boldsymbol{u}\Omega)+\nabla_{\boldsymbol{p}}\cdot(\dot{\boldsymbol{p}}\Omega)]+\frac{\Omega}{\tau^*}-\frac{1}{4\pi}\int\frac{\Omega}{\tau^*}d\boldsymbol{p}=0, \quad (4.88)$$

where $(\tau^*)^{-1}$ is the tumbling frequency non-dimensionalized by τ_0^{-1}, $\widehat{H} = H/(U_s\tau_0)$ is the ratio of the channel thickness to the bacterial persistence length, and De is a "Deborah number" defined as $De = V_f\tau_0/H$ where V_f is a generic fluid velocity scale. Here H can be viewed as a generic length scale characterizing the spatial extent of the flow. Using a generic fluid velocity makes the equations derived suitable for describing the suspension dynamics in circumstances that not only involve bacteria stress driven flows but also externally imposed fluid flows. Since the active stress is a function of the bacterial orientation field which relaxes due to tumbling, one may consider a bacterial suspension as a viscoelastic fluid with a characteristic relaxation time scale equal to the inverse tumbling frequency τ_0 so that the Deborah number defined above is the ratio of the relaxation time scale to the time scale of fluid motion. We assume that bacteria are slender so that their rotation rate due to fluid shear is given by $\dot{\boldsymbol{p}} = \boldsymbol{\omega}\cdot\boldsymbol{p}+(\boldsymbol{I}-\boldsymbol{pp})\cdot(\boldsymbol{e}\cdot\boldsymbol{p})$ with $\boldsymbol{e} = (1/2)(\nabla\boldsymbol{u}+\nabla\boldsymbol{u}^\dagger)$ and $\boldsymbol{\omega} = (1/2)(\nabla\boldsymbol{u}^\dagger-\nabla\boldsymbol{u})$. To derive Eq. 4.88 we have used the suspension depth H, bacteria swimming velocity U_s, and the ratio H/U_s as the characteristic scales for length, velocity, and time respectively.

The corresponding evolution equation for the bacteria number density obtained after integrating Eq. 4.88 in the orientation space is

$$\frac{\partial n}{\partial t} + \nabla \cdot (\boldsymbol{q} + \widehat{H} De \boldsymbol{u} n) = 0, \tag{4.89}$$

in which the swimming flux $\boldsymbol{q}$ is given by the first moment of the probability density as

$$\boldsymbol{q} = \int \Omega \boldsymbol{p} d\boldsymbol{p}. \tag{4.90}$$

Finally as mentioned in §4.3 the fluid velocity field $\boldsymbol{u}(\boldsymbol{x}, t)$ in Eq. 4.89 is governed by Stokes equations Eq. 4.13 which when written in non-dimensional form is

$$\nabla \cdot \boldsymbol{u} = 0, \tag{4.91a}$$

$$-\nabla p + \nabla^2 \boldsymbol{u} + \frac{8\beta_G}{3De\widehat{H}} \nabla \cdot \sigma^B = 0, \tag{4.91b}$$

Here, the pressure has been scaled by the viscous stress $\mu V_f / H$ for generality and the quantity $\beta_G = 3/8 C n_G L^2 H$ is a generalized version of the β parameter based on a generic number density n_G. The non-dimensional bacterial stress given by the second moment of the probability density in the orientation space is

$$\boldsymbol{\sigma}^B(\boldsymbol{x}, \boldsymbol{p}, t) = -\int \Omega \left(\boldsymbol{pp} - \frac{\boldsymbol{I}}{3} \right) d\boldsymbol{p}. \tag{4.92}$$

Equations 4.89 and 4.91 with Eq. 4.92 govern the long length scale behavior of the bacterial suspension and our goal now is to obtain continuum constitutive equations for the flux $\boldsymbol{q}$ and the bacteria stress $\boldsymbol{\sigma}^B$ in Eqs. 4.90 and 4.92. Since there is neither a net swimming flux nor a deviatoric bacterial stress for an isotropic bacterial suspension as per Eqs 4.90 and 4.92, the aforementioned constitutive relations arise from the deviation of the probability density from isotropy given by

$$\Omega' = \Omega - \frac{n}{4\pi}, \tag{4.93}$$

so that the swimming flux and the deviatoric bacteria stress are now given by

$$\boldsymbol{q} = \int \Omega' \boldsymbol{p} d\boldsymbol{p}, \tag{4.94a}$$

$$\boldsymbol{\sigma}^B = -\int \Omega' \left(\boldsymbol{pp} - \frac{\boldsymbol{I}}{3} \right) d\boldsymbol{p}, \tag{4.94b}$$

where Ω' satisfies the normalization condition $\int \Omega' d\boldsymbol{p} = 0$. The governing equation for Ω' obtained by subtracting $\widehat{H}^{-1}/(4\pi)$ times the number density equation Eq. 4.89 from Eq. 4.88 is

$$\begin{aligned} \widehat{H}^{-1} \quad & \left[\frac{\partial \Omega'}{\partial t} + \nabla \cdot \left(\Omega' \boldsymbol{p} - \frac{1}{4\pi} \int \Omega' \boldsymbol{p} d\boldsymbol{p} \right) \right] + De[\nabla \cdot (\boldsymbol{u}\Omega') + \nabla_{\boldsymbol{p}} \cdot (\dot{\boldsymbol{p}}\Omega')] + \frac{\Omega'}{\tau^*} \\ - \quad & \frac{1}{4\pi} \int \frac{\Omega'}{\tau^*} d\boldsymbol{p} = -\Bigg[\left(\frac{n}{4\pi} \right) \left(\frac{1}{\tau^*} - \frac{1}{4\pi} \int \frac{1}{\tau^*} d\boldsymbol{p} \right) + De \nabla_{\boldsymbol{p}} \cdot \left(\frac{n}{4\pi} \dot{\boldsymbol{p}} \right) \\ + \quad & \widehat{H}^{-1} \boldsymbol{p} \cdot \nabla \left(\frac{n}{4\pi} \right) \Bigg], \end{aligned} \tag{4.95}$$

The terms on the right hand side of Eq. 4.95 are the sources for the anisotropy in the orientation field. The first term in parentheses on the right hand side is $O(\zeta)$ at the leading order for weak chemotaxis and acts as source of orientational anisotropy through the biased tumbling of isotropically oriented bacteria. The $O(De)$ and $O(\widehat{H}^{-1})$ terms on the right hand side are the sources of anisotropy arising from the rotation of bacteria by fluid shear and the spatial variations in the number density. Thus for a bacterial suspension that is weakly perturbed from the state of isotropic swimming for small $\widehat{H}^{-1}$, De, and ζ, we get the first effects of biased bacterial tumbling, fluid flow, and non-uniform bacterial concentration field on the orientation field at the respective orders. In general we should consider the possibility that all three small parameters could be of the same order and our equations could exhibit coupled shear, non-homogeneity, and chemogradient bias effects. Thus a perturbation solution for Ω' in the fol-

lowing form can be sought

$$\begin{aligned}\Omega' &= \Omega'_{000} + (\zeta\Omega'_{001} + De\Omega'_{010} + \widehat{H}^{-1}\Omega'_{100}) \\ &+ (\zeta^2\Omega'_{002} + De^2\Omega'_{020} + \widehat{H}^{-2}\Omega'_{200} + \zeta De\Omega'_{011} + \widehat{H}^{-1}De\Omega'_{110} + \zeta\widehat{H}^{-1}\Omega'_{101}) \\ &+ O(\zeta^3, De^3, \widehat{H}^{-3}, ...). \end{aligned} \tag{4.96}$$

with the normalization condition

$$\int \Omega'_{ijk} d\boldsymbol{p} = 0, \tag{4.97}$$

for i, j, and k being equal to 0, 1, or 2. The orientation field remains isotropic in the absence of biased tumbling, fluid flow, or number density field inhomogeneity and indeed Eqs. 4.95 and 4.97 show that the $O(1)$ deviation of the orientation field from isotropy is zero $\Omega'_{000} = 0$.

Substituting Eq. 4.96 in Eq. 4.94 we obtain continuum constitutive relations for swimming flux and bacteria stress as perturbation series

$$\begin{aligned}\boldsymbol{q} &= (\zeta\boldsymbol{q}_{001} + De\boldsymbol{q}_{010} + \widehat{H}^{-1}\boldsymbol{q}_{100}) \\ &+ (\zeta^2\boldsymbol{q}_{002} + De^2\boldsymbol{q}_{020} + \widehat{H}^{-2}\boldsymbol{q}_{200} + \zeta De\boldsymbol{q}_{011} + \widehat{H}^{-1}De\boldsymbol{q}_{110} + \zeta\widehat{H}^{-1}\boldsymbol{q}_{101}) \\ &+ O(\zeta^3, De^3, \widehat{H}^{-3}, ...), \end{aligned} \tag{4.98a}$$

$$\begin{aligned}\boldsymbol{\sigma}^B &= (\zeta\boldsymbol{\Sigma}^{001} + De\boldsymbol{\Sigma}^{010} + \widehat{H}^{-1}\boldsymbol{\Sigma}^{100}) \\ &+ (\zeta^2\boldsymbol{\Sigma}^{002} + De^2\boldsymbol{\Sigma}^{020} + \widehat{H}^{-2}\boldsymbol{\Sigma}^{200} + \zeta De\boldsymbol{\Sigma}^{011} + \widehat{H}^{-1}De\boldsymbol{\Sigma}^{110} + \zeta\widehat{H}^{-1}\boldsymbol{\Sigma}^{101}) \\ &+ O(\zeta^3, De^3, \widehat{H}^{-3}, ...). \end{aligned} \tag{4.98b}$$

As we shall see, the $O(\zeta)$ stress and flux terms correspond to the chemotactic flux and the normal stress exerted by bacteria as in Eq. 4.12 in §4.3 and the $O(\zeta^2)$ terms are just corrections for the $O(\zeta^2)$ bias in bacterial tumbling frequency

$$\tau^{*-1} = 1 - \zeta\boldsymbol{p}\cdot\boldsymbol{g}\mathcal{H}(\boldsymbol{p}\cdot\boldsymbol{g}) + \frac{\zeta^2}{2}[\boldsymbol{p}\cdot\boldsymbol{g}\mathcal{H}(\boldsymbol{p}\cdot\boldsymbol{g})]^2 + O(\zeta^3). \tag{4.99}$$

The $O(De)$ and $O(\widehat{H}^{-1})$ terms could be expected to be the analogue of Newtonian viscous stress and Fickian mass transport and $O(De^2)$ and $O(\widehat{H}^{-2})$ terms would introduce weak viscoelasticity (second order fluid) and weak non-continuum effects (Burnett) respectively. The other second order terms would bring the coupled effects of chemotaxis, fluid flow, and discreteness of the suspension.

It is straightforward to solve Eq. 4.95 with Eqs. 4.96 and 4.97. At $O(\zeta)$ the biased tumbling of bacteria determines Ω'_{001} as

$$\Omega'_{001} == -\left(\frac{n}{4\pi}\right)\left(\frac{1}{\tau^*} - \frac{1}{4\pi}\int \frac{1}{\tau^*} d\boldsymbol{p}\right) = \frac{n}{4\pi}\left[\boldsymbol{p}\cdot\boldsymbol{g}\mathcal{H}(\boldsymbol{p}\cdot\boldsymbol{g}) - \frac{1}{4}\right], \tag{4.100}$$

which is same as the product of the number density and the $O(\zeta)$ anisotropic orientation field in Eq. 4.10. Thus in Eq. 4.98a this term gives rise to the chemotactic flux

$$\boldsymbol{q}_{001} = \frac{1}{6} n \boldsymbol{g}, \tag{4.101}$$

and in Eq. 4.98b we obtain the chemotaxis induced normal stress

$$\boldsymbol{\Sigma}^{001} = -\frac{n}{16}\left(\boldsymbol{g}\boldsymbol{g} - \frac{\boldsymbol{I}}{3}\right). \tag{4.102}$$

The dimensional version of the chemotactic flux and normal stress in Eqs. 4.101 and 4.102 are identical to the $\boldsymbol{U}_0 n$ and the $\boldsymbol{\sigma}^B$ terms Eqs. 4.12 and 4.15 respectively.

The $O(De)$ deviation from the isotropic state is determined by the fluid shear acting on the isotropic orientation field

$$\Omega'_{010} = -\nabla_{\boldsymbol{p}} \cdot \left(\frac{n}{4\pi}\dot{\boldsymbol{p}}\right) = \frac{3n}{4\pi}\nabla\boldsymbol{u} : \boldsymbol{p}\boldsymbol{p}. \tag{4.103}$$

Since Ω'_{010} is even in $\boldsymbol{p}$, no net swimming flux arises from this term in Eq. 4.98a so that $\boldsymbol{q}_{010} = 0$. This is a consequence of the fact that only the straining com-

ponent of the fluid shear alters the orientation field since the vorticity component merely rotates an isotropic orientation field leaving it unaltered. Owing to the symmetrically located extensional and compressional regions of straining motion, no mean orientation results from its action on the isotropic orientation field. Instead, one gets an enhanced probability of bacterial orientations near the extensional axis of the strain (Subramanian & Koch, 2009). The associated bacterial stress obtained from Eq. 4.98b is

$$\boldsymbol{\Sigma}^{010} = -\frac{n}{5}(\nabla \boldsymbol{u} + \nabla \boldsymbol{u}^{\dagger}), \tag{4.104}$$

is Newtonian since it can be written as $\Sigma^{010} = 2\mu^{b1}\boldsymbol{e}$ where $\boldsymbol{e}$ is the strain rate tensor and $\mu^{b1} = -n/5$ is a "bacterial viscosity". This viscosity is negative since the stress constituted by it acts in the opposite direction of the usual viscous stress owing to the higher fraction of bacteria oriented along the extensional axis of the fluid flow reinforcing the flow with their force-dipoles.

Now at $O(\widehat{H}^{-1})$ the spatial variations in the number density result in an anisotropic orientation field which peaks along the opposite direction of number density gradient

$$\Omega'_{100} = -\frac{\boldsymbol{p} \cdot \nabla n}{4\pi}, \tag{4.105}$$

and this term gives rise to the diffusive flux

$$\boldsymbol{q}_{100} = -\frac{\nabla n}{3}. \tag{4.106}$$

As Ω'_{100} is odd in $\boldsymbol{p}$, no bacteria stress arises from this term so that $\boldsymbol{\Sigma}^{100} = 0$. The orientation anisotropy peaking along the negative bacteria concentration gradient direction is a simple consequence of the $O(1)$ isotropic swimming of bacteria. Since bacteria are equally likely to swim in any direction, a non-uniform concentration field of bacteria causes a net swimming from high to low bacteria

concentration regions and this flux is diffusive as it is proportional to the gradient of bacteria concentration. In dimensional form, this flux is driven by the scalar diffusivity $\kappa = U_s^2\tau_0/3$ (Chen *et al.*, 2003; Bearon & Pedley, 2000; Bearon, 2003). Thus the leading order swimming flux $\zeta\frac{\boldsymbol{g}}{6}n - \widehat{H}^{-1}\frac{\nabla n}{3}$ obtained by the sum of Eqs. 4.101 and 4.106 is constituted by chemotaxis and diffusion without having the effect of shear rotation.

Proceeding in a similar manner, we obtain the full form of the the swimming flux as

$$\begin{aligned}\boldsymbol{q} &= \frac{\zeta}{6}\boldsymbol{g}n - \frac{\widehat{H}^{-1}}{3}\nabla n + \frac{\zeta^2}{48}\boldsymbol{g}n + \frac{De\zeta}{30}(9\boldsymbol{e}+5\boldsymbol{\omega})\cdot\boldsymbol{g}n \\ &- De\widehat{H}^{-1}\left[\frac{14}{15}\boldsymbol{e}\cdot\nabla n + \frac{1}{5}n\nabla^2\boldsymbol{u} - \frac{1}{3}(\boldsymbol{u}\nabla^2 n - \boldsymbol{u}\cdot\nabla\nabla n)\right] \\ &- \frac{\zeta\widehat{H}^{-1}}{8}\left(\boldsymbol{g}\boldsymbol{g} + \frac{\boldsymbol{I}}{3}\right)\cdot\nabla n. \end{aligned} \tag{4.107}$$

To derive Eq. 4.107 we have utilized the fact that $\zeta[\widehat{H}^{-1}\partial n/\partial t + De\nabla\cdot(\boldsymbol{u}n)]$ is only of order $\zeta\widehat{H}^{-1}O(\zeta,\widehat{H}^{-1},De)$ (see Eq. 4.89). The $O(\zeta^2)$ term in Eq. 4.107 is the correction to the chemotactic flux in Eq. 4.101 due to the $O(\zeta^2)$ bias in bacterial tumbling. The $O(De^2)$ flux in Eq. 4.107 is zero since the $O(De^2)$ orientation field does not have a mean orientation as it results from the fluid convection and shear acting on the $O(De)$ deviation from anisotropy in Eq. 4.103 which has no mean orientation. We do not explicitly write the $O(\widehat{H}^{-2})$ contribution to the swimming flux $\boldsymbol{q}_{200} = (1/3)\partial(\nabla n)/\partial t$ since it can be absorbed in the $O(De\widehat{H}^{-1})$ flux term through the relation $\widehat{H}^{-2}\partial(\nabla n)/\partial t = -De\widehat{H}^{-1}(\nabla\boldsymbol{u}\cdot\nabla n + \boldsymbol{u}\cdot\nabla\nabla n)$ at the leading order derived from Eq. 4.89. This leads to the form of the $O(De\widehat{H}^{-1})$ term given in Eq. 4.107 which shows that shear-induced rotation couples with the spatial variation of number density to yield a correction to the diffusive flux through the term $-(14/15)\boldsymbol{e}\cdot\nabla n$. The $O(De\widehat{H}^{-1})$ also includes a drift flux given by the term $-(1/5)n\nabla^2\boldsymbol{u}$ and a flux driven by the convection of higher gradients

of number density as seen in the term that involves $\boldsymbol{u}\nabla^2 n - \boldsymbol{u}\cdot\nabla\nabla n$. The drift flux is due to the coupling of shear-induced rotation and swimming of bacteria and this would cause bacteria to lag the fluid in a pressure driven unidirectional flow.

The first effects of coupling between chemotaxis and fluid flow on swimming flux is given by the $O(\zeta De)$ term Eq. 4.107. This term represents the correction to the chemotactic flux caused by the shear-induced rotation of the mean orientation vector $\langle \boldsymbol{p}\rangle_f$ derived in Eq. 4.11 and this is of $O(\zeta De)$ since the mean orientation $\langle \boldsymbol{p}\rangle_f$ itself is of order ζ and the fluid velocity gradient which rotates this mean orientation is of order De. Finally, the $O(\zeta \widehat{H}^{-1})$ term in Eq. 4.107 is the first correction to the diffusive flux due to biased tumbling and it takes the form of a transversely isotropic diffusivity tensor with a higher diffusivity along the direction of the chemical gradient.

Now the full form of the bacteria stress tensor is

$$\begin{aligned}
\boldsymbol{\sigma}^B &= -\frac{\zeta}{16}\left(\boldsymbol{gg}-\frac{\boldsymbol{I}}{3}\right)n - \frac{2De}{5}n\boldsymbol{e} - \frac{17\zeta^2}{960}\left(\boldsymbol{gg}-\frac{\boldsymbol{I}}{3}\right)n \\
&+ De^2\left\{\frac{2}{5}\left[\nabla\cdot(\boldsymbol{u}n\boldsymbol{e}) + n(\boldsymbol{e}\cdot\boldsymbol{\omega}+\boldsymbol{\omega}^\dagger\cdot\boldsymbol{e})\right] - \frac{12n}{35}\left(\boldsymbol{e}\cdot\boldsymbol{e}-\frac{\boldsymbol{I}}{3}\boldsymbol{e}:\boldsymbol{e}\right)\right\} \\
&- \frac{2\widehat{H}^{-2}}{15}\left(\nabla\nabla n - \frac{\boldsymbol{I}}{3}\nabla^2 n\right) + \zeta De(\boldsymbol{\mu}^{b2}:\boldsymbol{e}) + \frac{2De\widehat{H}^{-1}}{5}\frac{\partial}{\partial t}(n\boldsymbol{e}) \\
&+ \frac{2\zeta\widehat{H}^{-1}}{15}\left[\frac{1}{2}(\boldsymbol{g}\nabla n + \nabla n\boldsymbol{g}) - \frac{\boldsymbol{I}}{3}\boldsymbol{g}\cdot\nabla n\right]. \qquad (4.108)
\end{aligned}$$

While deriving Eq. 4.108 we have once again used the fact that $\zeta[\widehat{H}^{-1}\partial n/\partial t + De\nabla\cdot(\boldsymbol{u}n)]$ is only of order $\zeta\widehat{H}^{-1}O(\zeta,\widehat{H}^{-1},De)$. Thus the leading order bacterial stress in Eq. 4.108 is constituted by the $O(\zeta)$ chemotactic normal stress and the $O(De)$ viscous stress. As one may expect, the $O(\zeta^2)$ correction to the chemotactic bacterial stress in Eq. 4.108 is again a normal stress acting in the same sense as the $O(\zeta)$ chemotactic stress. The $O(De^2)$ bacteria stress in Eq. 4.108 accounts

for the change in bacteria stress due to the fluid velocity gradient acting on the $O(De)$ bacteria stress. The sum of the term in square brackets in the $O(De^2)$ and the $O(De\widehat{H}^1)$ stress has the familiar form of the corotational derivative (see (Bird *et al.*, 1987)) of the tensor $n\boldsymbol{e}$. A portion of this term appears at $O(De\widehat{H}^1)$ because time is non-dimensionalized by the time scale of bacterial swimming H/U_s rather than the time scale of fluid motion H/V_f. If the latter time scale were used to non-dimensionalize time, we would have got the $\partial(n\boldsymbol{e})/\partial t$ term at $O(De^2)$. The sum of the entire $O(De^2)$ and $O(De\widehat{H}^{-1})$ bacteria stresses when written in dimensional form is $C\mu L^2 U_s \tau_0^2\{(2/5)[\partial(n\boldsymbol{e})/\partial t + \nabla\cdot(\boldsymbol{u}n\boldsymbol{e}) + n(\boldsymbol{e}\cdot\boldsymbol{\omega} + \boldsymbol{\omega}^\dagger\cdot\boldsymbol{e})] - (12/35)n[\boldsymbol{e}\cdot\boldsymbol{e} - (\boldsymbol{I}/3)\boldsymbol{e}:\boldsymbol{e}]\}$. For a homogeneous bacterial suspension, the latter is identical to the non-Newtonian part of the stress in the second order constitutive equation $b_2(\partial\boldsymbol{e}/\partial t + \boldsymbol{u}\cdot\nabla\boldsymbol{e} + \boldsymbol{e}\cdot\boldsymbol{\omega} + \boldsymbol{\omega}^\dagger\cdot\boldsymbol{e}) + b_{11}[\boldsymbol{e}\cdot\boldsymbol{e} - (\boldsymbol{I}/3)\boldsymbol{e}:\boldsymbol{e}]$ obtained from the retarded motion expansion (Bird *et al.*, 1987) with $b_2 = (2/5)C\mu L^2 n U_s \tau_0^2$ and $b_{11} = -(12/35)C\mu L^2 n U_s \tau_0^2$. Here b_2 and b_{11} are scalar material constants related to the first and second normal stress differences, $\sigma_{11} - \sigma_{22} = -b_2\Gamma^2$ and $\sigma_{22} - \sigma_{33} = (1/2)\left(b_2 + \frac{b_{11}}{2}\right)\Gamma^2$, respectively with Γ being the shear rate for a simple shear flow. It is clear from Eq. 4.108 that $b_2 > 0$, $b_{11} < 0$, and $b_{11}/b_2 = -6/7$. This means that the first normal stress difference is negative and the second normal stress difference is positive and is in contrast to polymeric fluids (Ho & Leal, 1976) or suspensions of rigid, slender fibers (Brenner, 1974; Petrie, 1999) for which the first normal stress difference is positive and the second normal stress difference is negative. The difference in sign of normal stress differences between a polymeric fluid or a fiber suspension and the bacterial fluid is due to the fact the sign of the stresslets differ in the two cases. A polymer strand or a rigid fiber resists stretching by the shear flow thus creating tension on the fluid along its axis (positive stresslet) while the swimming induced force dipole

on bacteria creates a pressure on the fluid along its axis (negative stresslet). The fact that $b_{11}/b_2 = -6/7$ gives the ratio of the magnitudes of the second to the first normal stress difference as $2/7$ for the bacterial suspension at small shear rates while for a suspension of rigid, passive, Brownian fiber suspension, this ratio is $1/7$ (Brenner, 1974; Petrie, 1999). The reason for this difference is that the orientation distribution of bacteria relaxes through tumbling while that for passive Brownian fibers relaxes through rotational diffusion.

The non-zero first normal stress difference of a bacterial suspension is of particular importance in flows with curved streamlines. Just like polymeric fluids, curvature of streamlines along with normal stress differences would result in hoop stresses in a bacterial suspension flowing through curved pipes or channels and it is well-known that hoop stresses often result in secondary flows (Larson *et al.*, 1990; Joo & Shaqfeh, 1991; Bowen *et al.*, 1991; Fan *et al.*, 2001)) in the plane normal to the axis of the pipe or channel even in the creeping flow limit. These secondary flows arise above a critical Deborah number due to an elastic instability (Larson *et al.*, 1990; Joo & Shaqfeh, 1991) that involves a coupling between the normal stresses and the fluid velocity field in the case of a channel. Secondary flows develop at any finite Deborah number in the case of pipe (Bowen *et al.*, 1991; Fan *et al.*, 2001). Since the normal stresses exerted by bacteria are in the opposite sense of those exerted by a polymer molecule, one may expect the vortices that constitute the elastic-instability driven secondary flow of a bacterial suspension to be centered closer to the inner wall whereas those for a polymeric fluid, which was analyzed by Joo & Shaqfeh (1991), are near the outer wall. Similarly, the steady secondary motion that would exist in a bacterial suspension flowing through a curved pipe of circular cross-section will be directed from the outer bend to the inner bend at the center of the pipe

whereas for a polymeric fluid, it is in the opposite direction (Fan *et al.*, 2001). In the case of bacterial suspensions flowing through micro-channels, the secondary flow is of great importance from the perspective of mixing since the low Reynolds number nature of such flows prevents any inertial mixing. Previous experiments (Pathak *et al.*, 2004; Burghelea *et al.*, 2004) with polymeric fluids have demonstrated that secondary flows are efficient in mixing at low Reynolds numbers.

Proceeding further we see that the first non-continuum correction for the bacterial stress appears at $O(\widehat{H}^{-2})$ in Eq. 4.108 and this is due to non-linear spatial variations in the number density. Next at $O(\zeta De)$ we see the coupling between chemotaxis and shear re-orientation of bacteria. Just as the $O(De)$ bacteria stress in Eq. 4.104 is a Newtonian stress with a scalar viscosity of $\mu^{b1} = -n/5$, the coupling between chemotaxis and diffusion gives a Newtonian stress but with an anisotropic fourth order viscosity tensor (see Subramanian *et al.* (2011))

$$\begin{aligned}\mu^{b2}_{ijkl} &= -n[(11/480)(\delta_{ik}\delta_{jl}+\delta_{il}\delta_{jk}) - (5/96)g_ig_j\delta_{kl} - (1/96)g_ig_jg_kg_l \\ &+ (1/96)(g_ig_l\delta_{jk}+g_ig_k\delta_{jl}) + (7/96)(g_jg_l\delta_{ik}+g_jg_k\delta_{il})]. \qquad (4.109)\end{aligned}$$

As mentioned earlier, the $O(De\widehat{H}^{-1})$ bacterial stress in Eq. 4.108 arises due to temporal variations in the $O(De)$ bacteria stress and finally the coupling between alignment due to biased tumbling in a chemoattractant gradient and due to the spatial variation of bacterial number density yields the $O(\zeta\widehat{H}^{-1})$ bacteria stress in Eq. 4.108.

Thus Eqs. 4.89 and 4.91 with the swimming flux and bacteria stress being given by Eqs. 4.107 and 4.108 constitute the governing equations for a suspension of chemotactic bacteria. One important observation here is that the system of governing equations is a third order partial differential equation for

number density and fluid velocity owing to the presence of the second derivative of those quantities in the $O(De\widehat{H}^{-1})$ term in the expression for flux in Eq. 4.107. Thus one in principle would need more boundary conditions than are usually provided by the physics of the problem in order to have a unique solution for these equations. The same issue arises in the case of the well-known Burnett's equations for rarefied gas flows (Cercignani, 1988; Lee, 1994; Agarwal *et al.*, 2001) obtained from the Chapman - Enskog expansion of the Boltzmann's equation up to $O(Kn^2)$ where Kn is the Knudsen number defined as the ratio between the mean free path of the gas molecules to the macroscopic length scale. In fact the expansion of the probability density here in powers of $\widehat{H}^{-1}$ is analogous to the expansion in powers of Kn since the former is the ratio of the mean free path of the bacteria $U_s\tau_0$ to the macroscopic length scale H. At $O(1)$ the Chapman - Enskog expansion yields Euler's equations of motion and at $O(Kn)$ one gets the Navier - Stokes equations. Thus the dissipative phenomenon of viscous stress appears only at $O(Kn)$ in Chapman - Enskog expansion and at the next order (Burnett) one gets derivatives of the hydrodynamic variables beyond order two. Similarly, diffusion arises in Eq. 4.107 only at $O(\widehat{H}^{-1})$ and at $O(\widehat{H}^{-2})$ we have derivatives of order larger than two for the number density and the fluid velocity. The problem of extra boundary conditions can be eliminated if we perturb the solutions of Eqs. 4.89 and 4.91 with full flux and bacteria stress terms in Eqs. 4.107 and 4.108 as $n = n_1 + n_2$, $\boldsymbol{u} = \boldsymbol{u}_1 + \boldsymbol{u}_2$, and $p = p_1 + p_2$ with the leading terms with subscripts "1" correspond to the solution of the continuum

equations including first order terms in ζ, De and $\widehat{H}^{-1}$:

$$\frac{\partial n_1}{\partial t} + \nabla \cdot \left(\frac{\zeta}{6} \boldsymbol{g} n_1 + De\widehat{H} \boldsymbol{u}_1 n_1 - \frac{\widehat{H}^{-1}}{3} \nabla n_1 \right) = 0, \tag{4.110a}$$

$$\nabla \cdot \boldsymbol{u}_1 = 0, \tag{4.110b}$$

$$-\nabla p_1 + \nabla \cdot \left[\left(1 - \frac{8\beta_G}{15\widehat{H}} n_1 \right) (2\boldsymbol{e}_1) \right] - \frac{\beta_G \zeta}{6De\widehat{H}} \left(\boldsymbol{g}\boldsymbol{g} - \frac{\boldsymbol{I}}{3} \right) \cdot \nabla n_1 = 0, \tag{4.110c}$$

where $\boldsymbol{e}_1 = (1/2)(\nabla \boldsymbol{u}_1 + \nabla \boldsymbol{u}_1^\dagger)$. The leading terms are then refined by the fields with subscripts "2" which are governed by an equation that contains second order terms evaluated using the subscript "1" terms, i.e.,

$$\frac{\partial n_2}{\partial t} + \nabla \cdot \left(\frac{\zeta}{6} \boldsymbol{g} n_2 + De\widehat{H} \boldsymbol{u}_2 n_2 - \frac{\widehat{H}^{-1}}{3} \nabla n_2 \right) = -\nabla \cdot \boldsymbol{q}_1, \tag{4.111a}$$

$$\nabla \cdot \boldsymbol{u}_2 = -\nabla \cdot \boldsymbol{u}_1, \tag{4.111b}$$

$$-\nabla p_2 + \nabla \cdot \left[\left(1 - \frac{8\beta_G}{15\widehat{H}} n_2 \right) (2\boldsymbol{e}_2) \right] - \frac{\beta_G \zeta}{6De\widehat{H}} \left(\boldsymbol{g}\boldsymbol{g} - \frac{\boldsymbol{I}}{3} \right) \cdot \nabla n_2 = -\frac{8\beta_G}{3De\widehat{H}} \nabla \cdot \boldsymbol{\Sigma}^1, \tag{4.111c}$$

where $\boldsymbol{e}_2 = (1/2)(\nabla \boldsymbol{u}_2 + \nabla \boldsymbol{u}_2^\dagger)$ and

$$\begin{aligned}
\boldsymbol{q}_1 &= \frac{\zeta^2}{48}\boldsymbol{g}n_1 + \frac{De\zeta}{30}(9\boldsymbol{e}_1 + 5\boldsymbol{\omega}_1)\cdot\boldsymbol{g}n_1 \\
&\quad - De\widehat{H}^{-1}\left[\frac{14}{15}\boldsymbol{e}_1\cdot\nabla n_1 + \frac{1}{5}n_1\nabla^2\boldsymbol{u}_1 - \frac{1}{3}(\boldsymbol{u}_1\nabla^2 n_1 - \boldsymbol{u}_1\cdot\nabla\nabla n_1)\right] \\
&\quad - \frac{\zeta\widehat{H}^{-1}}{8}\left(\boldsymbol{g}\boldsymbol{g} + \frac{\boldsymbol{I}}{3}\right)\cdot\nabla n_1, \qquad (4.112a) \\
\boldsymbol{\Sigma}^1 &= -\frac{17\zeta^2}{960}\left(\boldsymbol{g}\boldsymbol{g} - \frac{\boldsymbol{I}}{3}\right)n_1 \\
&\quad + De^2\left\{\frac{2}{5}\left[\nabla\cdot(\boldsymbol{u}_1 n_1\boldsymbol{e_1}) + n_1(\boldsymbol{e_1}\cdot\boldsymbol{\omega_1} + \boldsymbol{\omega_1}^\dagger\cdot\boldsymbol{e_1})\right] - \frac{12n_1}{35}\left(\boldsymbol{e_1}\cdot\boldsymbol{e_1} - \frac{\boldsymbol{I}}{3}\boldsymbol{e_1}:\boldsymbol{e_1}\right)\right\} \\
&\quad - \frac{2\widehat{H}^{-2}}{15}\left(\nabla\nabla n_1 - \frac{\boldsymbol{I}}{3}\nabla^2 n_1\right) + \zeta De(\boldsymbol{\mu}^{b2}:\boldsymbol{e}_1) + \frac{2De\widehat{H}^{-1}}{5}\frac{\partial}{\partial t}(n_1\boldsymbol{e_1}) \\
&\quad + \frac{2\zeta\widehat{H}^{-1}}{15}\left[\frac{1}{2}(\boldsymbol{g}\nabla n_1 + \nabla n_1\boldsymbol{g}) - \frac{\boldsymbol{I}}{3}\boldsymbol{g}\cdot\nabla n_1\right], \qquad (4.112b)
\end{aligned}$$

in which $\boldsymbol{\omega}_1 = (1/2)(\nabla \boldsymbol{u}_1^\dagger - \nabla \boldsymbol{u}_1)$. Here in Eq. 4.112b the definition of μ^{b2} is obtained by replacing n by n_1 in Eq. 4.109. Thus the higher derivative terms in Eqs. 4.111 are just forcing terms and the governing equations for the perturbed quantities are still second order partial differential equations. A similar method has been proposed for Burnett equations (see Cercignani (1988)) by expanding the solutions in powers of Kn with the leading solution being given by Navier - Stokes equations.

It is clear from Eq. 4.110c that the leading velocity field is governed by the Stokes momentum equation forced by the chemotactic bacterial stress but with an effective viscosity given by

$$\widehat{\mu}_{eff}(\boldsymbol{x}, t) = 1 - \frac{8\beta_G}{15\widehat{H}}n_1(\boldsymbol{x}, t), \qquad (4.113)$$

in which $\widehat{\mu}_{eff}$ has been scaled by the viscosity of the suspending medium μ. The effective viscosity term combines the usual viscous stress and the $O(De)$ bacterial stress in Eq. 4.104 which is again a Newtonian viscous stress but with

a negative viscosity. Thus the effective viscosity in Eq. 4.113 is always smaller than the Newtonian viscosity ($\mu_{eff} < 1$) and as noted earlier, this is a consequence of the fact that bacterial force-dipoles re-oriented by the $O(De)$ fluid shear augment the fluid flow. As mentioned in §4.2 the orientation shear instability of bacterial suspensions arises from the aforementioned mechanism and in fact Subramanian & Koch (2009) consider the long wavelength orientation shear instability of homogeneous suspensions without any chemical gradient as a result of the effective viscosity in Eq. 4.113 being negative. The critical concentration for the orientation shear instability is then given by the condition of zero effective viscosity and for an unbounded, homogeneous suspension, the latter condition corresponds to $\beta_{G-crit} = 15/8\widehat{H}$ (Subramanian & Koch, 2009). Using the definitions of β_G and $\widehat{H}$ one finds that the critical condition is given by the non-dimensional concentration $\gamma = (C/5)n_G L^2 U\tau_0 = 1$ (Subramanian & Koch, 2009). If the bacterial concentration is larger than this critical value then the momentum equation in Eq. 4.110c is no longer well-posed owing to the negative effective viscosity of the suspension. This break down of the continuum equation is merely a consequence of the violation of the assumption made in Eq. 4.88 that the probability density evolves over a slow time scale of H/U_s. Once the orientation shear instability sets in, the orientation field evolves over a time scale of order $(CnL^2U_s\tau_0)^{-1}$ which at the critical concentration is $O(5\widehat{H})$ times faster than H/U_s.

Finally we wish to point out how the present derivation differs from the works of Bearon & Pedley (2000) and Bearon (2003) in which the coupling between shear rotation and chemotaxis has been analyzed. The primary objective of Bearon & Pedley (2000) and Bearon (2003) is to obtain a macroscopic transport equation for bacteria in the presence of an imposed chemical gradient and a sim-

ple shear flow. As a result, Bearon & Pedley (2000) and Bearon (2003) assume only a one-way coupling between bacterial and fluid motion which involves advection and the rotation of bacteria by the fluid velocity and its gradients respectively but without the bacterial force-dipoles affecting the fluid motion. The latter has been incorporated in our derivation and that leads to coupled equations for bacterial number density and fluid motion. Equation 4.91b shows that bacterial force-dipoles will have a strong influence particularly if the suspension is dense enough to have $\beta_G/(De\widehat{H}) = O(1)$. Furthermore, our number density equation Eq. 4.89 is more general since it allows for inhomogeneous shear fields while the analysis of Bearon & Pedley (2000) and Bearon (2003) is restricted to the case of simple shear flow. We also provide the higher order corrections to the diffusive flux arising from spatio-temporal variations in the number density and fluid flow.

4.7.2 Stability analysis with shear rotation

The analysis in the previous section shows that the primary effect of reorientation of bacteria under weak shear is to reduce the effective viscosity of the suspension. We now examine how this reduced viscosity of the suspension influences the critical concentration for the chemotaxis driven instability analyzed in this paper by performing the stability analysis of the leading order equations, Eq. 4.110. For brevity, we do not attempt to refine the leading solution by solving Eq. 4.111. Since the fluid flow here is driven by the bacterial stress, the fluid velocity scale V_f can be either the swimming velocity or the chemotactic velocity. We chose the latter in previous sections since the fluid flow is driven purely by the normal stresses induced by chemotaxis. However,

the form of the bacterial stress in Eq. 4.98b shows that one can have a bacterial stress that drives the fluid flow even in the absence of any chemotaxis ($\zeta = 0$) as in the case of the orientation shear instability due to negative effective viscosity. As a result, the most appropriate choice of the fluid velocity scale here is the swimming velocity and with that we obtain $De = \widehat{H}^{-1}$. Since the generic number density scale n_G in Eq. 4.91b is now equal to $\langle n_0 \rangle$, β_G is the same as β and by using the fact that $Pe = \widehat{H}\zeta/2$ we re-write the governing equations, Eq. 4.110, and boundary conditions as

$$3\widehat{H}\frac{\partial n}{\partial t} + \nabla \cdot (Pen\boldsymbol{g} + 3\widehat{H}\boldsymbol{u}n - \nabla n) = 0, \tag{4.114a}$$

$$\nabla \cdot \boldsymbol{u} = 0, \tag{4.114b}$$

$$-\nabla p + \nabla \cdot \left[\left(1 - \frac{8\beta_G}{15\widehat{H}}n\right)(\nabla \boldsymbol{u} + \nabla \boldsymbol{u}^{\dagger})\right] - \frac{\beta\zeta}{6}\left(\boldsymbol{gg} - \frac{\boldsymbol{I}}{3}\right) \cdot \nabla n = 0, \tag{4.114c}$$

$$Pen\boldsymbol{g} - \nabla n = \boldsymbol{u} = 0 \quad \text{at } z = 0, 1. \tag{4.114d}$$

with $\boldsymbol{g} = -\boldsymbol{e_z}$. Since we are solving only for the leading continuum variables we have dropped the subscripts here in Eq. 4.114 and the dimensional form of Eq. 4.114a is the same as the number density equation without any shear rotation Eq. 4.12 used in previous sections so that the base-state number density field $n_0(z) = Pe\exp(-Pez)/[1 - \exp(-Pe)]$ remains the same as before.

Linearizing Eqs. 4.114 for small perturbations of the form in Eq. 4.22 about

the base-state yields the amplitude equations

$$\left[D^2 + PeD - \left(\sigma + k^2\right)\right] N = 3\widehat{H} W D n_0, \tag{4.115a}$$

$$ikU + DW = 0, \tag{4.115b}$$

$$D\left[\left(1 - \frac{8\beta}{15\widehat{H}} n_0\right)(DU + ikW)\right] = 2k^2\left(1 - \frac{8\beta}{15\widehat{H}} n_0\right) U + ik\left(P - \frac{\beta\zeta}{18} N\right), \tag{4.115c}$$

$$2D\left[\left(1 - \frac{8\beta}{15\widehat{H}} n_0\right) DW\right] = -ik\left[\left(1 - \frac{8\beta}{15\widehat{H}} n_0\right)(DU + ikW)\right] + D\left(P + \frac{\beta\zeta}{9} N\right). \tag{4.115d}$$

with the boundary conditions $(Pe + D)N = U = W = 0$ at $z = 0$ and $z = 1$. When deriving Eq. 4.115a from Eq. 4.114a the factor of $3\widehat{H}$ has been absorbed into σ so that the growth rate σ is non-dimensionalized by H^2/κ as before. The factor of $3\widehat{H}$ in the unsteady term in Eq. 4.114a arose because time had been non-dimensionalized by H/U_s in this section rather than by the diffusive time scale H^2/κ as in §4.3. In addition, the fluid convective terms in Eqs. 4.115a and 4.23a differ by a factor of $\zeta/6$ since the fluid velocity has been scaled by the swimming velocity in the former and by the chemotactic velocity in the latter.

We now solve Eq. 4.115 in the long wavelength limit, $k \ll 1$, to obtain the neutral curve. A long wavelength analysis is sufficient to predict the marginal stability limits since the lowest critical concentration for both the orientation shear instability (Subramanian & Koch, 2009; Subramanian *et al.*, 2011) and the number density instability (see Fig. 4.7) corresponds to the longest wavelength modes. Expansions for all the dependent variables with respect to k remain the same as Eq. 4.29 in the previous long wavelength analysis since the fluid flow is still driven by essentially the same bacteria stress. As a result, the leading order number density, which is still determined by the balance between chemotaxis

and diffusion, is identical to the exponential in Eq. 4.31. The leading order x momentum equation is

$$D\left\{\left[1-\widehat{\beta}\exp(-Pez)\right]DU_1\right\}=i\left(P_0-\frac{\beta\zeta}{18}N_0\right), \tag{4.116}$$

with boundary conditions $U_1(0)=U_1(1)=0$ and $U_1(z)$ satisfies the incompressibility constraint $\langle U_1\rangle=0$. Here $\widehat{\beta}$ is defined as

$$\widehat{\beta}=\frac{8\beta Pe}{15\widehat{H}[1-\exp(-Pe)]}=\frac{\gamma Pe}{1-\exp(-Pe)}, \tag{4.117}$$

and the effective viscosity here given by the term $1-\widehat{\beta}\exp(-Pez)$ is vertically stratified owing to the exponential base-state number density field. The leading order z momentum equation is the same as Eq. 4.33 except for a factor of β multiplying the pressure

$$D\left(P_0+\frac{\beta\zeta}{9}N_0\right)=0. \tag{4.118}$$

which has the solution

$$P_0=\frac{\beta\zeta}{9}\left(-N_0+\frac{3}{2}C_2\right), \tag{4.119}$$

The factor of β difference in Eq. 4.118 is due to the fact that pressure here is scaled by the viscous stress rather than the bacterial stress. In Eq. 4.119, $(3/2)C_2$ is the constant of integration with the factor $3/2$ for algebraic simplicity in later manipulations. The solution to Eq. 4.116 which satisfies the no-slip boundary condition at $z=0$ is

$$U_1(z)=\int_0^z\frac{dU_1}{dz'}dz'=\frac{i\beta\zeta}{6}\left[\frac{I_1(z)}{1-\exp(-Pe)}+C_2I_2(z)+C_3I_3(z)\right], \tag{4.120}$$

where C_3 is the second integration constant and the integrals $I_1(z)$, $I_2(z)$, and

$I_3(z)$ are given by

$$
\begin{aligned}
I_1(z) &= \int_0^z \frac{\exp(-Pez')dz'}{1-\widehat{\beta}\exp(-Pez')} \\
&= \frac{1}{Pe\widehat{\beta}}\ln\left[\frac{1-\widehat{\beta}\exp(-Pez)}{1-\widehat{\beta}}\right], \qquad (4.121a) \\
I_2(z) &= \int_0^z \frac{z'dz'}{1-\widehat{\beta}\exp(-Pez')} \\
&= \frac{1}{Pe^2}\Bigg\{\frac{Pe^2z^2}{2} + \ln(\widehat{\beta})\ln\left[\frac{1-\widehat{\beta}\exp(-Pez)}{1-\widehat{\beta}}\right] \\
&\quad + dilog\left[\widehat{\beta}\exp(-Pez)\right] - dilog(\widehat{\beta})\Bigg\}, \qquad (4.121b) \\
I_3(z) &= \int_0^z \frac{dz'}{1-\widehat{\beta}\exp(-Pez')} \\
&= z + \frac{1}{Pe}\ln\left[\frac{1-\widehat{\beta}\exp(-Pez)}{1-\widehat{\beta}}\right], \qquad (4.121c)
\end{aligned}
$$

where the dilogarithmic function is defined as $dilog(x) = -\int_1^x \frac{\ln(t)}{t-1}dt$ (Abramowitz & Stegun, 1972). The constants C_2 and C_3 are then determined from the boundary condition on the top wall, $U_1(1) = 0$ and the no-net fluid flux constraint $\langle U_1 \rangle = 0$. Their expressions are too cumbersome to be reproduced here. Now averaging the number density equation Eq. 4.115a in the z-direction yields the $O(k^2)$ growth rate as

$$\sigma_2 = -(1 + 3i\widehat{H}\langle U_1 n_0 \rangle) \qquad (4.122)$$

The neutral curve given by the condition $\sigma_2 = 0$ is no longer simply described by β and Pe as in §4.4 owing to the presence of the non-dimensional number $\widehat{\beta}$ in the expression for the velocity in Eq. 4.120. The definition of $\widehat{\beta}$ in Eq. 4.117 shows that for a given Pe, the latter is fixed by a scaled bacteria concentration γ that does not involve the suspension depth. This is unlike the case without shear rotation in §4.4 in which bacterial concentration influences the

problem only through the depth-dependent scaled concentration β. Since both concentrations β and $\widehat{\beta}$, one being dependent on the suspension depth while the other not, influence the velocity field in Eq. 4.120 it is useful to separate the effects of bacteria concentration from those of the suspension depth. Moreover, the effect of chemotaxis can be described by ζ and thus all the three effects can be studied independently of each other if we describe the problem in terms of ζ, $\widehat{H}$, and γ. Physically this is a consequence of the fact that the effective viscosity is dependent only on the local bacterial concentration. A direct comparison with the case without shear rotation in §4.4 is still possible by making use of the relationship $\beta = (15/8)\gamma\widehat{H}$.

The well-posedness of Eq. 4.116 for the fluid velocity perturbation requires the effective viscosity $1 - (\gamma Pe \exp(-Pez)/[1 - \exp(-Pe)])$ to be positive everywhere in the domain $z\epsilon[0, 1]$. This leads to an upper bound for γ of

$$\gamma_{max} = \frac{1 - \exp(-Pe)}{Pe}. \tag{4.123}$$

Thus, our analysis yields a prediction of a chemotaxis driven instability only when there exists a critical concentration $\gamma < \gamma_{max}$ for which the growth rate is zero. If such a critical concentration does not exist then the suspension is destabilized by the orientation shear instability mechanism when $\gamma = \gamma_{max}$. Otherwise, the chemotaxis driven instability mechanism helps reduce the critical concentration below that for the pure orientation shear instability. The advantage of using γ instead of β to describe the critical condition is apparent now since in the absence of any chemotaxis ($\zeta = 0$) we recover the critical condition for the orientation shear instability $\gamma_{crit} = \gamma_{max} = 1$ obtained previously by Subramanian & Koch (2009).

Results of our calculations depicted in Fig. 4.14 show that a critical bacteria

concentration γ_{crit} that is smaller than the value for the shear rotation instability γ_{max} is indeed predicted. In Fig. 4.14(a) we present the variation of γ_{crit} obtained from the treatments with and without shear rotation with the non-dimensional suspension depth $\widehat{H}$ at $\zeta = 0.1$. For small $\widehat{H}$ the critical concentration is determined by the orientation shear mechanism as indicated by the merging of the γ_{crit} and γ_{max} curves. When $\widehat{H}$ is above a value $\widehat{H}_{min}$ shown by a circle in 4.14(a), the number density instability mechanism significantly reduces the critical concentration from the orientation shear value γ_{max}. We choose to put the circle where γ_{crit} is smaller than γ_{max} by around 10%. The influence of the number density instability mechanism continues to increase with increasing in $\widehat{H}$. The transition between the shear-driven instability and the chemotaxis instability is more or less complete at a value $\widehat{H} = \widehat{H}_{max}$. Beyond this value shear rotation plays little role in the instability as noted by the fact that, at $\widehat{H}_{max}$, γ_{crit} is 90% of the value of γ_{crit} without shear rotation. The effect of chemotaxis on the critical concentration is shown in Fig. 4.14(b). In the absence of any chemotaxis for which $\zeta = 0$ the suspension is destabilized purely by the orientation shear mechanism if $\gamma > \gamma_{crit} = 1$ (Subramanian & Koch, 2009). For a given $\widehat{H}$ increasing the strength of chemotaxis by increasing ζ decreases not just γ_{crit} but also the range of $\widehat{H}$ in which shear rotation has an influence. The latter point is seen in Fig.4.14(c).

Although shear rotation does not play a significant role in determining the critical concentration for deep channels as seen in Fig.4.14(a), it has a strong destabilizing effect when γ is sufficiently larger than γ_{crit}. To elucidate this we study the variation of the growth rate with the concentration in Fig. 4.14(d) at a suspension depth $\widehat{H} = 150$ and $\zeta = 0.1$ for which the effect of shear rotation on the critical condition is negligible as seen in Fig. 4.14(a). In Fig. 4.14(d) when γ

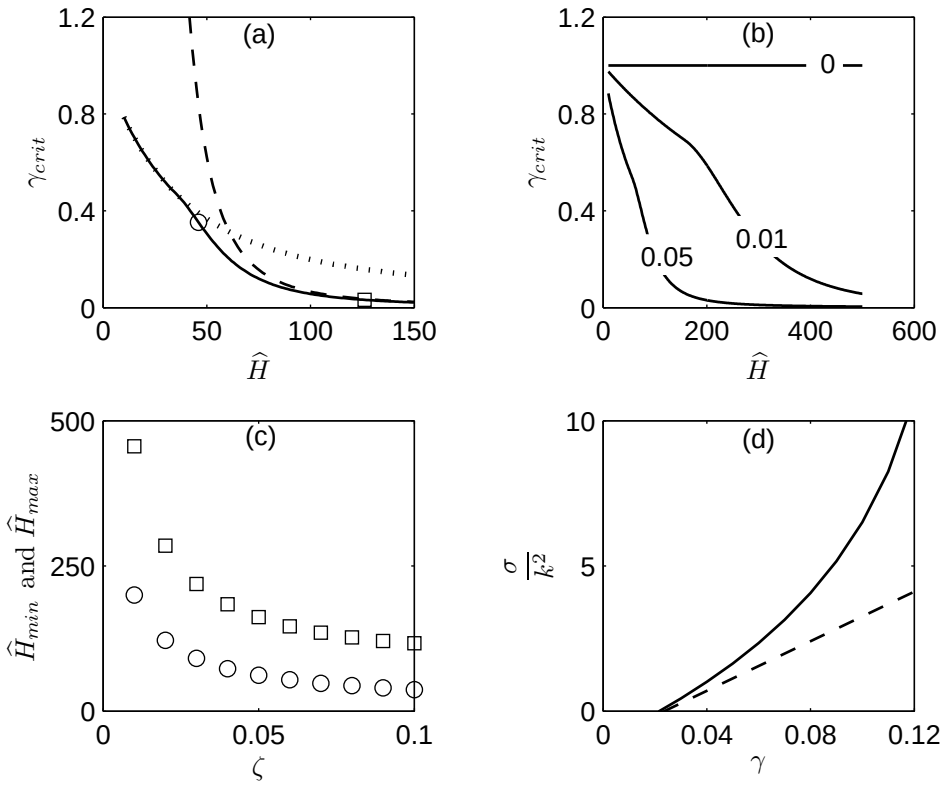

Figure 4.14: (a) Variation of the critical concentration γ_{crit} (solid line) with suspension depth $\widehat{H}$ at $\zeta = 0.1$. For comparison variation of γ_{crit} for the case without shear rotation (obtained from §4.4) and the critical concentration for the purely orientational instability γ_{max} are also shown by a dashed line and a dotted line respectively. The circle indicates the point at which γ_{crit} is 90% of γ_{max} and the square when γ_{crit} is 90% of γ_{crit} obtained for the case without shear rotation. We denote the values of $\widehat{H}$ at these points as $\widehat{H}_{min}$ and $\widehat{H}_{max}$ respectively. (b) γ_{crit} versus $\widehat{H}$ for various values of ζ with symbols defined as in (a). (c) Variation of $\widehat{H}_{min}$ (circles) and $\widehat{H}_{max}$ (squares) with ζ. (d) Normalized growth rate σ/k^2 versus concentration γ for the case with shear rotation (solid line) and without shear rotation (broken line) at $\zeta = 0.1$ and $\widehat{H} = 150$.

is close to γ_{crit} (the horizontal intercept) growth rates predicted by theories with and without shear rotation do not differ appreciably from each other. However, the presence of shear rotation causes a sharper increase in the growth rate thereafter. The reduction in the effective viscosity due to shear rotation enables the chemical gradient induced active stresses to drive a larger fluid velocity disturbance leading to a faster growth of the number density variation. The destabilizing role of shear rotation is further evidenced by the fact that the value of γ_{crit} obtained from the calculation that includes shear rotation is always smaller than the γ_{crit} predicted by the theory without shear rotation. However, as seen in Fig. 4.14(a) this difference is only infinitesimal for large enough suspension depth since the reduction in viscosity happens only within a thin boundary layer near $z = 0$.

4.8 Concluding Discussion

In the preceding sections we have demonstrated the existence of a new instability mechanism in bacterial suspensions driven by chemotaxis. The balance of chemotaxis and diffusion leads to a non-uniform base-state bacteria concentration field and active stress field. The coupling between fluid flow and bacteria concentration field through the swimming induced active stress and convection of bacteria leads to an instability of the aforementioned base-state when the scaled bacteria concentration β exceeds a critical value dictated by the Peclet number Pe measuring the strength of chemotaxis relative to diffusion. The critical concentration for the instability β_{crit} is set by the modes of the largest wavelength and $\beta_{crit} \sim Pe^{-3}$ for $Pe \ll 1$ while $\beta_{crit} \sim 2$ for $Pe \gg 1$ in the case with both boundaries being no-slip walls. If the boundary closer to the region

of larger concentration of the chemical attractant is a shear stress free interface, the large Pe asymptote changes to $\beta_{crit} \sim 4/Pe$. An analysis of semi-infinite suspensions has revealed the existence of a most dangerous wavenumber of the instability for which the growth rate is maximum and a cut-off wavenumber above which the disturbances cease to grow. From the full numerical solution of suspensions of finite depth, these wavenumbers have been found to scale with the Peclet number indicating the fact that the most dangerous and cut-off wavelength are of the order as the boundary layer thickness κ/U_0 when Pe is large. While the instability is stationary in the limit of small wavenumbers, the numerical solution shows the presence of oscillatory solutions for wavenumbers of $O(Pe)$ and for $\beta > 247$. Further analysis however has shown that the most dangerous mode is always stationary. A long wavelength analysis that includes the rotation of bacteria by fluid velocity gradients shows that the critical concentration of shallow suspensions is set by the orientation shear instability mechanism and the latter has only negligible influence in determining the critical concentration of deeper suspensions. Nevertheless, the growth rates of the instability in the super-critical regime is strongly enhanced by shear rotation.

While controlled experiments for validating our predictions are yet to be done, we believe that the present mechanism of instability operated in the experiments of Sokolov *et al.* (2009). The observation of cross film convective patterns in liquid films containing oxytactic *B. Subtilis* cells when the film thickness is raised above 200 μm suggests this. We note that the fundamental requirement for the present active stress instability, namely the inhomogeneous bacterial concentration field, is fulfilled in Sokolov *et al.*'s (2009) experiments at sufficiently large film thicknesses owing to the chemotactic accumulation of bacteria near the interfaces. The spatially homogeneous, in plane collective motion that

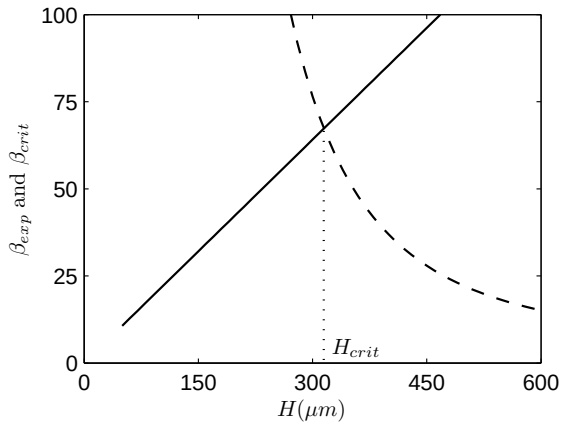

Figure 4.15: Variation of the value of β obtained in Sokolov *et al.*'s (2009) experiment β_{exp} (solid line) and the β_{crit} (broken line) required for instability with the thickness of the film. The instability persists when $H \geq H_{crit} \approx 310\mu m$.

the authors observe for thinner films is presumably due to the orientation shear instability. When the film thickness becomes sufficiently large, the spatially inhomogeneous active stress instability takes over and one starts to see cross-film convective patterns. Furthermore, our estimate of the critical film thickness for the onset of the present instability compares well with the experimental observation of Sokolov *et al.* (2009). To show this, we plot β_{exp}, the value of β reached in their experiment and the theoretical β_{crit} required for instability (Eq. 4.40) versus the film thickness in Fig. 4.15. The mean bacterial concentration $\langle n_0 \rangle$ used for calculating β_{exp} taken from Sokolov *et al.* (2009) is 2 $\times 10^{10}$ per milliliter. The swimming velocity and the mean tumbling frequency used in the calculations are the typical values 20 $\mu m/s$ and 1 s^{-1} respectively, along with the typical ratio 0.1 of the chemotactic velocity to the swimming speed. Here we use the half film thickness $H/2$ for all calculations since the gradient in Sokolov *et al.* (2009)'s

experiment is from the mid-plane of the film to the interfaces. The chemotaxis driven instability described here persists when $\beta_{exp} \geq \beta_{crit}$ which happens when $H \geq H_{crit} \approx 310\mu m$. The determination of a critical film thickness in an experiment is not entirely straightforward. Sokolov *et al.* (2009) reported the size of the largest region in which they observed number density inhomogeneities as a function of the film thickness and reported a critical thickness of $200\mu m$ as minimum film thickness at which any inhomogeneity could be observed. However, if we take the critical film thickness by extrapolating the plot of inhomogeneity size versus film thickness to zero inhomogeneity size assuming a simple linear or quadratic dependence we obtain a critical film thickness of about $290\mu m$. In either case the observed critical thickness is near the theoretical prediction but the latter method which requires a significant inhomogeneity to constitute an unstable film yields a critical thickness that is quite close to the theoretical prediction of 310μm in Fig. 4.15. This agreement is excellent considering the fact that the actual chemotactic velocity in the experiment is not known. Moreover, the Pe based on the half-film thickness for those film thicknesses above which the cross-film convective motions persists in Sokolov *et al.* (2009)'s experiment is of $O(1)$ which means that the most dangerous mode scales with the film thickness as seen in §4.6. This seems to agree with the map of bacterial number density given in Fig. 4a of Sokolov *et al.* (2009). These observations strongly suggest the existence of the new instability mechanism discussed here in their experiments.

Since the attractant gradient generated by the consumption of the attractant by bacteria in the experiment of Sokolov *et al.* (2009) is relatively uncontrollable, artificially imposing controlled chemical gradients on a bacterial suspension will create a better experiment to test our theory. A simple arrangement

to generate static chemical gradients for chemotaxis studies using microfluidic techniques has been described by Cheng *et al.* (2007). A specific application of this device for the quantitative study of bacterial chemotaxis was conducted by Kalinin *et al.* (2009). Their device consists of three microchannels carved out of an agarose gel with the center channel sealed at two ends containing the bacterial suspension. A solution containing the chemo-attractant flows through one of the side channels and a buffer solution through the other side channel. The attractant gradient is then produced by the diffusion of the attractant from the source channel to the sink channel across the agarose gel and the center channel. Precise control over the gradient can be achieved by adjusting the concentration of attractant in the source channel and the gradient of an attractant such as Me-Asp (α-methyl-DL-aspartate) (Adler, 1966) which is not consumed is not influenced by the presence of bacteria and can be maintained stationary for long times (Cheng *et al.*, 2007; Kalinin *et al.*, 2009). This method of gradient generation is superior to the method which involves co-flowing streams of bacteria and attractant described by Kim & Breuer (2007) since the shear in micro-channels disturbs bacterial orientation by aligning them along the streamlines rather than the chemical gradient.

We now discuss the results presented in the previous sections in the context of the previous literature on instabilities in bacterial suspensions. First, we wish to distinguish between the present mechanism of instability and bio-convection even though both arise from a non-uniform base state and both result in similar convection patterns. While the physical mechanism behind bio-convection involves the stratification of the effective density of the fluid (Childress *et al.*, 1975; Pedley & Kessler, 1992; Hillesdon & Pedley, 1996), the present mechanism is due to the stratification of the active stress field. This fundamental difference

in the physical mechanisms results in different length scale requirements for these instabilities. Active stress driven instabilities can give rise to bulk motion (Koch & Subramanian, 2011) in much thinner films where bio-convection cannot operate. In addition, while the active stress instability described here exists only for suspensions of pushers such *E. Coli*, bio-convection can occur whether the organism is a pusher or puller. For instance bio-convection has been observed in suspensions of the alga *C. Nivalis* which is a puller (Pedley & Kessler, 1992). It is also interesting to note that at the linear order and with constant chemotaxis velocities, bio-convection without gyrotaxis is a purely stationary instability (Childress *et al.*, 1975) while the active stress driven instability described here shows oscillatory modes for certain parameter values as shown in §4.6.

It is also important to note that the present mechanism of instability is entirely different from the previously analyzed active stress instabilities in homogeneous suspensions of swimming rods (Simha & Ramaswamy, 2002; Saintillan & Shelley, 2008*a*,*b*; Hohenegger & Shelley, 2010) or run-tumble bacteria (Koch & Subramanian, 2011; Subramanian & Koch, 2009; Subramanian *et al.*, 2011). The difference lies in whether the fluid flow couples to the bacterial number density field as in the present case or to the orientation field as in the latter. The hallmark of the present instability mechanism is the existence of unstable number density fluctuations at all wavelengths which is in sharp contrast with the previously analyzed cases. The existence of unstable density fluctuations at the linear order depends upon the symmetry of the base-state orientation field of the bacteria (Subramanian & Koch, 2009). If the base-state orientation field is symmetric, as in the case of isotropic suspensions, density fluctuations do not arise at the linear order at any wavelength (Saintillan & Shelley, 2008*a*,*b*; Subra-

manian & Koch, 2009; Hohenegger & Shelley, 2010). On the other hand, if the $\boldsymbol{p} \rightarrow -\boldsymbol{p}$ symmetry of the base-state orientation field is broken due to a chemical gradient, unstable density fluctuations in general arise at the linear order (Subramanian & Koch, 2009) for aligned suspensions of self-propelled rods without chemotaxis (Saintillan & Shelley, 2008*a*,*b*) or suspensions of chemotactic bacteria (Subramanian *et al.*, 2011). However, in both cases if the wavelength of the disturbance is much larger than $(nL^2)^{-1}$, it seen that the leading order problem involves only orientational fluctuations and the amplitude of density fluctuations is $O(k)$ (non-dimensionalized by nL^2) smaller than that of orientational fluctuations (see Eqs. 35 and 36 in Saintillan & Shelley (2008*a*,*b*) and Eq. 57 in Subramanian *et al.* (2011)). It is the homogeneous base-state number density field that prevented the growth of number density fluctuations at long wavelengths in these cases. In contrast to this, the instability mechanism analyzed here relies on an inhomogeneous number density field in the base-state and the flow driven by bacterial concentration fluctuations at *all* wavelengths including the longest wavelength mode which determines the critical concentration. A spatially non-uniform base state causes the number density instability to choose a length scale comparable to the length scale over which the bacteria concentration varies in the base state while orientation shear instability does not have a preferred length scale (Subramanian *et al.*, 2011). Furthermore, as seen in Fig. 4.14(a) for suspensions of sufficient depth, the critical concentration is not only determined by the present mechanism but it is significantly smaller that what required for the orientation shear instability. For instance, at a suspension depth of $\widehat{H} = 150$ in Fig. 4.14(a) γ_{crit} is smaller than γ_{max} by a factor of approximately six.

The existence of the chemotaxis-induced-instability presented in this paper

and in Kasyap & Koch (2012) has been confirmed by Ezhilan *et al.* (2012) through full nonlinear simulations of the kinetic equation for $\Omega(\boldsymbol{x}, \boldsymbol{p}, t)$. The primary objective of this paper is the investigation of the dynamics of suspensions of aerotactic bacteria under the experimental setting of Sokolov *et al.* (2009). Thus the suspension is confined in a cubical domain with periodic boundary conditions in two directions and zero-shear-stress boundary condition in the third direction and the latter boundaries are kept at constant oxygen concentration. The oxygen gradient is formed due to the consumption by bacteria and in addition to the bacterial consumption, the oxygen concentration evolves in time due to fluid convection and diffusive transport. Ezhilan *et al.* (2012) varied the thickness of the film in the third direction to mimic the experiment of Sokolov *et al.* (2009) and observed three principal regimes of suspension behavior. For film thicknesses less than $200\mu m$ (classified as "regime I" in Ezhilan *et al.* (2012)) the bacterial and the oxygen concentration profiles reached a steady state. Gross fluctuations in the bacteria concentration field and the fluid velocity field started to appear in "regime II" which spans the film thicknesses between $200\mu m$ and $400\mu m$. Further increase in the film thickness beyond $400\mu m$ (region III) resulted in an oxygen depletion layer along with the intensification in the magnitude of fluctuations closer to the film edges and attenuate the magnitude near the center.

Ezhilan *et al.* (2012) point out that in regime I in which no unsteady motion was observed, the oxygen concentration was uniform across the film so that the chemotaxis of bacteria was too weak for any fluctuations to grow. The latter started growing and eventually reached a level of saturation in regime II which had sufficient thickness to create a strong oxygen gradient. A typical observation in this regime was strong chemotactic concentration of bacteria near the

boundaries and plumes dense in bacteria originating from those boundaries to the bulk. This is consistent with the pattern of motion predicted by our theory and in addition, Ezhilan *et al.* (2012) report a general agreement on the critical conditions for the onset of the unsteady motion with our predictions in Kasyap & Koch (2012). An important insight based on this agreement is that the two approaches for analyzing the stability of bacterial suspensions viz. solving an equation for the number density as we do and solving the full kinetic equation for the position-orientation probability density in Ezhilan *et al.* (2012) are equivalent. However, the former will be considerably simpler especially for non-linear simulations since one does not have to solve for the orientational degrees of freedom and in this regard the continuum equations derived in §4.7.1 are valuable.

4.9 Appendix A: Justification for neglecting the attractant transport by fluid flow

In §4.3 we neglected the attractant transport by the fluid flow generated by instability since attractant diffusivity is typically much larger than bacteria diffusivity. We now provide a justification for this assumption by first writing down the non-dimensional attractant transport equation

$$\frac{\partial C_a}{\partial t} + Pe\nabla \cdot (\boldsymbol{u}C_a) - \frac{\kappa_a}{\kappa}\nabla^2 C_a = 0 \tag{4.124}$$

in which length, time, and velocity have been scaled by the channel depth H, the bacterial diffusion time H^2/κ, and the chemotactic velocity U_0 respectively as followed for deriving the non-dimensional bacteria transport equation Eq. 4.27a. For typical attractants like Me-Asp or oxygen, the diffusivity κ_a is of the

order of $10^3 \mu m^2/s$ (see Sartori & Tu (2011) and Ferrell & Himmelblau (1967)) while a typical bacterium swimming at a speed of $20 \mu m/s$ and tumbling at a rate of $1 s^{-1}$ is $\kappa \approx 133 \mu m^2/s$ which is an order magnitude smaller than the attractant diffusivity so that $\kappa_a/\kappa \gg 1$. Thus when $Pe = O(1)$, the transport of the attractant by fluid flow along with the unsteady term in Eq. 4.124 can be neglected. Even when $Pe \gg 1$ the diffusion term dominates since the fluid velocity is only $O(Pe^{-1})$ at most (see §4.5.3). A comparison of oxygen concentration profiles from nonlinear simulations of Ezhilan *et al.* (2012) also indicate that the instability generated fluid flow causes little perturbation to oxygen concentration field.

4.10 Appendix B: Matching the outer and inner solutions in $Pe \gg 1$ analysis

In this appendix, we give the details of the matching procedure followed for solving the fluid velocity field in §4.5.1 and 4.5.2.

4.10.1 Case I: no-slip boundary conditions at $z = 0$ and $z = 1$

The solutions of Eqs. 4.57 and 4.62 are

$$\overline{W_3} = \beta k^2 [\bar{z} + \exp(-\bar{z}) - 1] + a_3 \bar{z}^3 + b_3 \bar{z}^2, \tag{4.125a}$$

$$\overline{W}_4 = a_4 \bar{z}^3 + b_4 \bar{z}^2 \tag{4.125b}$$

The required matching condition written in terms of the inner variable $\bar{z}$ is

$$\lim_{Pe^{-1}\bar{z} \to 0} \widehat{W}(Pe^{-1}\bar{z}) = \lim_{\bar{z} \to \infty} \overline{W}(\bar{z}). \tag{4.126}$$

in which $\overline{W} = Pe^{-3}\overline{W}_3 + Pe^{-4}\overline{W}_4$ and $\widehat{W}$ is given by Eq. 4.45. Matching done by equating the coefficients of powers of $\bar{z}$ at respective orders yields the following up to $O(Pe^{-4})$

$$\text{At } O(1) \quad A_0(k\cosh k - \sinh k) + B_0 \sinh k = 0, \tag{4.127a}$$

$$\text{At } O(Pe^{-1}) \quad A_1(k\cosh k - \sinh k) + B_1 \sinh k = 0, \tag{4.127b}$$

$$A_0 k^2 \sinh k + B_0(k\cosh k + \sinh k) = 0, \tag{4.127c}$$

$$\text{At } O(Pe^{-2}) \quad A_2(k\cosh k - \sinh k) + B_2 \sinh k = 0, \tag{4.127d}$$

$$A_1 k^2 \sinh k + B_1(k\cosh k + \sinh k) = 0, \tag{4.127e}$$

$$\text{At } O(Pe^{-3}) \; A_2 k^2 \sinh k + B_2(k\cosh k + \sinh k) = -\beta k^2, \tag{4.127f}$$

$$A_1 \frac{k^2}{2}(\sinh k + k\cosh k) + B_1 \left(k\cosh k + \frac{k^2}{2}\sinh k\right) = b_3, \tag{4.127g}$$

$$A_0 \left(\frac{k^2}{6}\sinh k + \frac{k}{3}\cosh k\right) + B_0 \left(\frac{1}{2}\sinh k + \frac{k}{6}\cosh k\right) = -\frac{a_3}{k^2}, \tag{4.127h}$$

$$\text{At } O(Pe^{-4}) \; A_2 \frac{k^2}{2}(\sinh k + k\cosh k) + B_2 \left(k\cosh k + \frac{k^2}{2}\sinh k\right) = b_4, \tag{4.127i}$$

$$A_1 \left(\frac{k^2}{6}\sinh k + \frac{k}{3}\cosh k\right) + B_1 \left(\frac{1}{2}\sinh k + \frac{k}{6}\cosh k\right) = -\frac{a_4}{k^2}. \tag{4.127j}$$

Solving Eqs. 4.127a and 4.127c gives $A_0 = B_0 = 0$ and using this in Eq. 4.127h we get $a_3 = 0$. Similarly, Eqs. 4.127b and 4.127e yield $A_1 = B_1 = 0$ which in turn gives $b_3 = a_4 = 0$ from Eqs. 4.127g and 4.127j respectively. Finally Eqs. 4.127d and 4.127f yield

$$A_2 = \frac{\beta k^2 \sinh k}{k^2 - \sinh^2 k}, \tag{4.128a}$$

$$B_2 = -\frac{\beta k^2(k\cosh k - \sinh k)}{k^2 - \sinh^2 k}. \tag{4.128b}$$

Equation 4.127i then gives $b_4 = -\frac{\beta k^3(k - \sinh k \cosh k)}{k^2 - \sinh^2 k}$.

4.10.2 Case II: no-slip boundary condition at $z = 1$ and zero shear stress boundary condition at $z = 0$

Equations 4.70 and 4.71 yields the solutions

$$\overline{W}_2 = a_2\bar{z}^3 + c_2\bar{z}, \tag{4.129a}$$

$$\overline{W}_3 = \beta k^2\left[\exp(-\bar{z}) - \frac{\bar{z}^2}{2} - 1\right] + a_3\bar{z}^3 + c_3\bar{z}. \tag{4.129b}$$

The matching procedure used in case II gives the same relationships as in Eq. 4.127 up to $O(Pe^{-1})$ (Eq. 4.127c) so that $A_0 = B_0 = 0$ as before and the remaining relationships are

$$\text{At } O(Pe^{-2}) \quad A_2(k\cosh k - \sinh k) + B_2\sinh k = 0, \tag{4.130a}$$

$$A_1k^2\sinh k + B_1(k\cosh k + \sinh k) = -c_2, \tag{4.130b}$$

$$A_0\frac{k^2}{2}(\sinh k + k\cosh k) + B_0\left(k\cosh k + \frac{k^2}{2}\sinh k\right) = 0, \tag{4.130c}$$

$$a_2 = 0, \tag{4.130d}$$

$$\text{At } O(Pe^{-3}) \quad A_3(k\cosh k - \sinh k) + B_3\sinh k = -\beta k^2, \tag{4.130e}$$

$$A_2k^2\sinh k + B_2(k\cosh k + \sinh k) = -c_3, \tag{4.130f}$$

$$A_1\frac{k^2}{2}(\sinh k + k\cosh k) + B_1\left(k\cosh k + \frac{k^2}{2}\sinh k\right) = -\frac{\beta k^2}{2}, \tag{4.130g}$$

along with Eq. 4.127h which gives $a_3 = 0$. Equations 4.127b and 4.130g give

$$A_1 = \frac{\beta k\sinh k}{2(k - \sinh k\cosh k)}, \tag{4.131a}$$

$$B_1 = \frac{\beta k(\sinh k - k\cosh k)}{2(k - \sinh k\cosh k)}, \tag{4.131b}$$

which in turn yields from Eq. 4.130b

$$c_2 = \frac{\beta k(k^2 - \sinh^2 k)}{2(k - \sinh k\cosh k)}. \tag{4.132}$$

and using Eq. 4.132 in the solvability condition Eq. 4.73 yields $\sigma_{-1} = c_2$. Now to determine c_3 using Eq. 4.130f we need to obtain A_2 and B_2 first. Unfortunately, at present we have only Eq. 4.130a that involves A_2 and B_2 and to obtain one more relationship between them, we need to do the matching of the $O(Pe^{-4})$ velocity field governed by

$$\overline{D}^4\overline{W}_4 = 2k^2\overline{D}^2\overline{W}_2 - \beta k^2\overline{DN}_1, \tag{4.133a}$$

$$\overline{W}_4 = \overline{D}^2\overline{W}_4 = 0 \quad \text{at } \bar{z} = 0, \tag{4.133b}$$

in which $\overline{N}_1$ is the solution of

$$(\overline{D}^2 + \overline{D})\overline{N}_1 = \sigma_{-1}\overline{N}_0 - \overline{W}_2 \exp(-\bar{z}), \tag{4.134a}$$

$$(1 + \overline{D})\overline{N}_1 = 0 \quad \text{at } \bar{z} = 0, \tag{4.134b}$$

$$\lim_{\bar{z}\to\infty} \overline{N}_1(\bar{z}) = 0. \tag{4.134c}$$

along with the normalization $\int_0^\infty \overline{N}_1(\bar{z})d\bar{z} = 0$. Using the form of σ_{-1} determined above and the form of $\overline{W}_2$ in Eq. 4.72a we obtain

$$\overline{N}_1 = c_2 \left(\frac{\bar{z}^2}{2} - 1\right) \exp(-\bar{z}). \tag{4.135}$$

in which c_2 is given by Eq. 4.132. Equation 4.135 in Eq. 4.133 then gives

$$\overline{W}_4 = \frac{\beta^2 k^2}{2} \left[c_2 \exp(-\bar{z})(6\bar{z} + \bar{z}^2 + 10) + a_4\bar{z}^3 + c_4\bar{z} - 10c_2\right]. \tag{4.136}$$

In Eq. 4.136 the $\bar{z}^2 \exp(-\bar{z})$ term vanishes in the matching limit of $\bar{z} \to \infty$ so that equating the coefficient of $\bar{z}^2$ in the $O(Pe^{-4})$ outer solution of the z-velocity field Eq. 4.45 to zero yields one more relationship between A_2 and B_2 as

$$A_2\frac{k^2}{2}(\sinh k + k\cosh k) + B_2\left(k\cosh k + \frac{k^2}{2}\sinh k\right) = 0. \tag{4.137}$$

Finally, Eqs. 4.130a and 4.137 gives $A_2 = B_2 = 0$ so that we have $c_3 = 0$ from Eq. 4.130f.

4.11 Appendix C: Series expansion for $W(z)$

$W(z)$ is given by the fourth order ODE

$$\left(D^2 - k^2\right)^2 W(z) = -\beta k^2 \sum_{j=0}^{M} a_j \phi_j(z). \tag{4.138}$$

$$W = DW = 0 \quad \text{at } z = 0, z = 1 \tag{4.139}$$

Solving 4.139 yields $W(z) = \sum_{j=0}^{M} a_j \psi_j(z)$ where

$$\psi_j(z) = -\beta k^2 \left\{ \sum_{i=1}^{4} \left[(\Lambda_{1i} F_{ij} + \Lambda_{2i} F_{ij} z) \sinh kz + (\Lambda_{3i} F_{ij} + \Lambda_{4i} F_{ij} z) \cosh kz \right] + G_j(z) \right\}, \tag{4.140}$$

where $\Lambda_{11} = k + \sinh k \cosh k$, $\Lambda_{12} = k$, $\Lambda_{13} = -(k \cosh k + \sinh k)$, $\Lambda_{14} = \sinh k$, $\Lambda_{21} = k \sinh^2 k$, $\Lambda_{22} = \sinh k \cosh k - k$, $\Lambda_{23} = -k^2 \sinh k$, $\Lambda_{24} = k \cosh k - \sinh k$, $\Lambda_{31} = -1$, $\Lambda_{32} = \Lambda_{33} = \Lambda_{34} = 0$, $\Lambda_{41} = -k(k + \cosh k \sinh k)$, $\Lambda_{42} = -\sinh^2 k$, $\Lambda_{43} = k(k + \cosh k \sinh k)$, and $\Lambda_{44} = -k \sinh k$ and

$$F_{ij} = \frac{Pe \exp(-Pe)}{8k^2} \begin{bmatrix} 0 & 0 & -1 & Pe - 2 \end{bmatrix}^\dagger, \tag{4.141}$$

if $|k| = Pe$ and

$$F_{ij} = \frac{Pe}{\left(Pe^2 - k^2\right)^2} \begin{bmatrix} -1 & Pe & -\exp(-Pe) & Pe \exp(-Pe) \end{bmatrix}^\dagger, \tag{4.142}$$

if $|k| \neq Pe$. For $j \neq 0$

$$F_{ij} = \left[R_2 \quad j\pi R_1 - \frac{PeR_2}{2} \quad (-1)^j R_2 \exp\left(\frac{-Pe}{2}\right) \quad (-1)^j \exp\left(\frac{-Pe}{2}\right) \left(j\pi R_1 - \frac{PeR_2}{2} \right) \right]^\dagger, \tag{4.143}$$

where

$$R_1 = \frac{2\pi j f_2 + \left(\frac{2j^2\pi^2}{Pe} - \frac{Pe}{2} \right) f_1}{f_1^2 + f_2^2},$$

$$R_2 = \frac{2\pi j f_1 - \left(\frac{2j^2\pi^2}{Pe} - \frac{Pe}{2} \right) f_2}{f_1^2 + f_2^2},$$

in which

$$\begin{aligned} f_1 &= \frac{Pe^4}{16} - \frac{3Pe^2j^2\pi^2}{2} + j^4\pi^4 - \frac{Pe^2k^2}{2} + 2k^2j^2\pi^2 + k^4, \\ f_2 &= -\frac{Pe^3j\pi}{2} + 2Pej^3\pi^3 + 2k^2Pej\pi, \end{aligned}$$

Finally for $j = 0$

$$G_0(z) = \begin{cases} -\frac{Pez^2\exp(-Pez)}{8k^2}, & |k| = Pe \\ -\frac{Pe\exp(-Pez)}{(Pe^2-k^2)^2}, & |k| \neq Pe, \end{cases} \tag{4.144}$$

and for $j \neq 0$

$$G_j(z) = \exp\left(\frac{-Pe}{2}\right)\left[R_1\sin(j\pi z) + R_2\cos(j\pi z)\right].$$

Acknowledgement

This work was supported by NSF grant CBET-1066193.

Bibliography

ABRAMOWITZ, M. & STEGUN, I. A. 1972 *Handbook of Mathematical Functions with Formulas, Graphs, and Mathematical Tables. National Bureau of Standards Applied Mathematics Series 55. Tenth Printing..*

ADEROGBA, K. & BLAKE, J.R. 1978 Action of a force near the planar surface between two semi-infinite immiscible liquids at very low reynolds numbers. *Bulletin of the Australian Mathematical Society* **18** (03), 345–356.

ADLER, J. 1966 Effect of amino acids and oxygen on chemotaxis in escherichia coli. *J. Bacteriol.* **92**, 121–129.

AGARWAL, RAMESH K., YUN, KEON-YOUNG & BALAKRISHNAN, RAMESH 2001 Beyond navier–stokes: Burnett equations for flows in the continuum–transition regime. *Physics of Fluids* **13** (10), 3061–3085.

ANGELINI, T. E., ROPER, M., KOLTER, R., WEITZ, D. A. & BRENNER, M. P. 2009 Bacillus subtilis spreads by surfing on waves of surfactant. *Proc. Natl. Acad. Sci.* **106**, 18109–18113.

BEARON, R. & PEDLEY, T. 2000 Modelling run-and-tumble chemotaxis in a shear flow. *Bull. Math. Biol.* **62**, 775–791.

BEARON, R. N. 2003 An extension of generalized taylor dispersion in unbounded homogeneous shear flows to run-and-tumble chemotactic bacteria. *Phys. Fluids* **15**, 1552–1563.

BERG, H. C. 2003 *E. coli in Motion*. Springer Verlag.

BERKE, ALLISON P., TURNER, LINDA, BERG, HOWARD C. & LAUGA, ERIC 2008 Hydrodynamic attraction of swimming microorganisms by surfaces. *Phys. Rev. Lett.* **101**, 038102.

BIRD, R.B., ARMSTRONG, R.C. & HASSAGER, O. 1987 *Dynamics of polymeric liquids. Vol. 1: Fluid mechanics*. John Wiley and Sons Inc., New York, NY.

BLAKE, J. R. 1971 A note on the image system for a stokeslet in a no-slip boundary. *Mathematical Proceedings of the Cambridge Philosophical Society* **70** (02), 303–310.

BOWEN, P.J., DAVIES, A.R. & WALTERS, K. 1991 On viscoelastic effects in swirling flows. *Journal of Non-Newtonian Fluid Mechanics* **38** (23), 113 – 126.

BRENNER, HOWARD 1974 Rheology of a dilute suspension of axisymmetric brownian particles. *International Journal of Multiphase Flow* **1** (2), 195 – 341.

BRENNER, M. P., LEVITOV, L. S. & BUDRENE, E. O. 1998 Physical mechanisms for chemotactic pattern formation by bacteria. *Biophys. J.* **74**, 1677 – 1693.

BUDRENE, E. O. & BERG, H. C. 1991 Complex patterns formed by motile cells of Escherichia coli. *Nature* **349**, 630–633.

BUDRENE, E. O. & BERG, H. C. 1995 Dynamics of formation of symmetrical patterns by chemotactic bacteria. *Nature* **376**, 49–53.

BURGHELEA, TEODOR, SEGRE, ENRICO, BAR-JOSEPH, ISRAEL, GROISMAN, ALEX & STEINBERG, VICTOR 2004 Chaotic flow and efficient mixing in a microchannel with a polymer solution. *Phys. Rev. E* **69**, 066305.

CERCIGNANI, C. 1988 *The Boltzmann equation and its applications*, , vol. 67. Springer.

CHANDRASEKHAR, S. 1961 *Hydrodynamic and hydromagnetic stability*. Dover.

CHEN, K. C., FORD, R. M. & CUMMINGS, P. T. 2003 Cell balance equation for chemotactic bacteria with a biphasic tumbling frequency. *J. Math. Biol.* **47**, 518–546.

CHENG, S. Y., HEILMAN, S., WASSERMAN, M., ARCHER, S., SHULER, M. L. & WU, M. 2007 A hydrogel-based microfluidic device for the studies of directed cell migration. *Lab Chip* **7**, 763–769.

CHILDRESS, S., LEVANDOWSKY, M. & SPIEGEL, E. A. 1975 Pattern formation in a suspension of swimming microorganisms: equations and stability theory. *J. Fluid Mech.* **69**, 591–613.

CISNEROS, LUIS, DOMBROWSKI, CHRISTOPHER, GOLDSTEIN, RAYMOND E. & KESSLER, JOHN O. 2006 Reversal of bacterial locomotion at an obstacle. *Phys. Rev. E* **73**, 030901.

DILUZIO, W.R., TURNER, L., MAYER, M., GARSTECKI, P., WEIBEL, D.B., BERG, H.C. & WHITESIDES, G.M. 2005 Escherichia coli swim on the right-hand side. *Nature* **435** (7046), 1271–1274.

DOMBROWSKI, C., CISNEROS, L., CHATKAEW, S., GOLDSTEIN, R. E. & KESSLER, J. O. 2004 Self-concentration and large-scale coherence in bacterial dynamics. *Phys. Rev. Lett.* **93**, 098103.

EZHILAN, BARATH, PAHLAVAN, AMIR ALIZADEH & SAINTILLAN, DAVID 2012 Chaotic dynamics and oxygen transport in thin films of aerotactic bacteria. *Physics of Fluids* **24** (9), 091701.

FAN, Y., TANNER, R.I. & PHAN-THIEN, N. 2001 Fully developed viscous and viscoelastic flows in curved pipes. *Journal of Fluid Mechanics* **440**, 327–357.

FERRELL, RALPH T. & HIMMELBLAU, DAVID M. 1967 Diffusion coefficients of nitrogen and oxygen in water. *Journal of Chemical & Engineering Data* **12** (1), 111–115.

HERNANDEZ-ORTIZ, J. P., STOLTZ, C. G. & GRAHAM, M. D. 2005 Transport and collective dynamics in suspensions of confined swimming particles. *Phys. Rev. Lett.* **95**, 204501.

HILL, N. A., PEDLEY, T. J. & KESSLER, J. O. 1989 Growth of bioconvection patterns in a suspension of gyrotactic micro-organisms in a layer of finite depth. *J. Fluid Mech.* **208**, 509–543.

HILLESDON, A. J. & PEDLEY, T. J. 1996 Bioconvection in suspensions of oxytactic bacteria: linear theory. *J. Fluid Mech.* **324**, 223–259.

HO, B. P. & LEAL, L. G. 1976 Migration of rigid spheres in a two-dimensional unidirectional shear flow of a second-order fluid. *Journal of Fluid Mechanics* **76**, 783–799.

HOHENEGGER, C. & SHELLEY, M. J. 2010 Stability of active suspensions. *Phys. Rev. E* **81**, 046311.

JÁNOSI, I. M., KESSLER, J. O. & HORVÁTH, V. K. 1998 Onset of bioconvection in suspensions of bacillus subtilis. *Phys. Rev. E* **58**, 4793–4800.

JOO, YONG LAK & SHAQFEH, ERIC S. G. 1991 Viscoelastic poiseuille flow through a curved channel: A new elastic instability. *Physics of Fluids A: Fluid Dynamics* **3** (7), 1691–1694.

KALININ, Y. V., JIANG, L., TU, Y. & WU, W. 2009 Logarithmic sensing in escherichia coli bacterial chemotaxis. *Biophys. J.* **96**, 2439 – 2448.

KASYAP, T. V. & KOCH, DONALD L. 2012 Chemotaxis driven instability of a confined bacterial suspension. *Phys. Rev. Lett.* **108**, 038101.

KELLER, E. F. & SEGEL, L. A. 1971 Model for chemotaxis. *J. Theor. Biol.* **30**, 225–234.

KIM, M. J. & BREUER, K. S. 2004 Enhanced diffusion due to motile bacteria. *Phys. Fluids* **16**, L78–L81.

KIM, M. J. & BREUER, K. S. 2007 Controlled mixing in microfluidic systems using bacterial chemotaxis. *Anal. Chem.* **79**, 955–959.

KIM, S. & KARRILA, S.J. 1991 *Microhydrodynamics*. Butterworth-Heinemann New York.

KOCH, D. L. & SUBRAMANIAN, G. 2011 Collective hydrodynamics of swimming microorganisms: Living fluids. *Ann. Rev. Fluid Mech.* **43**, 637–659.

LARSON, R. G., SHAQFEH, ERIC S. G. & MULLER, S. J. 1990 A purely elastic instability in taylorcouette flow. *Journal of Fluid Mechanics* **218**, 573–600.

LAUGA, ERIC, DILUZIO, WILLOW R., WHITESIDES, GEORGE M. & STONE, HOWARD A. 2006 Swimming in circles: Motion of bacteria near solid boundaries. *Biophysical Journal* **90** (2), 400 – 412.

LAUGA, E. & POWERS, T. R. 2009 The hydrodynamics of swimming microorganisms. *Rep. Prog. Phys.* **72**, 096601.

LEE, CJ 1994 Unique determination of solutions to the burnett equations. *AIAA J.* **32**, 985–990.

LI, GUANGLAI & TANG, JAY X. 2009 Accumulation of microswimmers near a surface mediated by collision and rotational brownian motion. *Phys. Rev. Lett.* **103**, 078101.

MENDELSON, N. H., BOURQUE, A., WILKENING, K., ANDERSON, K. R. & WATKINS, J. C. 1999 Organized Cell Swimming Motions in Bacillus subtilis Colonies: Patterns of Short-Lived Whirls and Jets. *J. Bacteriol.* **181**, 600–609.

MESIBOV, R. & ADLER, J. 1972 Chemotaxis toward amino acids in escherichia coli. *J. Bacteriol.* **112**, 315–326.

PATHAK, JAI A., ROSS, DAVID & MIGLER, KALMAN B. 2004 Elastic flow instability, curved streamlines, and mixing in microfluidic flows. *Physics of Fluids* **16** (11), 4028 – 4034.

PEDLEY, T. J. & KESSLER, J. O. 1992 Hydrodynamic phenomena in suspensions of swimming microorganisms. *Ann. Rev. Fluid Mech.* **24**, 313–358.

PETRIE, CHRISTOPHER J.S. 1999 The rheology of fibre suspensions. *Journal of Non-Newtonian Fluid Mechanics* **87** (23), 369 – 402.

RIVERO, M. A., TRANQUILLO, R. T., BUETTNER, H. M. & LAUFFENBURGER, D. A. 1989 Transport models for chemotactic cell populations based on individual cell behavior. *Chem. Engng. Sci.* **44**, 2881 – 2897.

SAINTILLAN, D. & SHELLEY, M. J. 2007 Orientational order and instabilities in suspensions of self-locomoting rods. *Phys. Rev. Lett.* **99**, 058102.

SAINTILLAN, D. & SHELLEY, M. J. 2008*a* Instabilities and pattern formation in active particle suspensions: Kinetic theory and continuum simulations. *Phys. Rev. Lett.* **100**, 178103.

SAINTILLAN, D. & SHELLEY, M. J. 2008*b* Instabilities, pattern formation, and mixing in active suspensions. *Phys. Fluids* **20**, 123304.

SARTORI, PABLO & TU, YUHAI 2011 Noise filtering strategies in adaptive biochemical signaling networks. *Journal of Statistical Physics* **142** (6), 1206–1217.

SIMHA, R. A. & RAMASWAMY, S. 2002 Hydrodynamic fluctuations and instabilities in ordered suspensions of self-propelled particles. *Phys. Rev. Lett.* **89**, 058101.

SOKOLOV, ANDREY, ARANSON, IGOR S., KESSLER, JOHN O. & GOLDSTEIN, RAYMOND E. 2007 Concentration dependence of the collective dynamics of swimming bacteria. *Phys. Rev. Lett.* **98**, 158102.

SOKOLOV, A., GOLDSTEIN, R. E., FELDCHTEIN, F. I. & ARANSON, I. S. 2009 Enhanced mixing and spatial instability in concentrated bacterial suspensions. *Phys. Rev. E* **80**, 031903.

SUBRAMANIAN, G. & KOCH, D. L. 2009 Critical bacterial concentration for the onset of collective swimming. *J. Fluid Mech.* **632**, 359–400.

SUBRAMANIAN, G., KOCH, D. L. & FITZGIBBON, S. R. 2011 The stability of a homogeneous suspension of chemotactic bacteria. *Phys. Fluids* **23**, 041901.

UNDERHILL, P. T., HERNANDEZ-ORTIZ, J. P. & GRAHAM, M. D. 2008 Diffusion and spatial correlations in suspensions of swimming particles. *Phys. Rev. Lett.* **100**, 248101.

VUPPULA, R. R., TIRUMKUDULU, M. S. & V., VENKATESH K. 2010 Chemotaxis of escherichia coli to l -serine. *Phys. Biol.* **7**, 026007.

WU, X. L. & LIBCHABER, A. 2000 Particle diffusion in a quasi-two-dimensional bacterial bath. *Phys. Rev. Lett.* **84**, 3017–3020.

CHAPTER 5

BACTERIAL COLLECTIVE MOTION NEAR THE CONTACT LINE OF AN EVAPORATING SESSILE DROP

5.1 Abstract

The near-contact-line dynamics of evaporating sessile drops containing live *E. Coli* cells is studied experimentally. The evaporation of the drop drives a radially outward fluid flow inside the drop owing to the pinning of the contact-line and the flow concentrates the suspended bacteria near the contact-line . Our experiments reveal a collective behavior of the concentrated bacterial population near the contact-line appearing in the form of periodic "jets" of bacteria along the circumference of the drop. The observed pattern of jets was very distinct for drops of suspensions of both wild-type and smooth-swimming cells of *E. Coli* and in the case of drops containing incessantly tumbling cells of *E. Coli*, the pattern was much less distinct. A decrease in bacteria concentration was observed to result in a decrease in the width of the region of collective motion. A qualitative reasoning of the problem from the point of view of the linear stability of the continuum equations for the conservation of bacteria and momentum in the suspension suggests the possibility of a concentration instability of the suspension driven by the active stress of swimming bacteria.

5.2 Introduction

Deposition of suspended particles near the pinned contact-line of evaporating drops of particulate suspensions is a ubiquitous observation termed the "coffee ring" effect — a name derived from the appearance of coffee stain which is the archetypal example of this phenomenon (Deegan *et al.*, 1997, 2000; Hu & Larson, 2005). The pinning of the contact-line prevents any change in the contact-line radius of the drop and hence to compensate for the volume of the fluid lost by evaporation, fluid has to be brought toward contact-line from the bulk of the drop thus setting up a radially outward flow. If there are particles suspended in the fluid, the evaporation driven flow brings them towards the contact-line and the particles accumulate there due to the no-flux boundary condition provided by the contact-line. In the present work, we experimentally investigate the near-contact-line dynamics of an evaporating drop containing living bacteria instead of passive particles. This investigation is motivated by the fact that recent experiments on bacterial suspensions have shown the existence of organized motion correlated over length scales much larger than the size of individual bacteria when the bacterial concentration becomes sufficient (see Koch & Subramanian (2011) and references therein). The evaporation driven flow inside a sessile drop provides a natural mechanism to concentrate the bacterial population. It has been suggested that such large scale motions enhance the mixing process in bacteria suspensions (Wu & Libchaber, 2000; Kim & Breuer, 2004; Tuval *et al.*, 2005; Sokolov *et al.*, 2009) resulting in better dispersal of the chemical species vital for bacteria. Furthermore, the sessile drop geometry can be important in the context of bacterial swarming and biofilm formation which often involve bacteria confined within thin liquid films (Bees *et al.*, 2000; Joanny

& Ramaswamy, 2012).

Bacteria such as *E. Coli* are composed of a cell-body propelled in fluids by means of a rotating bundle of helical filaments called flagella and in an isotropic environment bacteria perform an unbiased random walk featuring persistent swimming for about a second interposed by short tumbles after which bacteria pick a random direction to swim. While swimming, a bacterium creates Stokesian hydrodynamic disturbances which behave like a force-dipole in the far-field owing to the absence of any net force or net torque on the bacterium (Berg, 2003; Lauga & Powers, 2009). Numerical studies on hydrodynamically interacting self-propelled particles (Hernandez-Ortiz *et al.*, 2005; Saintillan & Shelley, 2007; Underhill *et al.*, 2008) and continuum theories of active particle suspensions (Simha & Ramaswamy, 2002; Saintillan & Shelley, 2008*a*,*b*; Subramanian & Koch, 2009; Hohenegger & Shelley, 2010) suggest that the bulk flow observed in experiments (Mendelson *et al.*, 1999; Wu & Libchaber, 2000; Dombrowski *et al.*, 2004; Sokolov *et al.*, 2007, 2009; Ishikawa *et al.*, 2011; Dunkel *et al.*, 2013) arises from the hydrodynamic disturbances associated with bacterial swimming. At the continuum level, the effect of swimming induced force-dipoles on bacteria is to provide an "active" stress field as a function of the local orientation and concentration fields of bacteria and continuum theories of suspensions of swimming bacteria (Subramanian & Koch, 2009) and other self-propelled particles (Simha & Ramaswamy, 2002; Saintillan & Shelley, 2008*a*,*b*; Hohenegger & Shelley, 2010) have shown the existence of hydrodynamic instabilities driven by the active stress of swimmers. These stability analyses assume an unbounded suspension with a homogeneous base state and the instability originates from the coupling between the bacterial orientation field and the fluid flow through the shear-induced rotation of bacteria. The instability would set in only if the

bacterial concentration exceeds a critical value owing to the stabilizing effect of bacterial tumbling or rotational diffusion (see (Subramanian & Koch, 2009)).

While the assumption of an unbounded and homogeneous base state has greatly simplified the stability analysis in the above-mentioned investigations, such a state with large enough bacterial concentration for the instability is unlikely to persist at macroscopic length scales in bacterial suspensions encountered in practical situations. For example, when suspensions of aerobic bacteria such as *B. Subtilis* are exposed to air, bacteria concentrate near the air-water interface due to their preferential migration along the direction of increasing oxygen concentration (aerotaxis) and the no-flux boundary condition at the interface (Dombrowski *et al.*, 2004; Sokolov *et al.*, 2009). The stability of such inhomogeneous bacterial suspensions is of practical interest and in a recent work Kasyap & Koch (2012) we have shown theoretically that an inhomogeneous bacteria concentration field in the base state resulting from bacterial chemotaxis along the direction of an imposed chemo-attractant gradient can give rise to a novel instability which relies on the convection of bacteria by the fluid flow instead of their rotation as in the case of previously analyzed instabilities in homogeneous bacterial suspensions (Simha & Ramaswamy, 2002; Saintillan & Shelley, 2008*a*,*b*; Subramanian & Koch, 2009; Hohenegger & Shelley, 2010). In those investigations, the homogeneity of the base state precluded the fluid convection of bacteria in the linearized stability equations and as a result bacteria concentration fluctuations did not arise in the linear order at macroscopic length scales.

In the situation considered in our previous work (Kasyap & Koch, 2012) the inhomogeneity of the suspension was due to the active migration of bacteria

along the imposed chemical gradient. However, passive mechanisms such as fluid convection of bacteria can also result in inhomogeneous bacteria concentration possibly with regions of large bacteria concentration susceptible to instabilities and a thorough understanding of the dynamics bacterial suspensions warrants studies of such cases. An evaporating sessile drop of a bacterial suspension is an excellent model system to study the effect of passive bacterial accumulation owing to its simplicity. Furthermore, the sessile drop geometry can also be important in the context of bacterial swarming and biofilm formation which often involve bacteria confined within thin liquid films (Bees *et al.*, 2000; Joanny & Ramaswamy, 2012). While there have been a few experimental investigations in past on evaporating drops of bacterial suspensions such as of Nellimoottil *et al.* (2007), Baughman *et al.* (2010), and Sempels *et al.* (2013), none of them have considered the collective dynamics of the bacterial suspension near the contact-line of the drop. For example, Nellimoottil *et al.* (2007) and Baughman *et al.* (2010) studied the patterns of deposited bacteria near the contact-line after drying the drop completely and Sempels *et al.* (2013) did experiments that showed the existence of Marangoni flows in drying drops driven by the surfactants that bacteria secrete. We on the other hand observe the region near the contact-line of the drop during evaporation and we use wild-type *E. Coli* strain RP437 in our study which does not secrete any surfactant (see (Be'er & Harshey, 2011)). The present experiment can be important in the context of biofilms since the RP437 strain of *E. Coli* is known to produce biofilms (Hou *et al.*, 2007).

5.3 Materials and Methods

Cells of wild-type *E. Coli* strain RP437 containing green fluorescent protein (GFP) plasmid were grown overnight in tryptone broth (10 g bacto-tryptone powder and 5 g sodium chloride per liter of 10 mM phosphate buffer) at $30°C$ and 200 revolutions per minute in a rotary water bath followed by dilution by a factor of 25 into fresh tryptone broth. The diluted culture was then allowed to grow in the rotary shaker until bacteria reached the mid-exponential phase of its growth (suspension optical density at 600 nm, $OD_{600} \approx 0.5$) at which point bacteria were harvested by centrifugation at 2000g for 3 minutes and then washed and resuspended gently into a motility medium consisting of 10mM lactic acid, 0.1 mM EDTA, and 1 μM L-methionine. Prior to harvesting, the fluorescence of bacteria was activated by adding the promoter isopropyl thiogalactopyranoside (IPTG) to the suspension to a concentration of 500 μM when the optical density of the suspension reached around 0.2. A 1μL drop of the final bacteria suspension was placed on a glass coverslip coated with 0.2% bovine serum albumin solution to reduce adhesion of bacteria onto the glass coverslip (see Cheng *et al.* (2007)). The approximate radius of the drop was 1 mm and the approximate contact angle in the beginning was 40 degrees. The bacterial concentration in the final suspension was varied between $1.2 * 10^9$ bacteria per milliliter to 10^{10} bacteria per milliliter.

To visualize the collective motion of bacteria, we image the region near the contact-line of of the drop using an epi-fluorescence microscope – Olympus IX-51, with 10x objective lens and EXFO X-Cite 120 fluorescent illumination system. Control experiments were done with the evaporation of the drop being prevented by covering the drop by means of a petri-dish lid lined with a moist

paper wipe. Additional control experiments were also done on evaporating drops of suspensions of smooth-swimming strain RP9535 of *E. Coli* and the tumbling strain RP1616 (Wu *et al.*, 2006) to understand the role of bacterial motility on the observed collective motion. In addition, we measure the typical contact angle of the drop by means of a contact angle goniometer (Ramé-hart instrument co., NJ) and the typical evaporation-induced fluid velocity by tracking micron-scale tracer particles. The contact angle measurement were performed on bacteria suspension drops of concentration 10^{10} bacteria per milliliter and the fluid velocity measurements were done on drops of motility medium without any bacteria but seeded with 1.01 μm diameter fluorescent polystyrene beads (Bangs Laboratories, IN) at a concentration of around 10^8 beads per milliliter. These particles were tracked in movies of evaporating drop taken at a magnification of 20x and a speed of 30 frames per second.

5.4 Results

We first give a summary of the observations that we made from the experiments described above and then proceed to the detailed discussion of these results. We first visualize the dynamics near the contact-line of the evaporating drop through time-lapsed images given in Fig. 5.1 and also through the time evolution of the fluorescence intensity profile given in Fig. 5.2. To see whether the collective motion originates from the possible chemotaxis of bacteria towards oxygen, we observe the near contact-line dynamics of evaporating drops of suspensions containing the smooth-swimming cells of *E. Coli* (strain RP9535) which are non-chemotactic in Fig. 5.3(a). In Figs. 5.3(b) and (c) we study the effect of evaporation of the drop and the bacterial motility respectively by preventing the

drop evaporation in the first and by using a suspension of incessantly tumbling cells of *E. Coli* (strain RP1616) in the second. Next, we investigate the effect of the bacterial concentration on the collective motion by varying the concentration in the range of $1.2 * 10^9$ bacteria per milliliter to 10^{10} bacteria per milliliter and the resulting observations are shown in Fig. 5.4. Finally, the variation of the contact angle with time and the magnitude of the fluid velocity inside drop are investigated and the results are shown in Fig. 5.5.

We now proceed to the details of the experimental observations. Figure 5.1 shows time-lapsed images of the near-contact-line region of an evaporating drop containing wild-type *E. Coli* cells starting from one and a half minutes from the placement of the drop and until the drop has dried out completely (≈ 10 minutes). The bacterial concentration in the suspension is about 10^{10} bacteria per milliliter and since this is large, individual cells cannot be seen in the figure and the fluorescence intensity qualitatively represent the number of bacteria per unit area of the the drop measured on the glass substrate supporting the drop. Figure 5.2 shows the variation of fluorescence intensity in the direction normal to the contact-line (approximately) corresponding to the images at 2 minutes, 4 minutes, and 6 minutes in Fig. 5.1. In the beginning when the drop has not evaporated significantly, the bacteria concentration in the drop would be more or less uniform since the suspension is well-mixed. However, since the thickness of the drop increases as we move toward the center of the drop, the number of bacteria per unit area also increases thus resulting in a monotonically increasing fluorescent intensity toward the center of the drop at early times as seen in Fig. 5.1 and in Fig. 5.2 (see the intensity profile labeled as "2 min"). As time passes, bacteria accumulate near the contact-line owing to the evaporation-driven radial flow in the drop and the no-flux boundary condition

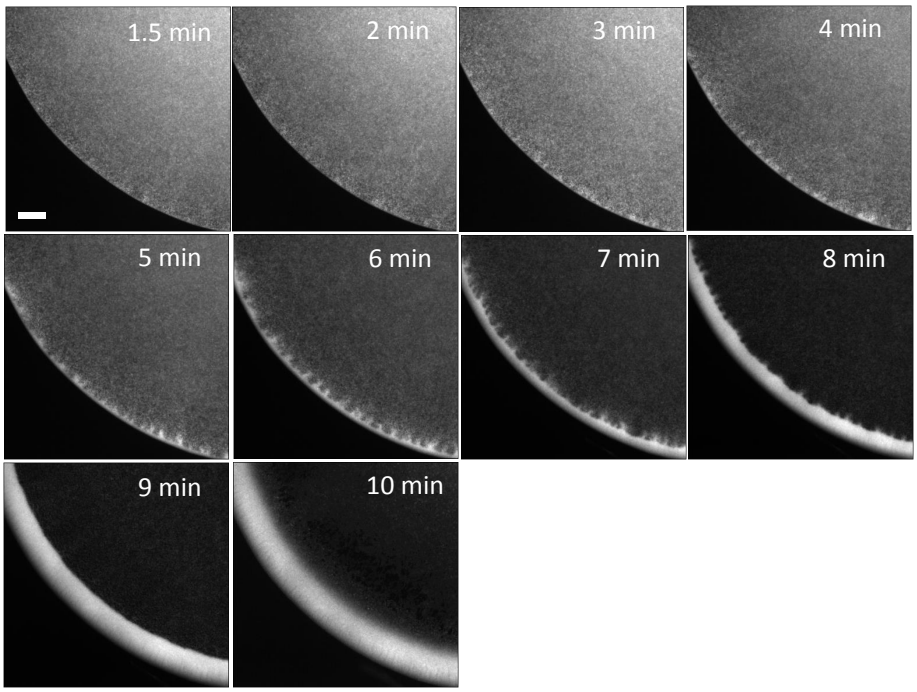

Figure 5.1: Time-lapsed images of the contact-line region of evaporating drop of wild-type (RP437) *E. Coli* suspension. The times shown on the images are the times that elapsed from the placement of the drop. The collective motion of bacteria appearing in the from of a periodic variation in bacterial concentration near the contact-line is apparent in images at 5, 6, and 7 minutes. The scale bar in the first image represents a distance of $100\mu m$.

at the contact-line and as a result the fluorescence intensity near the contact-line increases. This is evident in the image at 4 minutes given in Fig. 5.1 and also in the non-monotonic nature of the intensity profile at 4 minutes given in Fig. 5.2. At intermediate times of around 5 to 7 minutes from the placement of the drop, the accumulated bacteria near the contact line organize themselves into periodic clusters along the periphery the drop as seen in Fig. 5.1 and the bacterial density is strongly peaked near the contact-line as seen in the intensity profile at 6

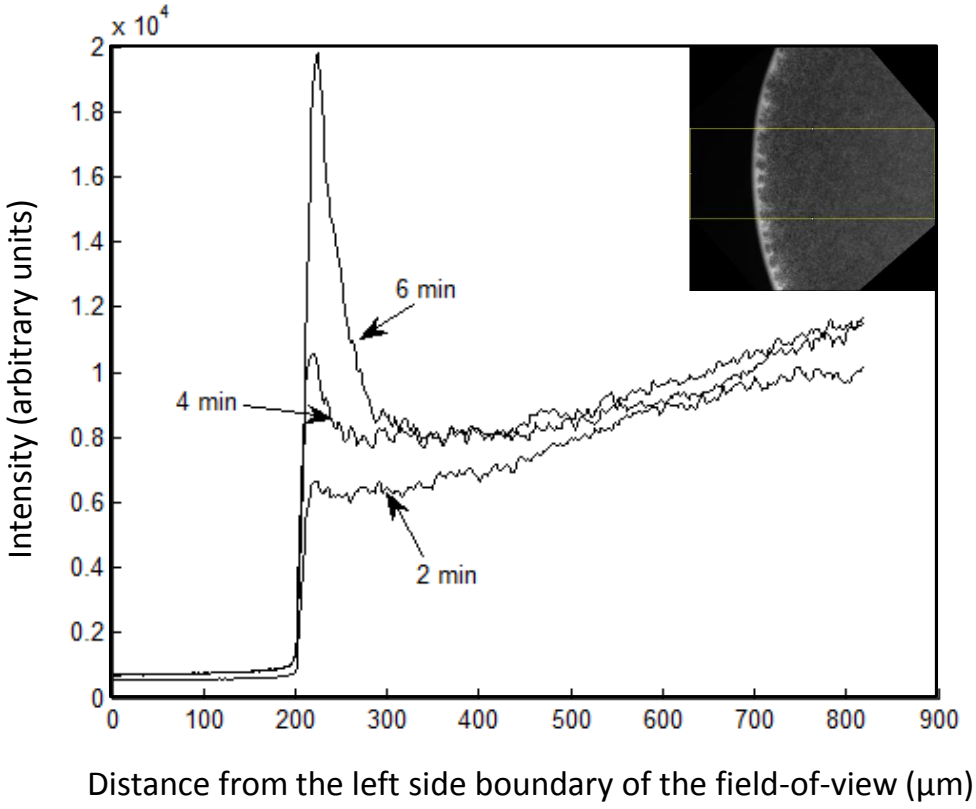

Figure 5.2: Fluorescence intensity variation in the approximate normal direction of the contact-line for images at 2, 4, and 6 minutes in Fig. 5.1. The intensity profiles were obtained by first rotating the aforementioned frames to the form shown in the inset and vertically averaging the intensity in the area shown in the inset with yellow lines. The inset is the rotated version of the image at 6 minutes in Fig. 5.1.

minutes in Fig. 5.2. The typical wavelength of the pattern was found to be of the order of 50 μm which is comparable to the length scale over which the bacteria concentration varies in the radial direction near the contact-line and much larger than the length of an individual bacterium (of the order of $10\mu m$). We took movies of the collective motion and a close examination of them revealed that the periodic clusters of bacteria in images at times 5 - 7 minutes in Fig. 5.1 are in

fact dense bacterial jets directed away from the contact-line and the pattern was more or less stationary. Nevertheless, the pattern eventually disappeared as the drop evaporated further as seen in images from the 8 minutes onwards in Fig. 5.1.

While the pattern observed in Fig. 5.1 is similar to the one observed by Dombrowski *et al.* (2004) it is the gravitational instability of the suspension arising from the chemotactic accumulation of bacteria near the surface of the drop that caused pattern in that case. In fact, Dombrowski *et al.* (2004) had prevented evaporation-driven flows inside the drop by enclosing the drop inside a chamber with high humidity. Thus the chemotaxis of bacteria towards oxygen (or in general aerotaxis) is a fundamental requirement for pattern formation in the experiment of Dombrowski *et al.* (2004). In contrast to this, our experiments with smooth-swimming strain of *E. Coli* (RP9535) which is non-chemotactic also show (see Fig. 5.3(a)) similar pattern as in Fig. 5.1 thus ruling out aerotaxis driven bioconvection as the mechanism behind the pattern seen in Fig. 5.1. This is further confirmed by the observation that the pattern shown in Fig. 5.1 can be eliminated completely by preventing the evaporation of drop as seen in Fig. 5.3(b) while the patterns resulting from bioconvection in the experiment of Dombrowski *et al.* (2004) were observed in the absence of any evaporation driven flow within the drop. Furthermore, while the diameter and the initial thickness of drops used in the present experiment is about 2 mm and 500 μm respectively, Dombrowski *et al.* (2004) observe bioconvection-driven patterns in a much larger drop with a diameter of around 1 cm and thickness 2 mm which is not surprising since the gravitational instability leading to bioconvection occurs in general at larger length scales (see Koch & Subramanian (2011)). Figure 5.3(c) shows the image of the contact-line region of a drop of a suspension of

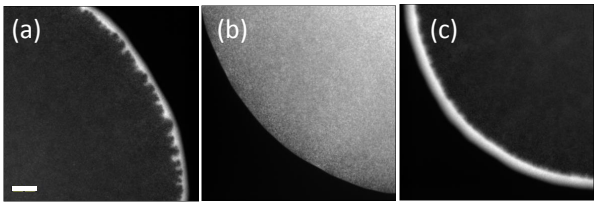

Figure 5.3: Image of the contact-line region of (a) evaporating sessile drop of suspension of smooth-swimming *E. Coli* (RP9535), (b) non evaporating drop of wild-type *E. Coli* (RP437) suspension, and (c) evaporating drop of incessantly tumbling *E. Coli* (RP1616) suspension. The scale bar in figure (a) represents a distance of $100\mu m$ and the bacteria concentration for all cases are approximately the same as in Fig. 5.1 ($\approx 10^{10}$ bacteria per milliliter). For figure (b) the evaporation of the drop was prevented by covering the drop with the lid of a small petri-dish lined with moist paper. All the images are taken at the same time (≈ 6.5 minutes) from the placement of the drop and the drying times of drops shown in figure (a) and (c) are around 9.5 minutes.

incessantly tumbling cells of *E. Coli* (RP1616). The bacteria concentration and the time at which the image is captured in this experiment are approximately the same as in Fig. 5.1. While the pattern in this case is much more diffuse when compared to Fig. 5.1 at 6 minutes, periodic jet-like structures can be identified in the top left corner region of the image. The difference between patterns in Fig. 5.3(c) and Fig. 5.1 at 6 minutes suggest a link between the pattern formation and the motility of bacteria whose precise nature is yet to be determined. We also did experiments with different bacteria concentrations and we found that the width of the region of the collective motion decreases with the decrease in bacteria concentration as seen in Fig. 5.4.

To further characterize the observed patterns we investigate the variation of the contact angle of the bacterial suspension drop with respect to time as the

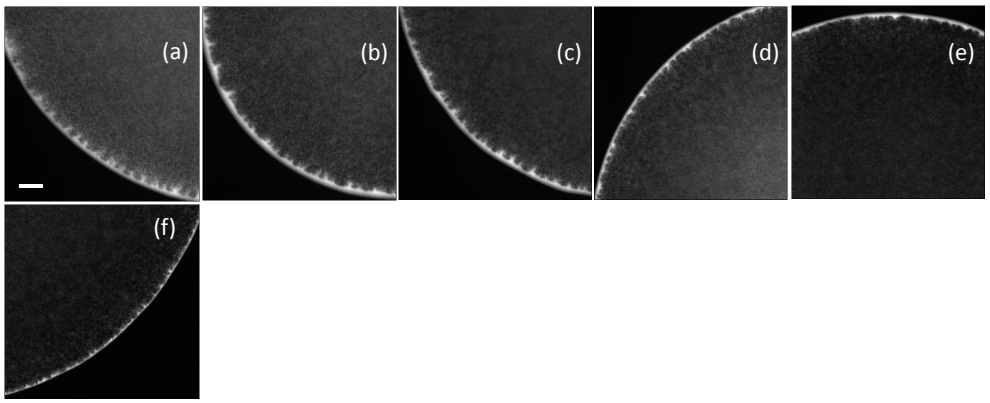

Figure 5.4: Image of the contact-line region of evaporating sessile drop of suspension of of wild-type *E. Coli* cells at varying bacterial concentrations concentrations. (a) 10^{10} bacteria per milliliter (b) $7.5{*}10^9$ bacteria per milliliter, (c) $6{*}10^9$ bacteria per milliliter, (d) $4.5*10^9$ bacteria per milliliter, (e) $2.4*10^9$ bacteria per milliliter, and (f) $1.3*10^9$ bacteria per milliliter. The scale bar in figure (a) represents a distance of $100\mu m$ and the drop radii are approximately the same (≈ 1 mm) for all cases.

drop evaporates and we also measure the typical evaporation-induced fluid velocity inside the drop by tracking fluorescent tracer particles suspended in a drop of motility medium without any bacteria. The drop volume used in both experiments is the same as in Figs. 5.1, 5.3, and 5.4 ($1\mu L$) and the glass coverslips for these experiments were also prepared in the identical manner. The time variation of the contact angle is shown in Fig. 5.5(a) and the variation of the evaporation-induced radial velocity with distance from the contact-line is shown in Fig. 5.5(b). It is clear from Fig. 5.5(a) that the contact angle of the drop decreases more or less linearly with time which is consistent with the results from numerical simulations of drop evaporation by Hu & Larson (2002). In Fig. 5.1 the collective motion is predominantly observed at durations between $0.5t_d$ to $0.7t_d$ where t_d is the drying time of the drop and Fig. 5.5(a) shows that the typical contact angle during these times is around 20 degrees. The experimen-

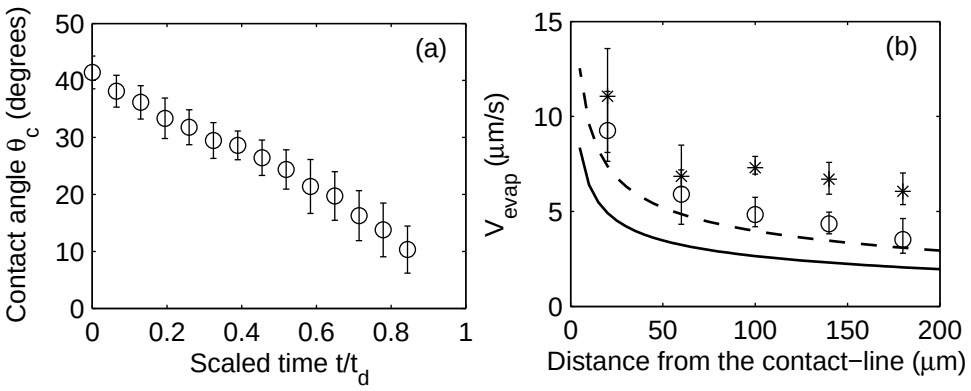

Figure 5.5: (a) Variation of the contact angle (θ_c) with time for an evaporating sessile drop of bacterial suspension at a bacterial concentration of 10^{10} bacteria per milliliter. Time is scaled by the drying time (≈ 8 minutes) of the drop and the error bars show one standard deviation to either sides of the mean value obtained from ten measurements for each data point. (b) Typical evaporation-induced fluid velocity inside an evaporating sessile drop versus distance from the contact line measured at times $t/t_d = 0.5$ (square), and $t/t_d = 0.67$ (asterisk) from the placement of the drop. The drop did not contain any bacteria and was seeded with $1\mu m$ size fluorescent tracer particles at a low concentration of about 10^8 per milliliter. The velocity data was obtained by manual tracking of five tracer particles lying in a strip of width $40\mu m$ centered at each data points and the error bars in the figure show the maximum and minimum velocities obtained those five. The lines at the bottom of the plot shows the analytical predictions of the depth-averaged fluid velocity inside the drop obtained from lubrication theory given in Eq. 5.1 (see Deegan *et al.* (1997) and Hu & Larson (2005)) for a typical contact angle of $\theta_c = 20$ degrees, drop radius $R = 1mm$, and drying time $t_d = 10$ minutes. The solid line is for $t/t_d = 0.5$ and the dashed line is for $t/t_d = 0.67$ with $t_d \approx 6$ minutes.

tally measured evaporation-induced fluid velocity inside the drop during these times is of the order of $10\mu m/s$ near the contact-line as shown in Fig. 5.5(b) by symbols. The velocity data in Fig. 5.5 were obtained by manually tracking the tracer particles appearing in the movies of the near-contact-line region of the drop and since the tracking procedure is labor intensive, only five particles were tracked for each data point. For each data point, only those particles which were fast-moving and passing through a strip of width $20\mu m$ in the radial direction to either sides of the location of the data point were chosen to be tracked. Thus the velocity data given Fig. 5.5 can only be considered to be representing the typical order of magnitude of the fluid velocity inside the drop. The lines in Fig. 5.5(b) show the prediction of the depth-averaged fluid velocity from the lubrication theory of evaporating drops (Deegan *et al.*, 1997; Hu & Larson, 2005)

$$V_{evap} = \frac{R}{t_d}\frac{1}{4(1-t/t_d)}\frac{\left[(1-\tilde{r}^2)^{-\lambda(\theta_c)} - \left(1-\tilde{r^2}\right)\right]}{\tilde{r}} \tag{5.1}$$

where R is the radius of the drop ($\approx 1mm$), t_d is the drying time (≈ 6 minutes), $\tilde{r} = (R-y)/R$ is the non-dimensional radial co-ordinate measured from the center of the drop with y being the distance from the contact-line, and $\lambda(\theta_c) = \pi/2 - \theta_c/180$ where $\theta_c \approx 20$ is the contact angle of the drop in degrees. The fluid velocity increases as we move toward the contact-line and at the contact-line ($y = 0$) the fluid velocity is divergent due to the singularity in the diffusive flux of the vapor (see Deegan *et al.* (1997) and Hu & Larson (2005)) and the vanishing depth of the drop. The qualitative nature of the radial velocity variation in the drop is reproduced in our experiments as seen in Fig. 5.5 and the order of magnitude of the fluid velocity also agrees with the theoretical prediction in Eq. 5.1.

One important observation is that the length scale over which the bacteria

concentration varies in Fig. 5.2 at 6 minutes is of the order of 100 μm while the balance of the convective flux of bacteria due to evaporation-driven flow and the bacterial diffusive flux would give a length scale of $D/V_{evap} = 10\mu m$ (with the typical magnitude of $V_{evap} = 10\mu m/s$ and the bacteria diffusivity $D = 100\mu m^2/s$) which is in order of magnitude smaller than the observation. The most likely reason for this discrepancy is that the collective motion drives bacteria away from the contact-line since the bacterial "jets" associated with the collective motion seen in Fig. 5.1 are directed away from the contact-line. This reasoning is reinforced by the observation in Fig. 5.1 at 6 minutes that bacteria accumulate in significantly thinner layers in regions that lie between two bacterial jets.

5.5 Concluding discussion

The experimental observations described in the previous section establish the existence of a collection motion of bacteria near the contact-line of an evaporating sessile drop appearing as a periodic variation in the bacteria concentration along the periphery of the drop. The evaporation-driven radial flow inside the drop along with the impenetrability condition at the contact-line concentrate bacteria near the contact-line where the bacterial population organize themselves into periodic jets directed toward the center of the drop. Experiments show that the bacterial collective motion does not appear when the evaporation of the drop is prevented by enclosing it inside a humid chamber. The observation of collective motion in both wild-type cells and smooth-swimming cells rules out chemotaxis as the reason behind the collective motion. The motility of bacteria nevertheless seems to influence the organized motion since the periodic variation in bacteria concentration observed for cells which tumble incessantly

is much more diffuse that that for the wild-type suspension at similar bacteria concentrations. We further observe that decreasing the bacteria concentration results in a decrease in the spatial extent of collective motion. Finally, experiments with fluorescent tracer particles show that the evaporation-driven radial fluid velocity in the region where collective motion is observed is comparable to the swimming speed of bacteria.

Since the collective motion observed here is characterized by the periodic variation of the bacterial density near the contact-line, it is reasonable to suspect that the observed pattern in the present experiment arises from the concentration instability of an inhomogeneous base state characterized by the balance between evaporation-induced convection and diffusion of bacteria. The following heuristic analysis of the present problem in the point of view of the linear stability of continuum bacteria and momentum conservation equations (see Subramanian & Koch (2009)) of the bacteria suspension suggests the possibility of an instability driven by the coupling between the bacteria concentration field and the bacteria stress driven fluid flow. First, the inhomogeneous base state resulting from the balance between the diffusion of bacteria and convection by evaporation-driven fluid flow gives rise to a source for bacteria concentration fluctuations appearing as the term $\boldsymbol{u}' \cdot \nabla n_0$ where $\boldsymbol{u}'$ is the perturbed fluid velocity field and n_0 is the base-state bacteria concentration field (see Kasyap & Koch (2012)) in the linearized bacteria conservation equation. Secondly, the bacteria concentration fluctuations can drive the fluid velocity perturbations, $\boldsymbol{u}'$ in the present problem owing to the shear-induced anisotropy in the bacterial orientation field in the base state. The shear associated with the evaporation driven fluid flow rotates bacteria causing their orientation field to be in general be anisotropic (Subramanian & Koch, 2009) and this would result the bacteria

stress term in the linearized momentum equation $\nabla \cdot [-C\mu U_s L^2 n' \langle \boldsymbol{pp} - \boldsymbol{I}/3 \rangle_0]$ where n' is the perturbed bacteria concentration field and $\langle \boldsymbol{pp} - \boldsymbol{I}/3 \rangle_0$ is the second moment tensor of the base-state orientation field to force the fluid velocity perturbations. Here $C \approx 0.57$ is the non-dimensional bacterial dipole strength, μ is the solvent viscosity, U_s is the bacterial swimming speed, and L is the overall length of the bacterium including its flagella bundle. An isotropic base state on the other hand, would not have such a term since $\langle \boldsymbol{pp} - \boldsymbol{I}/3 \rangle_0 = 0$ in that case.

The degree of anisotropy in the orientation field of the bacteria in the present problem is determined by the competition between the rotation of the bacteria by the shear associated with the fluid flow and bacterial tumbling. For small shear rates compared to the bacterial tumbling frequency, bacteria would tend to orient near the extensional axis of the fluid flow and for large shear rates, they would tend to orient along the flow direction. It is thus useful to look at the non-dimensional shear rate associated with the evaporation-induced fluid flow inside the drop defined as $\Gamma = V_{evap}/(h\tau^{-1})$ with h being the thickness of the drop and τ^{-1} being the bacterial tumbling frequency. In Fig. 5.6 we show the variation of Γ with respect to the distance from the contact-line. The calculated values of Γ shown in Fig. 5.6 is based on the typical values of experimentally obtained V_{evap} given in Fig. 5.5(b) and with the typical tumbling frequency of bacteria of $\tau^{-1} = 1/s$. The thickness of the drop h as a function of distance from the contact-line is calculated for the typical contact-line radius $R = 1mm$ and the contact angle of $\theta_c = 20$ degrees. Since the contact angle is small, the thickness profile of the drop can be approximated to be a parabola so that $h(y) = h_0(1-\tilde{r}^2)$ (Hu & Larson, 2005) where $h_0 = R(1/\sin(\theta_c) - 1/\tan(\theta_c))$ is the maximum height of the drop and $\tilde{r}(y)$ is the non-dimensional radial coordinate defined earlier. The non-dimensional shear rate shown in Fig. 5.6 is of order 1 near the contact-

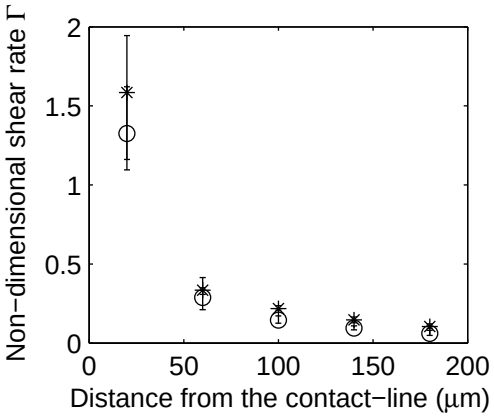

Figure 5.6: (a) Variation of the non-dimensional shear rate associated with the experimentally obtained fluid velocity inside drop given in Fig. 5.5(b) with respect to the distance from the contact-line. Circles correspond to the velocity data at 3 minutes in Fig. 5.5(b) and stars correspond to the data at 4 minutes.

line and it decays quickly as we move farther into the bulk of the drop. Thus the evaporation-induced flow would tend to orient bacteria lying far away from the contact-line near the extensional axis of the shear flow and their orientation would be progressively brought toward the flow direction as we approach the contact-line. Thus the base state bacterial orientation field will be significantly anisotropic in the region of collective motion facilitating bacteria concentration fluctuation driven fluid flows.

Thus in the present problem there exists a two-way coupling between the bacteria concentration field and the fluid flow such that bacteria concentration fluctuations can drive a fluid flow which in turn can transport bacteria. At present, it is not clear if such a coupling would indeed result in an instability and only a full linear stability analysis of the problem can confirm the possibility of the instability. This however is beyond the scope of the present investi-

gation. The present problem may appear to be somewhat similar to the case of chemotaxis driven instability described by us previously (Kasyap & Koch, 2012) in which the chemotaxis and diffusion of bacteria balance to yield an inhomogeneous base state which is unstable to bacterial concentration fluctuations if the mean bacterial concentration exceeds a critical value. However, the disturbance fluid flow in that case is driven by the perturbations in the normal stresses that bacteria create owing to the net orientation of bacteria along the direction of the chemical gradient. In contrast to that, the thin film geometry of the present problem causes the fluid disturbances to be driven predominantly by the perturbations in bacterial shear stress.

Bibliography

BAUGHMAN, KYLE F., MAIER, RAINA M., NORRIS, THERESA A., BEAM, BROOKE M., MUDALIGE, ANOMA, PEMBERTON, JEANNE E. & CURRY, JOAN E. 2010 Evaporative deposition patterns of bacteria from a sessile drop: Effect of changes in surface wettability due to exposure to a laboratory atmosphere. *Langmuir* **26** (10), 7293–7298.

BE'ER, AVRAHAM & HARSHEY, RASIKA M. 2011 Collective motion of surfactant-producing bacteria imparts superdiffusivity to their upper surface. *Biophysical Journal* **101** (5), 1017 – 1024.

BEES, M. A., ANDRESN, P., MOSEKILDE, E. & GIVSKOV, M. 2000 The interaction of thin-film flow, bacterial swarming and cell differentiation in colonies of serratia liquefaciens. *Journal of Mathematical Biology* **40** (1), 27–63.

BERG, H. C. 2003 *E. coli in Motion*. Springer Verlag.

CHENG, S. Y., HEILMAN, S., WASSERMAN, M., ARCHER, S., SHULER, M. L. & WU, M. 2007 A hydrogel-based microfluidic device for the studies of directed cell migration. *Lab Chip* **7**, 763–769.

DEEGAN, ROBERT D, BAKAJIN, OLGICA, DUPONT, TODD F, HUBER, GREB, NAGEL, SIDNEY R & WITTEN, THOMAS A 1997 Capillary flow as the cause of ring stains from dried liquid drops. *Nature* **389** (6653), 827–829.

DEEGAN, ROBERT D., BAKAJIN, OLGICA, DUPONT, TODD F., HUBER, GREG, NAGEL, SIDNEY R. & WITTEN, THOMAS A. 2000 Contact line deposits in an evaporating drop. *Phys. Rev. E* **62**, 756–765.

DOMBROWSKI, C., CISNEROS, L., CHATKAEW, S., GOLDSTEIN, R. E. & KESSLER, J. O. 2004 Self-concentration and large-scale coherence in bacterial dynamics. *Phys. Rev. Lett.* **93**, 098103.

DUNKEL, JÖRN, HEIDENREICH, SEBASTIAN, DRESCHER, KNUT, WENSINK, HENRICUS H., BÄR, MARKUS & GOLDSTEIN, RAYMOND E. 2013 Fluid dynamics of bacterial turbulence. *Phys. Rev. Lett.* **110**, 228102.

HERNANDEZ-ORTIZ, J. P., STOLTZ, C. G. & GRAHAM, M. D. 2005 Transport and collective dynamics in suspensions of confined swimming particles. *Phys. Rev. Lett.* **95**, 204501.

HOHENEGGER, C. & SHELLEY, M. J. 2010 Stability of active suspensions. *Phys. Rev. E* **81**, 046311.

HOU, SHUYU, BURTON, ERIK A., SIMON, KAREN A., BLODGETT, DUSTIN, LUK, YAN-YEUNG & REN, DACHENG 2007 Inhibition of escherichia coli biofilm formation by self-assembled monolayers of functional alkanethiols on gold. *Applied and Environmental Microbiology* **73** (13), 4300–4307.

HU, HUA & LARSON, RONALD G. 2002 Evaporation of a sessile droplet on a substrate. *The Journal of Physical Chemistry B* **106** (6), 1334–1344.

HU, HUA & LARSON, RONALD G. 2005 Analysis of the microfluid flow in an evaporating sessile droplet. *Langmuir* **21** (9), 3963–3971.

ISHIKAWA, T., YOSHIDA, N., UENO, H., WIEDEMAN, M., IMAI, Y. & YAMAGUCHI, T. 2011 Energy transport in a concentrated suspension of bacteria. *Phys. Rev. Lett.* **107**, 028102.

JOANNY, JEAN-FRANÇOIS & RAMASWAMY, SRIRAM 2012 A drop of active matter. *Journal of Fluid Mechanics* **705**, 46–57.

KASYAP, T. V. & KOCH, DONALD L. 2012 Chemotaxis driven instability of a confined bacterial suspension. *Phys. Rev. Lett.* **108**, 038101.

KIM, M. J. & BREUER, K. S. 2004 Enhanced diffusion due to motile bacteria. *Phys. Fluids* **16**, L78–L81.

KOCH, D. L. & SUBRAMANIAN, G. 2011 Collective hydrodynamics of swimming microorganisms: Living fluids. *Ann. Rev. Fluid Mech.* **43**, 637–659.

LAUGA, E. & POWERS, T. R. 2009 The hydrodynamics of swimming microorganisms. *Rep. Prog. Phys.* **72**, 096601.

MENDELSON, N. H., BOURQUE, A., WILKENING, K., ANDERSON, K. R. & WATKINS, J. C. 1999 Organized Cell Swimming Motions in Bacillus subtilis Colonies: Patterns of Short-Lived Whirls and Jets. *J. Bacteriol.* **181**, 600–609.

NELLIMOOTTIL, TITTU THOMAS, RAO, PINJALA NAGARAJU, GHOSH, SIDDHARTHA SANKAR & CHATTOPADHYAY, ARUN 2007 Evaporation-induced

patterns from droplets containing motile and nonmotile bacteria. *Langmuir* **23** (17), 8655–8658.

SAINTILLAN, D. & SHELLEY, M. J. 2007 Orientational order and instabilities in suspensions of self-locomoting rods. *Phys. Rev. Lett.* **99**, 058102.

SAINTILLAN, D. & SHELLEY, M. J. 2008*a* Instabilities and pattern formation in active particle suspensions: Kinetic theory and continuum simulations. *Phys. Rev. Lett.* **100**, 178103.

SAINTILLAN, D. & SHELLEY, M. J. 2008*b* Instabilities, pattern formation, and mixing in active suspensions. *Phys. Fluids* **20**, 123304.

SEMPELS, WOUTER, DE DIER, RAF, MIZUNO, HIDEAKI, HOFKENS, JOHAN & VERMANT, JAN 2013 Auto-production of biosurfactants reverses the coffee ring effect in a bacterial system. *Nature communications* **4**, 1757.

SIMHA, R. A. & RAMASWAMY, S. 2002 Hydrodynamic fluctuations and instabilities in ordered suspensions of self-propelled particles. *Phys. Rev. Lett.* **89**, 058101.

SOKOLOV, ANDREY, ARANSON, IGOR S., KESSLER, JOHN O. & GOLDSTEIN, RAYMOND E. 2007 Concentration dependence of the collective dynamics of swimming bacteria. *Phys. Rev. Lett.* **98**, 158102.

SOKOLOV, A., GOLDSTEIN, R. E., FELDCHTEIN, F. I. & ARANSON, I. S. 2009 Enhanced mixing and spatial instability in concentrated bacterial suspensions. *Phys. Rev. E* **80**, 031903.

SUBRAMANIAN, G. & KOCH, D. L. 2009 Critical bacterial concentration for the onset of collective swimming. *J. Fluid Mech.* **632**, 359–400.

TUVAL, IDAN, CISNEROS, LUIS, DOMBROWSKI, CHRISTOPHER, WOLGEMUTH, CHARLES W., KESSLER, JOHN O. & GOLDSTEIN, RAYMOND E. 2005 Bacterial swimming and oxygen transport near contact lines. *Proceedings of the National Academy of Sciences of the United States of America* **102** (7), 2277–2282.

UNDERHILL, P. T., HERNANDEZ-ORTIZ, J. P. & GRAHAM, M. D. 2008 Diffusion and spatial correlations in suspensions of swimming particles. *Phys. Rev. Lett.* **100**, 248101.

WU, MINGMING, ROBERTS, JOHN W., KIM, SUE, KOCH, DONALD L. & DELISA, MATTHEW P. 2006 Collective Bacterial Dynamics Revealed Using a Three-Dimensional Population-Scale Defocused Particle Tracking Technique. *Appl. Environ. Microbiol.* **72** (7), 4987–4994.

WU, X. L. & LIBCHABER, A. 2000 Particle diffusion in a quasi-two-dimensional bacterial bath. *Phys. Rev. Lett.* **84**, 3017–3020.